INVESTIGATION OF THE THERMAL HISTORY OF THE DELAWARE BASIN USING CARBONATE CLUMPED ISOTOPE THERMOMETRY

A Thesis

by

HOWARD NATHAN NAYLOR

Submitted to the Office of Graduate and Professional Studies of
Texas A&M University
In partial fulfillment of the requirements for the degree of

MASTER OF SCIENCE

Chair of Committee,	Ethan L. Grossman
Committee Members,	Niall C. Slowey
	Nicholas D. Perez
Head of Department,	Michael C. Pope

AUGUST 2018

Major Subject: Geology

ABSTRACT

I utilized carbonate clumped isotope thermometry to explore the thermal history of the Delaware Basin, West Texas, USA. Carbonate wellbore cuttings from five oil/gas wells across the basin yielded apparent clumped isotope temperatures ($T(\Delta_{47})$) ranging from 26°C to 305°C, interpreted to reflect a combination of initial precipitation/recrystallization temperature and solid-state C-O bond reordering during burial. Dolomite samples record lower apparent $T(\Delta_{47})$s than calcite, interpreted to reflect greater resistance to reordering in dolomite. Using burial curves provided by the Chevron Center of Research Excellence (CoRE), I created unique time-temperature histories by linearly applying a geothermal gradient. Using two different Thermal History Reordering Models (THRMs), I modeled the extent of solid-state C-O bond reordering to iteratively find the time-averaged best-fit geothermal gradients (BFGGs) for each of the five wells. Results of this modeling suggest that the shallower, southwestern portion of the study area experienced roughly 40% higher geothermal gradients throughout the sediment history (40-45 °C/km) than did the deeper, southeastern portion (30-35 °C/km), with the northern portion experiencing intermediate geothermal gradients (35-40 °C/km). This trend agrees with the observed gas/oil ratios of the Delaware Basin, increasing from east to west. I furthermore compared my modeled maximum burial temperatures to previously published vitrinite reflectance data in two of the wells, and observe a good agreement in the maximum burial temperatures between the two methodologies.

DEDICATION

To my Mother –

ACKNOWLEDGEMENTS

I would like to thank my committee chair, Ethan Grossman, for his invaluable mentorship and for always pushing me to be my best. I thank committee members, Nicholas Perez and Niall Slowey for guiding and improving my research. I acknowledge and thank Will Defliese for his technical expertise, guidance and many contributions to the project. I acknowledge and thank Mauro Becker at the Chevron Center of Research Excellence for his contributions of burial history curves and research insights. I thank Chris Maupin for his personal and academic mentorship and his unwavering support throughout my graduate career. I thank Juan Carlos Laya for the use of his instrumentation and his guiding discussions. I also express sincere appreciation to Michael Heaney for his personal mentorship, and impromptu-midnight ambulance services. Finally, I thank my family, especially my parents Patti and Bud Naylor, and my fiancée Kelsey Haza, for their steadfast love and support.

I am very grateful for scholarships from the Berg-Hughes Center for Petroleum and Sedimentary Systems at Texas A&M University, the Texas A&M Foundation sponsored by ConocoPhillips, and the Michel T. Halbouty Chair in Geology.

CONTRIBUTORS AND FUNDING SOURCES

Contributors

This work was supervised by a thesis committee consisting of Professors Ethan L. Grosssman (advisor) and Nicholas D. Perez of the Department of Geology and Geophysics and Professor Niall C. Slowey of the Department of Oceanography.

All work for the thesis was completed by the student, in collaboration with Professor Ethan L. Grossman and Dr. William Defliese of the Department of Geology and Geophysics.

Funding Sources

Graduate study was supported by a fellowship from the Berg-Hughes Center for Petroleum and Sedimentary Systems at Texas A&M University, and scholarships from the Texas A&M Foundation, sponsored by ConocoPhillips, and the Michel T. Halbouty Chair in Geology.

TABLE OF CONTENTS

PAGE

PAGE

LIST OF FIGURES

PAGE

LIST OF TABLES

INTRODUCTION

The Permian Basin accounts for roughly 25% of the daily crude oil production within the continental United States (EIA.gov). The Delaware Basin, a sub-basin of the Permian Basin, is one of the most active exploration and production areas, even after close to 100 years of development. Despite the long production history, there remain puzzling aspects of the basin that have yet to be fully answered and explained. There exists an anomalous gas/oil ratio that increases to the west despite accompanying shallower burial depths (**Fig. 1**). Multiple possibilities to explain this occurrence include: asymmetric basin-scale burial and exhumation; long distance hydrocarbon migration; or possibly elevated burial temperatures associated with a higher geothermal gradient in western portions of the basin (Barker & Pawlewicz, 1987). To investigate the spatial and vertical patterns of basin thermal maturation, I utilize carbonate clumped isotope thermometry on samples collected from various locations and depths across the Delaware Basin.

The Delaware Basin has multiple stacked carbonate intervals spanning ages from the Cretaceous to Ordovician and burial depths ranging from outcrop to 22,000 ft, providing multiple levels to apply clumped isotope techniques to investigate burial history and paleo-geothermal gradients. Carbonate clumped isotopes can complement and refine standard industry methods of assessing thermal maturity, such as vitrinite reflectance. A clear understanding of a basin's thermal history has direct implications for quantifying source rock maturity, hydrocarbon generation, and economic prospectivity. Thus, clumped isotope thermometry has the potential to be a valuable addition to techniques used by the petroleum industry.

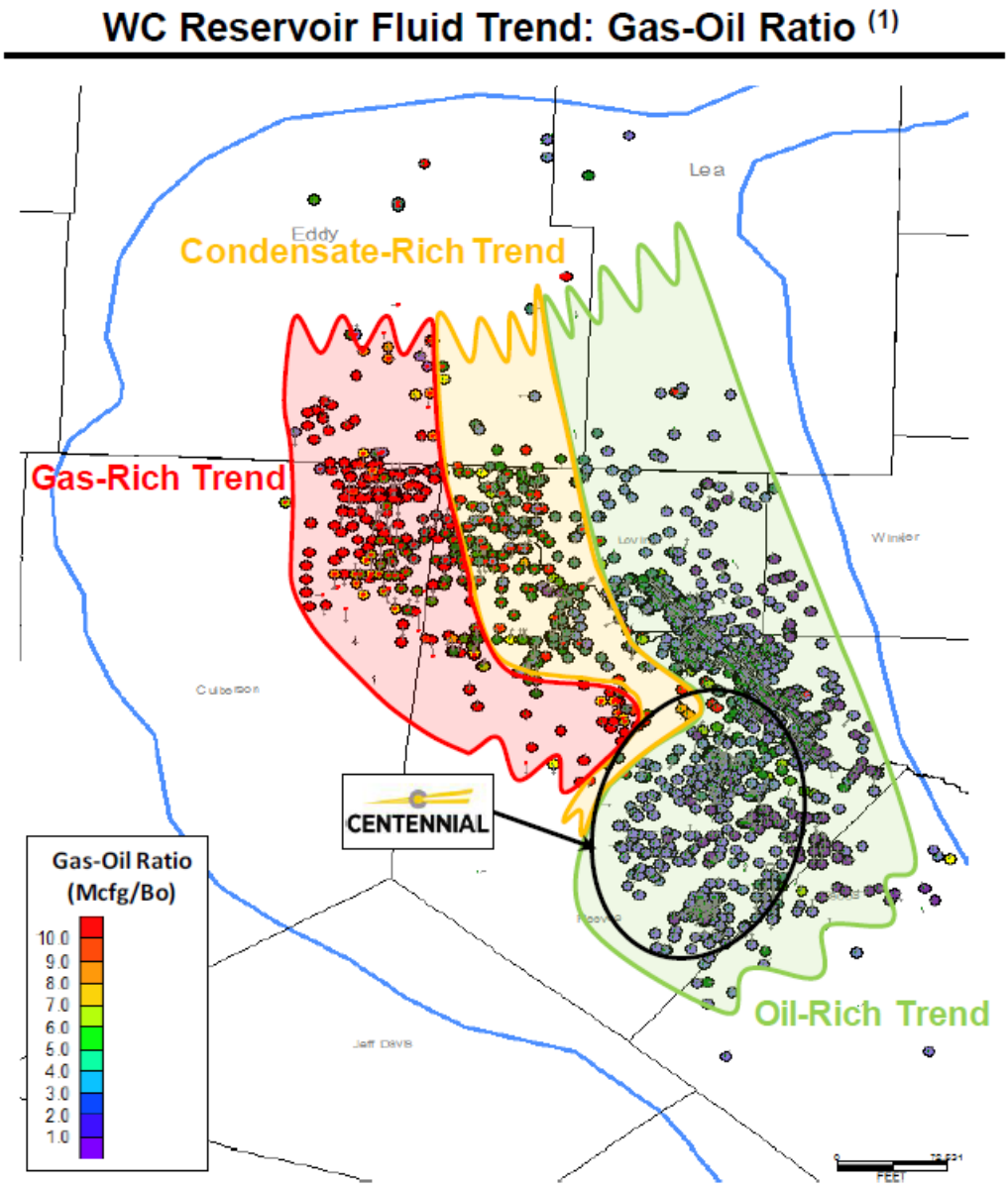

Figure 1- Gas/oil ratio of produced fluids from the Wolfcamp formation across the Delaware Basin. (Centennial Energy: Investor Presentation 2015).

Carbonate Clumped Isotopes

Carbonate clumped isotope thermometry is a burgeoning geochemical technique that measures the pairing of rare, heavy isotopes of carbon and oxygen in the same carbonate

molecule (Ghosh et al., 2006, Schauble et al., 2006). Following the principle put forth by Urey (1947), heavy isotopes form more stable bonds than light isotopes and are therefore energetically favorable within the crystal lattice, with this energy advantage more prevalent at lower temperatures. In clumped isotopes, researchers measure the occurrence of two heavy isotopes within the molecule or isotopologue (i.e., molecule that varies only in its isotopic composition) (Eiler, 2007; 2011). The solid-state exchange reaction for $CaCO_3$ is as follows, with the left side of the equation being favored at lower temperatures:

$$Ca^{12}C^{16}O_3 + Ca^{13}C^{18}O^{16}O_2 \leftrightarrow Ca^{12}C^{18}O^{16}O_2 + Ca^{13}C^{16}O_3 \quad (1)$$

This clumping of heavy isotopes does not involve exchange with water, therefore the clumped isotopic concentration of carbonate minerals is independent of the isotopic composition of formation waters. Furthermore, during the measurement of carbonate clumped isotopes, $\delta^{18}O$ and $\delta^{13}C$ are also measured. Therefore, using an oxygen isotope paleo-thermometry equation (e.g., Epstein et al., 1953; Kim & O'Niel, 1997), one can calculate the $\delta^{18}O$ of the ambient waters, which can inform paleoclimate reconstructions and the origin of diagenetic fluids.

The clumped isotopologue measured in this study (CO_2 produced from carbonate digestion by phosphoric acid) is $^{13}C^{18}O^{16}O$ (mass/charge [*m/z*] 47), which contains both the heavy isotopes ^{13}C and ^{18}O in the same molecule. The abundance of these clumped isotopologues in samples is higher than the expected stochastic ratio based on the natural abundances of the individual heavy isotopes (Eiler, 2007). In other words, molecules slightly favor having heavy isotopes substituted in its structure as they create a more stable molecule with a lower vibrational frequency (Urey, 1947). The degree of enrichment of the clumped isotopologue above the stochastic distribution, Δ_{47} (Eiler & Schauble, 2004), is temperature

dependent, and therefore isotopic analysis can be used as a paleothermometer (Ghosh et al., 2006). The equation for Δ_{47} is:

$$\Delta_{47} = \left[\left(\frac{R^{47}}{R^{47*}} - 1\right) - \left(\frac{R^{46}}{R^{46*}} - 1\right) - \left(\frac{R^{45}}{R^{45*}} - 1\right)\right] * 1000 \quad (2)$$

where R^{47} for example is the ratio of the ion beam intensities for *m/z* 47/44 in CO_2^+, and R^{47*} is the ratio that is expected based on the stochastic distribution of natural abundances of the isotopes. In the case of clumped isotopes, this expected stochastic distribution is the standard against which measurements are reported. At very high temperatures (>1000°C), Δ_{47} values fall to the expected stochastic distribution for the bulk composition of the sample, and Δ_{47} trends to 0 (Eiler & Schauble, 2004).

Carbonate clumped isotopes have been utilized in studies of paleoclimate and paleoceanography (e.g., Came et al., 2007; Finnegan et al., 2011), diagenesis and associated fluids (e.g. Huntington et al., 2011), and paleo-altimetry (Huntington et al., 2010; 2015). However, while useful for determining the temperatures of carbonate mineral precipitation, clumped isotope temperatures (T(Δ_{47})) are subject to change via reordering of the C-O bonds within the solid-state mineral lattice when exposed to elevated temperatures (Passey & Henkes, 2012; Henkes et al., 2014; Stolper & Eiler, 2015). This tendency allows for the investigation of burial temperatures rather than depositional or cementation paleotemperature (Shenton et al., 2015).

Clumped Isotope Reordering

As carbonates are heated, solid-state diffusion of oxygen atoms throughout the mineral lattice decreases the Δ_{47}, moving towards an equilibrium with the ambient burial temperature

(Dennis & Schrag, 2010; Passey & Henkes, 2012; Stolper & Eiler, 2015). Reordering is a kinetically controlled process, with faster reordering rates at higher temperatures. Multiple studies have sought to investigate the kinetics of calcite clumped isotope reordering, and different models propose slightly varying kinetic relationships (Passey & Henkes, 2012; Henkes et al., 2014; Stolper & Eiler, 2015).

The models proposed by Passey & Henkes (2012) and Henkes et al. (2014) are founded on the hypothesis that crystallographic defects are the primary pathways through which reordering proceeds, driving **Eq. 1** to the right. These authors identify two types of crystallographic defects within the mineral lattice, annealable (transient) defects and non-annealable (equilibrium) defects. The Passey and Henkes (2012) model, hereby referred to as the Linear Approximation Model (LAM), only considers equilibrium defects, postulating that transient defects are annealed very quickly during heating and do not contribute significantly to the reordering process. The governing equation for the first order approximation is as follows:

$$\ln\left[\frac{\Delta_{47}^{t}-\Delta_{47}^{eq}}{\Delta_{47}^{init}-\Delta_{47}^{eq}}\right] = -tK_0e^{\left(\frac{-E_a}{RT}\right)} \quad (3)$$

The model allows for the prediction of changes in Δ_{47} as a function of temperature T (kelvin), time t spent at given temperature, and the Arrhenius parameters, frequency factor (K_0) and activation energy (E_a), for the material under study. The Henkes et al. (2014) model is a more advanced model that considers both the transient and equilibrium defects within the lattice and models the change in Δ_{47} as a function of temperature and time:

$$\ln\left(\frac{\Delta_{47}^{t}-\Delta_{47}^{eq}}{\Delta_{47}^{init}-\Delta_{47}^{eq}}\right) = -tK_ce^{\left(\frac{-E_c}{RT}\right)} + \left(\frac{K_de^{\left(\frac{-E_d}{RT}\right)}}{K_2e^{\left(\frac{-E_2}{RT}\right)}}\right)\left[e^{-tK_2e^{\left(\frac{-E_2}{RT}\right)}-1}\right] \quad (4)$$

There are three pairs of Arrhenius parameters to consider (K_c, E_c; K_d, E_d; and K_2, E_2) each pair

representing the equilibrium defect component (c), the transient defect component (d), and the annealing rate of transient defects (2). Partial reordering takes place when minerals do not reach these temperatures for sufficient time to fully reorder (Henkes et al., 2014; Shenton et al., 2015).

Stolper & Eiler (2015) model exchange between neighboring carbonate ion groups as an additional control on reordering. Simply put, a clumped bonded pair cannot form unless the necessary rare isotopes are located adjacent to each other in the crystal lattice. Furthermore, during reordering, a carbonate clumped isotopologue dissociates by exchanging one of its rare isotopes with abundant, common isotopes in a neighboring carbonate group. However, once dissociated, the clumped bond is relatively more likely to reform due the fact that ^{13}C and ^{18}O atoms are close to one another. Therefore, diffusion of oxygen atoms away from the neighboring ^{13}C-bearing carbonate ion is an additional control on the kinetics of reordering. The chemical equation is as follows:

$$Ca^{12}C^{16}O_3 + Ca^{13}C^{18}O^{16}O_2 \leftrightarrow pair \leftrightarrow Ca^{12}C^{18}O^{16}O_2 + Ca^{13}C^{16}O_3 \quad (5)$$

Referred to as the Paired Diffusion Model (PDM), this model depends on two separate reactions, the exchange of ions from clumped molecules to an intermediary "pair", and then a subsequent diffusion to unpaired ion groups, or "singletons". When a clumped isotopologue exchanges with a neighboring commonly-substituted carbonate molecule, it will form a "pair" of two singly substituted carbonate molecules ($^{13}C^{16}O_3^{2-}$, $^{12}C^{18}O^{16}O_2^{2-}$) that reside directly next to each other in the crystal lattice. To then become a singleton, the singly substituted ion groups must diffuse away until they are not surrounded by any other singly-substituted ion groups in the crystal lattice, making it impossible for a clumped molecule to form again. The equation for the first reaction, the dissociation of clumped molecules to pairs is:

$$\frac{\partial[^{13}C^{18}O^{16}O_2^{2-}]}{\partial t} = K_f\left([^{12}C^{16}O_3^{2-}]\,[^{13}C^{18}O^{16}O_2^{2-}]_t + K_b[pair]_t\right) \quad (6)$$

The second equation models the diffusion of pairs away into singletons:

$$\frac{\partial[pair]}{\partial t} = K_f\left([^{12}C^{16}O_3^{2-}]\,[^{13}C^{18}O^{16}O_2^{2-}]_t\right) - K_b[pair]_t + K_{diff-single}[^{12}C^{18}O^{16}O_2^{2-}]_{single,0} *$$

$$[^{13}C^{16}O_3^{2-}]_{single,0} - K_{diff-pair}[pair] \quad (7)$$

These two equations contain four reaction rate constants (K_f, K_b, $K_{diff\text{-}single}$, and $K_{diff\text{-}pair}$) all of which can be solved based on temperature and the $\delta^{13}C$ and $\delta^{18}O$ values of the sample, both of which are assumed to remain constant through time. The two reactions do not progress at the same rate, nor do they begin at the same temperature. Therefore, in geologically relevant scenarios, the dissociation of clumped molecules to pairs progresses before pairs can diffuse to singletons. This can create a stepwise reordering pathway depending on the rate of burial and heating, as seen in **Figure 2.**

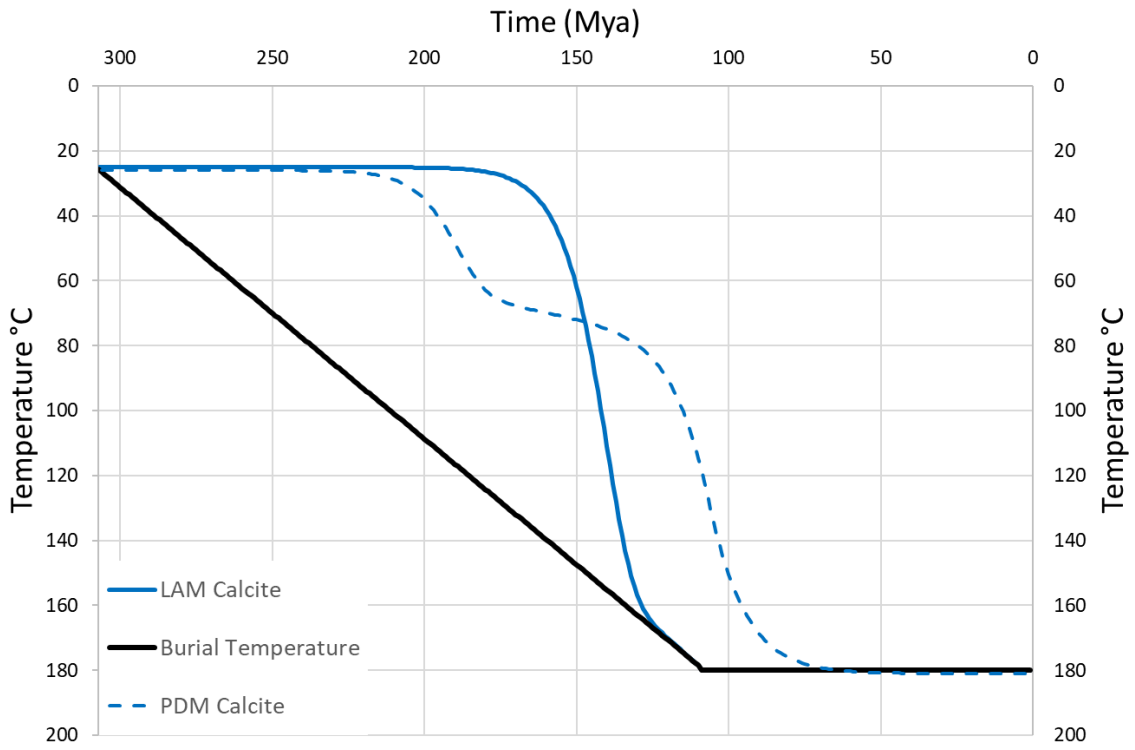

Figure 2- Clumped isotope reordering pathways based on Passey & Henkes (2012) & Stolper and Eiler (2015)

Retrograde reordering of clumped isotopes during cooling/exhumation can change the measured value to represent a temperature below the maximum burial temperature. The kinetic relationship for reordering applies whether the sample is being heated or cooled. At higher temperatures (e.g., >200 °C) reordering proceeds very quickly relative to geologic time scales. In contrast, reordering becomes rate-limited at lower temperatures, with a kinetic threshold of ~100°C (PDM) and an "apparent equilibrium blocking temperature," analogous to a closure temperature where clumped isotope reordering stops and values are locked in during cooling, of ~150°C (Henkes et al., 2014; Stolper & Eiler, 2015). Furthermore, recent work (Lloyd, 2018; Lloyd & Eiler, 2014) suggests that dolomite reorders its clumped isotope values more slowly than calcite. In other words, calcite and dolomite samples that experience the same burial history will not show the same reordered clumped isotope temperature. The dolomite will appear cooler due to

the slower kinetics of the reordering reaction. An estimate based upon Lloyd (2018) suggests that the Arrhenius parameters of dolomite are roughly 30% higher than those of calcite of the PDM. Practically speaking, this means that dolomite would not be expected to significantly reorder until reaching approximately 180°C. To reproduce this behavior in the LAM, the Arrhenius parameters must be increased 15% in both E_a and K_0 (See **Table 1**).

Table 1- Arrehnius parameters (LAM) and reaction rate constants (PDM) used for THRMs

LAM, Calcite	
Frequency factor (K_o)	4.45×10^8
Activation energy (E_a)	188,000 (J)
LAM, Dolomite	
Frequency factor (K_o)	5.1175×10^8
Activation energy (E_a)	216,200 (J)
PDM, Calcite	
K_f	$(\exp((-20700/297.15)+20.1))*3.1556736*10^{13}$
K_{diffs}	$(\exp((-25400/297.15)+24.7))*3.1556736*10^{13}$
PDM, Dolomite	
K_f	$(\exp(((-20700*1.30)/347.15)+20.1))*3.1556736*10^{13}$
K_{diffs}	$(\exp(((-25400*1.30)/347.15)+24.7))*3.1556736*10^{13}$

Only recently have researchers begun to apply clumped isotopes to better understand basin thermal histories. Macdonald et al. (2017) compared clumped isotope temperatures to fluid inclusion temperatures from core samples to constrain the thermal history of the Pinda formation offshore Angola, a productive hydrocarbon reservoir. Recognizing a difference in the clumped isotope temperature and the fluid inclusion temperature data, the authors interpreted the clumped isotope temperature to represent deep burial recrystallization of dolomite. Because fluid inclusion data matched closely to current ambient well temperatures, the authors interpreted the fluid inclusion data as being recently reset. This study highlights the ability of clumped isotopes

to refine thermal histories, especially when used in conjunction with complementary techniques. John (2015) used clumped isotopes to constrain the burial depth of an outcrop of the Qishn formation in Oman. The Qishn formation is a productive hydrocarbon horizon across the Arabian Peninsula. By comparing clumped isotope values of unaltered and partially neomorphosed oyster samples, John (2015) was able to revise the interpreted minimum burial depth to at least a kilometer, a depth and temperature regime that is in line with conodont alteration index data in the region. Lawson et al. (2017) combined clumped isotope thermometry with U-Pb dating to evaluate the burial and diagenetic history El Abra Formation of Mexico. The El Abra formation is one of the many productive units within the Tampico embayment oil fields of Mexico (Enos et al. 1997). The authors analyzed different generations of cementation and determined that reordering was necessary to explain the elevated clumped temperature signal, and linked the major cementation phase with burial on the order of 3800 m and contemporaneous with Laramide-related tectonics. As these studies show, clumped isotope thermometry provides an exciting new tool for the investigation of basin thermal histories, and the Permian Basin of Texas and New Mexico is a prime location where this technique can be applied to further aid the oil industry in its pursuits.

Geologic Background

The Permian Basin is subdivided into two major sub-basins, the Delaware (western) and Midland (eastern) Basins, which are separated by the Central Basin Platform (**Fig. 3**). Associated with the Late Paleozoic Ancestral Rocky Mountains, the Permian basin formed as a result of the collision between Gondwana and Laurentia (Kluth & Coney, 1981). Much of the Permian Basin

consists of marine sediments, including siliciclastic rocks, organic-rich silt- and mudstones, as well as carbonates representing deposition from the Precambrian through the Cenozoic (**Fig. 4**). The main sources of carbonates in the basin are the Central Basin Platform and the Northwest shelf. Of particular interest to this project are the formations spanning the Ordovician though Permian, consisting of the Ellenberger, Montoya, Devonian, Pennsylvanian, Mississippian Lime, and the Bone Springs Carbonates. The carbonates that make up these formations are a combination of in situ growth and detritus shed from the Central Basin Platform and basin margins. These formations are not all laterally extensive across the entire basin, as many are sourced from detrital carbonate material from the basin margins. The most extensively dolomitized formation is also the most deeply buried, the Ellenberger formation, which has long been a productive hydrocarbon-producing horizon (Smith 1979).

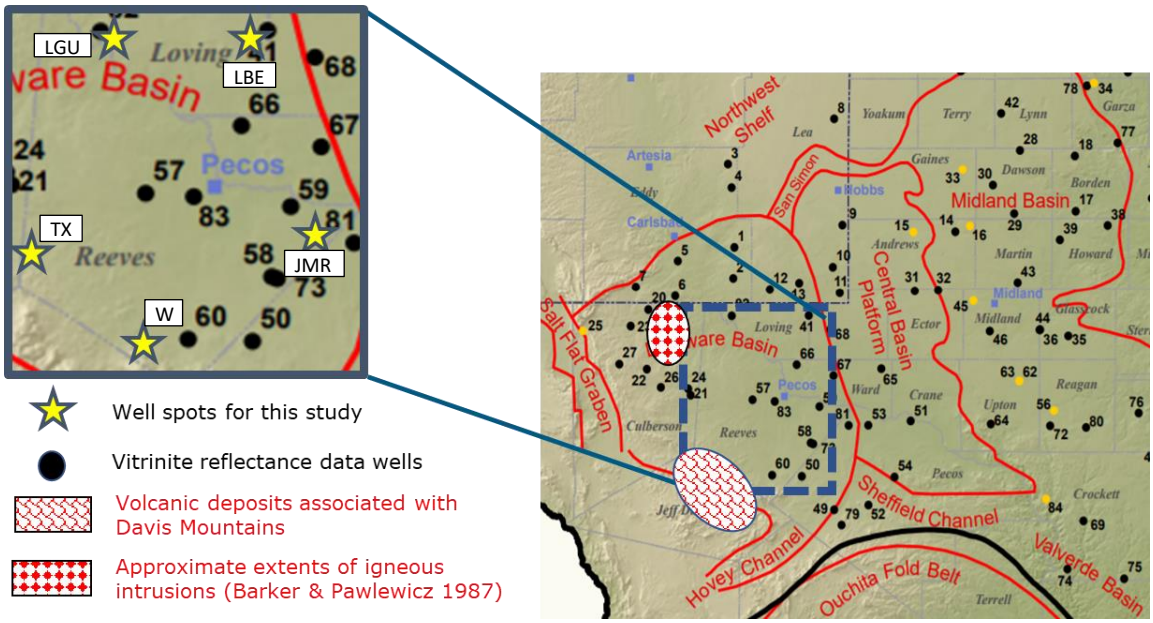

Figure 3-Generalized map of the Permian Basin, highlighting locations of well spots for this study as well as Barker and Pawlewicz (2001) (Reprinted and modified from Barker and Pawlewicz 2001). Approximate locations of igneous intrusions (Barker and Pawlewicz 1987) and the location of the Davis Mountains volcanics. LGU (Lago Unit #1), TX (Texaco #1-29), W (Weinacht #1), JMR (Rape, J.M. #1), LBE (Lineberry Evelyn #1).

A persistently unresolved question within the Delaware Basin is an anomalous gas/oil ratio that increases to the western portions of the basin despite shallower modern burial depths. One would expect more deeply buried sediments and the associated organic matter to be more gas prone because they presumably experience higher burial temperatures. Two possible explanations for the observed gas/oil ratio trends are (1) burial and subsequent exhumation of the western portion of the Delaware Basin and (2) higher geothermal gradients associated with a thermal source in the western portion of the basin. Barker & Pawlewicz (1987) identified Cenozoic intrusions in the western portion of the basin (**Fig. 3**). Furthermore, the Davis Mountains lie along the western boundary of the Delaware Basin and represent the remnants of a Paleogene volcanic field. Hills (1984) explored the modern geothermal gradient using petrophysical logs and found an average of roughly 25°C/km. Furthermore, Hills (1984) observed that there were two different gradient regimes within the wells, with the delineation between them being the evaporates that overlie the Delaware mountain group. Interestingly, from Hills' (1984) figures, the three wells with the highest geothermal gradients are all found along the western extent of his study area. Kinley et al. (2008) explored the hydrocarbon potential of the Barnett Shale in the Delaware Basin and saw a drastic increase in vitrinite reflectance values locally around the subsurface intrusions identified by Barker & Pawlewicz (1987) (**Fig. 5**). As the western-most wells for this study are ±30 miles away from the mapped intrusions, they may or may not record an increased geothermal gradient associated with these intrusions.

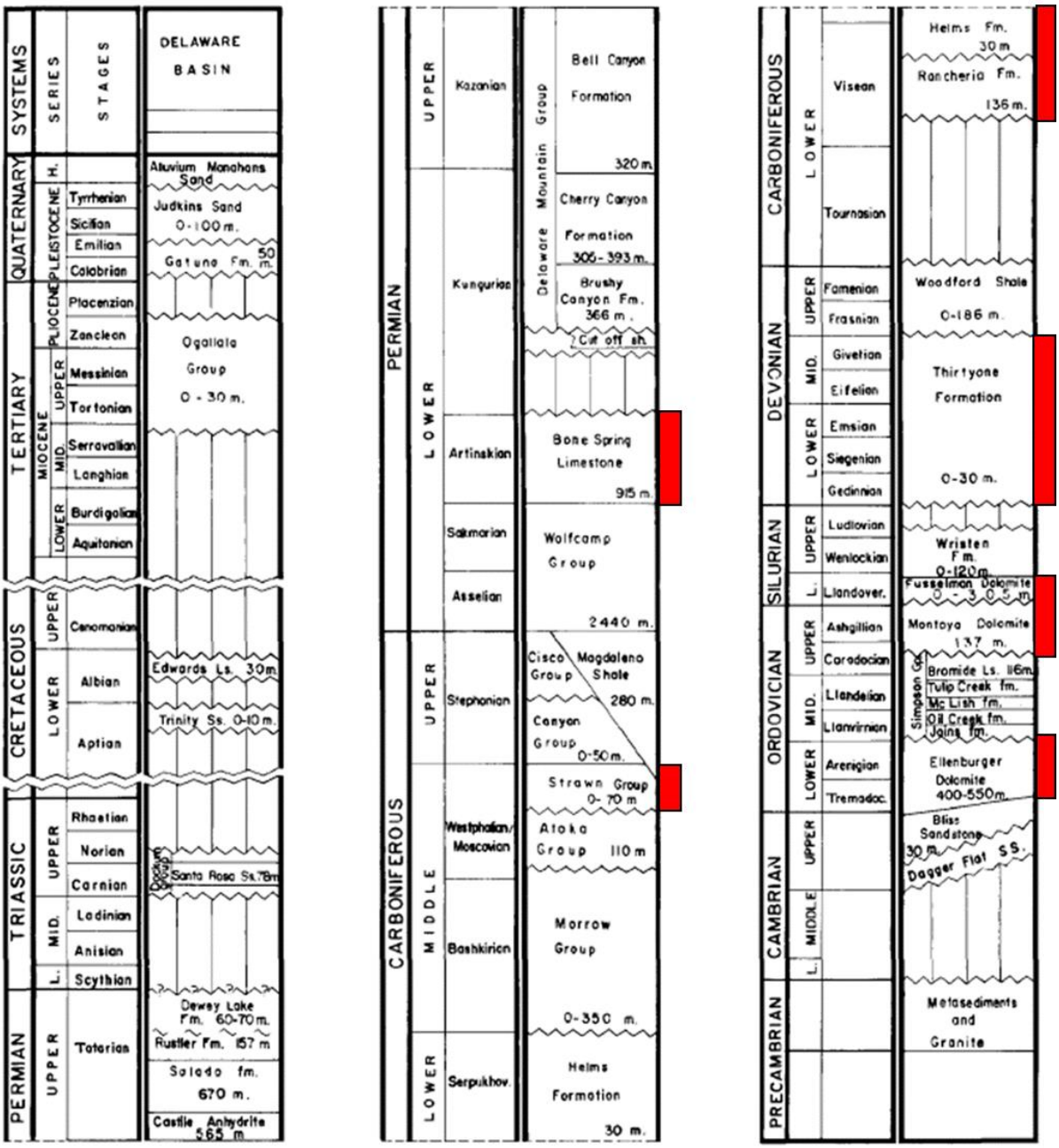

Figure 4- Generalized stratigraphic column of the Delaware Basin (Reprinted and modified from Hills 1984). Red bars mark formations that have been sampled for this study.

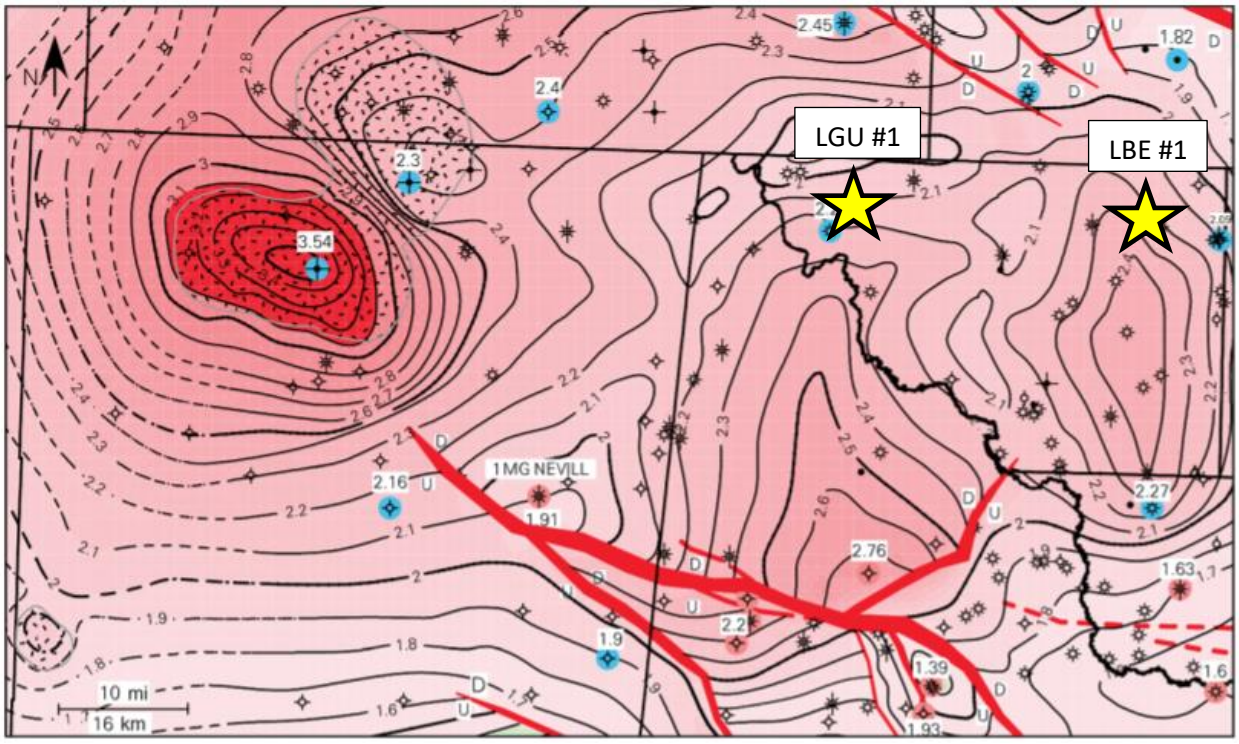

Figure 5- Map of vitrinite reflectance values (Ro%) of the Barnett shale across the central portion of the Delaware Basin (Reprinted and modified from Kinley et al. 2008). LGU #1 = Lago Unit #1. LBE #1 = Lineberry Evelyn #1. The Texaco #1-29 is just off the map to the South. Weinacht #1 and Rape, J. M. #1 are off the map to the southeast.

METHODS

Sample Collection and Screening

Samples from five wells (see **Table 2** for location/ identification), following a circular pattern covering the central and eastern portions of the basin, were collected from the Bureau of Economic Geology (BEG) Core Repository at the University of Texas at Austin. The sample material represents drill cuttings that were collected at the time of drilling and housed at the BEG since the well was completed. At the time of drilling, the cuttings were bagged in 10 ft intervals. Due to the nature of cuttings within a well bore, there are factors such as cuttings recycling and mud circulation timing that must be approximated; therefore, cuttings are a less precise representation of a formation of interest than a core would be. Unfortunately, the appropriate cores were not available. The size of the cuttings ranged between fine powder and 5 mm. Cuttings that were of a sufficient size (>1 mm diameter) were imbedded in epoxy billets and abraded to reveal a clean surface. The cuttings were screened using a Phenom XL scanning electron microscope (SEM) with energy dispersive spectroscopy (EDS) (15 kV Accelerating voltage, low vacuum, map mode) to determine mineral content and lithology, and to identify evidence of diagenetic alteration (see **Appendix B** for screening details). The carbonate material picked for each sample was finely powdered and homogenized using a mortar and pestle.

Table 2- Location and Identification information for the 5 wells sampled as part of this study

Well name	County (TX)	API Number	Spud Date	TD (ft)	Survey	Latitude (NAD 27)°	Longitude (NAD 27)°
LINEBERRY, EVELYN #1	Loving	423011017000	12/31/64	22,456	SEC 3/BLK 75/1320' FEL & 430' FSL	31.9186841	103.3317174
RAPE, J.M. #1	Reeves	423891049600	02/01/68	18,500	SEC 2/BLK C-2/1168' FNL & 900' FEL	31.2556722	103.1377006
TEXACO #1-29	Reeves	423891055200	10/31/68	10,935	SEC 29/BLK 58/1980' FSL & 1980' FWL	31.1895525	-104.0686863
WEINACHT #1	Reeves	423893155700	03/27/85	12,850	SEC 1/BLK 55/660' FNL & 1200' FEL	30.8928944	-103.6778147
LAGO UNIT 1	Loving	423013004500	Unknown	19,153	SEC 34/BLK 56-T/1320' FWL & 1320' FSL	31.916198	-103.851108

Isotopic Analysis

Isotopic analyses ($\delta^{13}C$, $\delta^{18}O$, and Δ_{47}) were performed on a ThermoFisher Scientific 253 Plus isotope ratio mass spectrometer (IRMS) housed in the Stable Isotope Geoscience Facility (SIGF) at Texas A&M University. Approximately 100-120 μg of carbonate material were weighed for each clumped isotope analysis. Larger sample weights were employed for samples with lower percent calcite or dolomite to give the same yield. A Kiel IV automated carbonate reaction system (ThermoFisher Scientific) was used to produce and purify the CO_2 gas for analysis at a temperature of 70°C. The addition of a tertiary trap (1/4 inch outside diameter) filled with a one inch length of Poropak Q resin (Waters corp, 50-80 mesh) and 99.9+% silver wool, held at a constant temperature of -20 °C, was fitted to the Kiel system as an additional barrier to organic material, sulfur compounds, and chlorinated hydrocarbons, all of which could interfere with the *m/z* 47 analysis.

Standardization and Correction

The primary means of standardization is based on the methods in Meckler et al. (2014). The data were placed into the absolute reference frame (ARF) (Dennis, 2011). The absolute reference frame eliminates a mass spectrometer artifact within the measurement that creates a

dependent relationship between δ^{47} and Δ_{47}, which should not exist based on theoretical predictions. Carbonate standards ETH 1-4 (courtesy of Dr. Stefano Bernasconi, ETH Zurich) were utilized for calibration. The four standards consist of two isotopically distinct carbonate powders (ETH 3 & 4), each with an aliquot heated at high temperature (>600°C) for a sufficient time for the Δ_{47} to reorder and reach equilibrium with the new temperature (ETH 1 & 2). This calibration of heated and unheated samples allows correction for the dependent relationship between δ^{47} and Δ_{47}. A moving correction scheme, consisting of the five most recent of each standard before and after each sample replicate, was applied as the correction window.

A pressure baseline (PBL) measurement is an additional corrective step necessary for clumped isotope analysis (He et al., 2012; Bernasconi et al., 2013). The PBL corrects for negative voltages seen in the *m/z* 47 Faraday cup from secondary electrons generated by the *m/z* 44 ion beam (Bernasconi et al., 2013). Furthermore, an acid fractionation correction must be made for the reaction temperature of 70°C, as previous studies on which paleotemperature equations are based have used reaction temperatures of 25°C and 90°C. Replicates were screened using a multiple protocols as a means of QA/QC. Any replicate that had an initial voltage balance mismatch of greater than 300 mV was discarded. This mismatch would lead to poor precision as a function of the depletion rates of the sample gas. Furthermore, any replicate with a $\delta^{13}C$ or $\delta^{18}O$ value that fell greater than 2σ away from the mean of that sample was discarded, regardless of the Δ_{47} value. Peirce's criterion was then used to determine outliers in the remaining Δ_{47} data set, which were subsequently removed (Ross, 2003).

Clumped isotope temperatures ($T(\Delta_{47})$) have been calculated using the universal carbonate equation from Bonifacie et al. (2017), which is modified below to include the 70°C acid fractionation correction (Defliese et al., 2015):

Δ_{47} = 0.0422 (±0.0019) * 10^6 / T^2 + 0.2082 (±0.0207)

where T is temperature in kelvin.

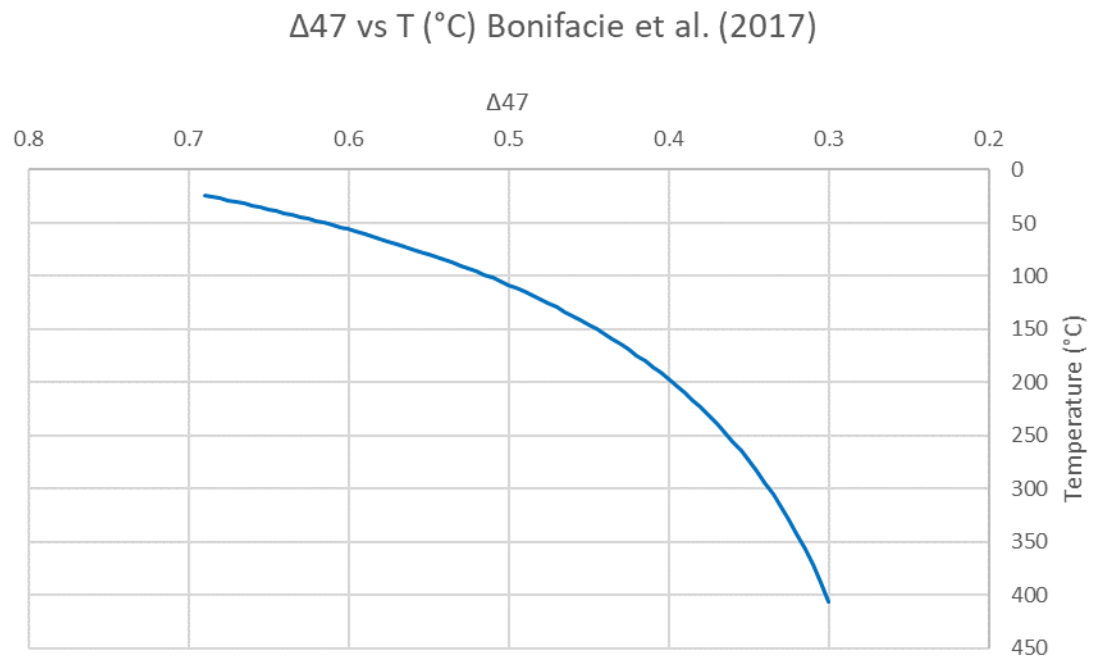

Figure 6- Plot of Δ_{47} vs. temperature for the universal carbonate equation from Bonifacie et al. (2017) modified to include the 70°C acid correction factor (Defliese et al. 2015).

RESULTS

The isotopic results for the five wells in this study are presented in **Table 3**

Table 3- Isotopic results of samples. Depths are measured depths where the cuttings were bagged. Blue highlighting indicates the sample is calcite. Yellow highlighting indicates the sample is dolomite.

*** indicates ± the 95% confidence interval of the measurement.*

Well Name	ID	N # Replicates	Depth (ft)	Depth (m)	$\delta^{13}C$ VPDB ‰ **	$\delta^{18}O$ VPDB ‰ **	Δ_{47} CDES **	Δ_{47} T (°C) (Bonifacie et al. 2015)	Δ_{47} T (°C) 95% CI Range
Rape, J. M. #1	JMR-1	13	12,950	3,948	3.29 ± 0.06	-1.34 ± 0.12	0.477 ± 0.039	124	97-157
	JMR-2	10	15,750	4,802	-0.24 ± 0.08	-4.97 ± 0.19	0.421 ± 0.053	173	126-241
	JMR-3	11	18,350	5,595	-1.82 ± 0.04	-6.11 ± 0.06	0.476 ± 0.055	125	90-172
Lineberry Eveleyn #1	LB-1	10	15,660	4,774	3.28 ± 0.04	-3.12 ± 0.25	0.421 ± 0.078	173	109-286
	LB-2	15	18,530	5,649	2.50 ± 0.02	-4.83 ± 0.02	0.335 ± 0.055	305	236-815
	LB-3	10	20,300	6,189	1.46 ± 0.04	-7.65 ± 0.06	0.351 ± 0.025	272	229-329
	LB-4	12	22,230	6,777	-1.40 ± 0.02	-6.24 ± 0.04	0.446 ± 0.043	149	115-192
Lago Unit #1	LG-3	12	7,320	2,232	0.83 ± 0.02	-4.86 ± 0.08	0.674 ± 0.049	29	15-46
	LG-1	15	13,600	4,146	1.40 ± 0.08	-3.52 ± 0.08	0.400 ± 0.088	197	116-368
	LG-2	8	16,300	4,970	0.31 ± 0.06	-7.56 ± 0.14	0.477 ± 0.057	124	89-173
Texaco #1-29	TX-1	11	7,200	2,195	0.77 ± 0.10	-2.41 ± 0.08	0.507 ± 0.063	104	69-151
	TX-2	11	8,800	2,683	1.09 ± 0.02	-5.13 ± 0.06	0.460 ± 0.059	137	96-195
	TX-3	12	9,750	2,973	-0.54 ± 0.06	-4.94 ± 0.08	0.429 ± 0.069	165	109-255
	TX-4	15	10,800	3,293	-1.40 ± 0.04	-4.76 ± 0.10	0.460 ± 0.088	137	79-237
Weinacht #1	W-1	10	7,050	2,149	3.44 ± 0.06	-0.91 ± 0.06	0.513 ± 0.047	100	74-132
	W-2	10	8,350	2,546	-10.0 ± 0.06	-2.58 ± 0.18	0.684 ± 0.047	26	12-42
	W-3	9	11,000	3,354	0.07 ± 0.04	-5.22 ± 0.02	0.425 ± 0.076	169	107-278
	W-4	10	12,660	3,860	-1.92 ± 0.02	-6.34 ± 0.10	0.554 ± 0.068	77	47-119

The results are reported as the mean isotopic value, with an error representing the 95% confidence interval. Note that the 95% confidence interval for Δ_{47} T(°C) is not symmetrical about the mean value; this is because the relationship between Δ_{47} and temperature is not linear

(**Fig. 6**). Carbonate Δ_{47} values range between 0.335 ± 0.055 ‰ and 0.684 ± 0.047 ‰, corresponding to temperatures ranging from 304°C (236-815°C) and 26°C (12-42°C) using Bonifacie et al. (2017). In every well, the deepest buried sample is a dolomite, and in every case it yields and apparent clumped isotope temperature that is lower than the next most deeply buried calcite. Other than this fact, temperature generally increases with depth with the exception of two samples which are discussed in a later section.

DISCUSSION

Given that all of the samples are taken from kilometers beneath the surface, it is not surprising that only two samples (LG-3 and W-2) yield clumped isotope temperatures reflective of surface conditions (29°C and 26°C respectively). All other samples yield apparent clumped isotope temperatures higher than original precipitation temperature, and are interpreted to reflect burial heating reordering and/or recrystallization temperatures at depth. The general trend of increasing apparent clumped isotope temperatures with depth is consistent in all of the wells, with the exception of samples that are dolomite (highlighted in yellow in **Table 3**). Dolomite samples representing the deepest samples consistently record cooler apparent clumped isotope temperatures than the next deepest calcite samples. This is interpreted to result from differences in reordering kinetics between calcite and dolomite. Dolomite reorders at a slower rate than calcite (Lloyd 2018; Lloyd & Eiler 2014), and accordingly for a given time-temperature history, the reordered apparent clumped isotope temperature will progress more slowly and potentially less completely towards the equilibrium temperature than would calcite. I used burial history curves (**Fig. 7**) provided by the Texas A&M Chevron Center of Research Excellence (CoRE) for each individual well as a starting point for estimating the time-temperature history of the samples and the expected reordering (Mauro Becker, personal communication, 2018). The CoRE histories are based on work done by Sinclair (2007) who used apatite fission track thermochronology to create burial history curves for the basin.

Thermal History Reordering Models (THRMs)

Two thermal history reordering models "THRMs" (Shenton et al., 2015) were used to evaluate the extent of C-O bond reordering for each of the sample depths in the five wells. First, a burial curve was established for each sample based on the plots provided by the Chevron CoRE and a time-temperature history was created by linearly applying a paleo-geothermal gradient that could be varied. The models were initialized at the age of the formation, which ranged from the Ordovician to the Permian. The Linear Approximation Model (LAM) is based on **Equation 3** from Passey & Henkes (2012), which utilizes a first order approximation of reordering kinetics. It represents a sequential time step evolution of Δ_{47} based on the time-temperature history of the sample. The Arrhenius parameters used were those for the Permian brachiopod from Passey and Henkes (2012), and the time steps were 1 million years. This model requires an assumption of the initial clumped isotope value, which was set at 0.686, equivalent to 25°C using Boniface et al. (2017).

The Paired Diffusion Model (PDM) of Stolper & Eiler (2015) assumes a two-part reaction of clumped isotopes dissociating to pairs and then a second reaction of pairs dissociating to singletons (**Eq. 6 & 7**). The time steps used were again 1 million years. This model requires the input of the initial temperature, which was again set at 25°C (Δ_{47} = 0.686), as well as the $\delta^{13}C$ and $\delta^{18}O$ of the sample. The $\delta^{13}C$ and $\delta^{18}O$ values are necessary for the calculation of the initial concentration of pairs. An assumption of the model is that the $\delta^{13}C$ and $\delta^{18}O$ values do not change over time. This model requires the simultaneous solving of two ordinary differential equations, and as such was programmed in "R" using the package "deSolve" (R Core Team 2018; Soetaert et al. 2010; William Defliese, personal communication, 2018).

Initial Precipitation Temperatures

Both THRMs require an input of initial Δ_{47} T(°C), which was set at 25°C. It is considered a necessary simplification to make this assumption. Given that only two of the samples are interpreted to record initial precipitation temperatures, there is limited ability to back calculate the isotopic composition of formation waters using the clumped isotope measurement. The $\delta^{18}O$ values for those two samples (LG-3 and W-2) were -4.86‰ and -2.58‰ VPDB. Using clumped isotope temperatures and the oxygen isotope paleothermometer of Hays and Grossman (1991, modified from O'Neil et al., 1969) yields calculated $\delta^{18}O$ compositions of the water of approximately -1‰ and 0‰ VSMOW respectively. The average $\delta^{18}O$ of all non-dolomite samples is approximately -3.5‰ VPDB. Using an isotopic composition of formation waters ranging from 1‰ and 0‰ VSMOW yields formation temperatures ranging from 25°C to 30°C using Hays and Grossman (1991).

It is unlikely that these sediments have undergone no recrystallization throughout their history, with isotopic exchange with diagenetic fluids very likely, but identifying and accounting for this recrystallization in the modeling would be very difficult, especially considering the sample material is comprised of cuttings. Better evaluation of recrystallization might be more possible with cores, but depth of recrystallization would likely remain difficult to determine. Recrystallization would serve to reset the Δ_{47} of each sample, which would in turn bring the value closer to the final reordered value. This in effect would lower the necessary burial temperature over time to reach the final value. If the sample is modeled to have reordered to equilibrium with the burial temperature, any recrystallization will have no effect on its calculated geothermal gradient.

Data-Model Fitting and Determination of Paleo-Geothermal Gradients

For each sample, the unique time-temperature history was varied by changing the linear geothermal gradient applied to the burial curve iteratively until the modeled, reordered Δ_{47} matched the measured value for the sample. Examples of different reordering pathways produced by varying the paleo-geothermal gradients in both models are shown in **Fig. 8 A&B.**

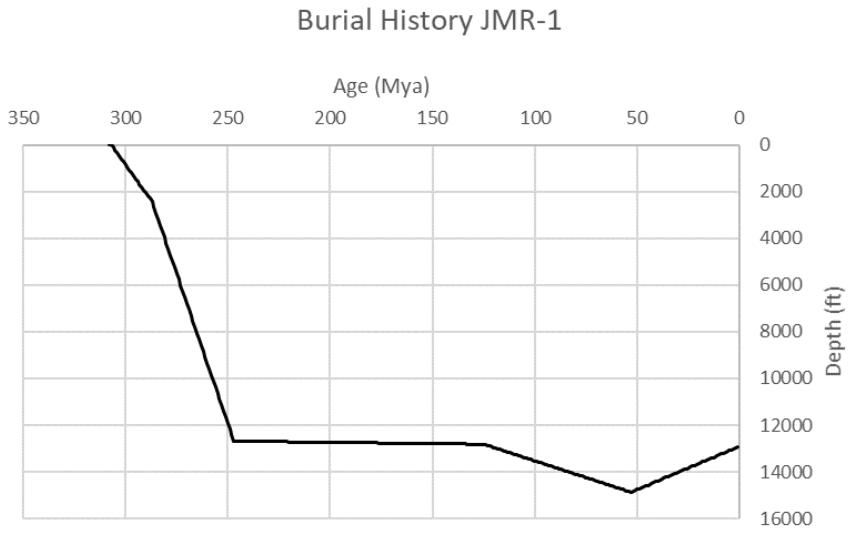

Figure 7- Burial history of the JMR-1 sample (Personal communication, Mauro Becker, 2018).

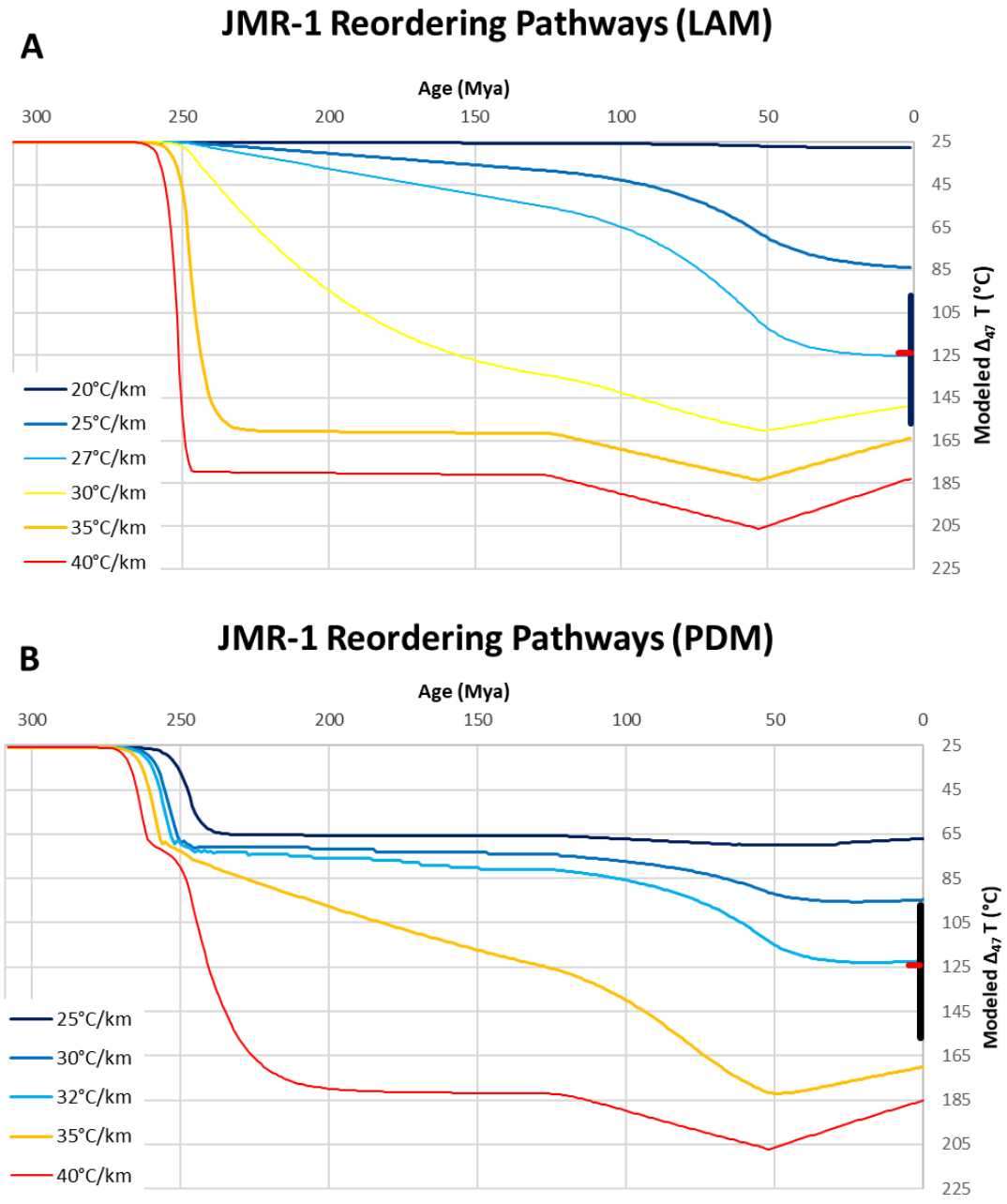

Figure 8 A&B- Different clumped isotope reordering pathways based on varied geothermal gradients for JMR-1. A) Linear Approximation Model (LAM) based on Passey and Henkes (2012). B) Paired Diffusion Model (PDM) based on Stolper and Eiler (2015). The black bar represents the 95% confidence interval of the reordered T(Δ_{47}), and the red mark within represents the mean measured value of T(Δ_{47}).

This process was used for both models to determine the best-fit geothermal gradient (BFGG).

Note that I am assuming a simple, constant geothermal gradient, therefore the BFGG should be

thought of as a time-averaged geothermal gradient. The resulting BFGGs are summarized in **Table 4** along with the modeled maximum burial temperature that corresponds to the time-temperature history using the BFGG.

When comparing the two estimates of dolomite reordering kinetics, the PDM produces BFGGs that are more consistent with calcite data than the LAM, which produces significantly lower BFGGs. There is an even better fit if a dolomitization/recrystallization temperature of approximately 75-100°C is assumed. These temperatures are within the estimated range of burial dolomitization (Tucker & Wright, 1990) and the estimated temperature of dolomitization of the Ellenberger formation in the Permian Basin based on fluid inclusion data (Kupecz & Land, 1991). The equivalent depth of dolomitization based on this study's modeling of paleo-geothermal gradients is roughly 2-3 km, which is in agreement with previous studies of the Ellenberger formation in the Permian Basin by Lee & Friedman (1987) and Kupecz & Land (1988). The present study uses a rough approximation of the reordering kinetics of dolomite, but the resulting paleo-geothermal gradients fit well with the better constrained calcite reordering kinetics as well as with vitrinite reflectance data that are available for two of the five wells.

*Table 4- Results for data-model fitting. *Indicates a recrystallization temperature of 75°C was used. ^Indicates a maximum geothermal gradient, not a BFGG. "Indicates a Max Burial Temperature calculated using the well's average GG not the BFGG (see discussion for reasoning). Blue and yellow represent calcite and dolomite respectively.*

ID	Present Measured Depth (ft)	Modeled Max Burial Depth (ft)	Δ_{47} CDES **	Δ_{47} T (°C) (Bonifacie et al. 2015)	Δ_{47} T (°C) 95% CI Range	LAM BFGG (°C/km)	PDF BFGG (°C/km)	Max Burial T (LAM) °C	Max Burial T (PDF) °C
JMR-1	12,950	14,900	0.477 ± 0.039	124	97-157	27	32	147.7	170.4
JMR-2	15,750	17,600	0.421 ± 0.053	173	126-241	30	30	186.0	186.0
JMR-3	18,350	20,300	0.476 ± 0.055	125	90-172	28	35*	198.3	241.6
						28 ± 1.5	**32 ± 2.5**		
LB-1	15,660	16,057	0.421 ± 0.078	173	109-286	31	31	176.8	176.8
LB-2	18,530	18,930	0.335 ± 0.055	305	236-815	49	49	307.8	307.8
LB-3	20,300	20,600	0.351 ± 0.025	272	229-329	39	40*	269.9	276.2
LB-4	22,230	22,650	0.446 ± 0.043	149	115-192	25	37*	197.6	280.5
						36 ± 10.5	**39 ± 7.5**		
LG-3	7,320	11,100	0.674 ± 0.049	29	15-46	47^	38^	143.5"	153.6"
LG-1	13,600	17,300	0.400 ± 0.088	197	116-368	40	40	236.0	236.0
LG-2	16,300	20,000	0.477 ± 0.057	124	89-173	30	40*	209.5	268.9
						35 ± 8.4	**40 ± 1.2**		
TX-1	7,200	10,500	0.507 ± 0.063	104	69-151	40	47	153.0	175.5
TX-2	8,800	12,100	0.460 ± 0.059	137	96-195	36	42	157.8	179.9
TX-3	9,750	13,100	0.429 ± 0.069	165	109-255	46	42	208.7	192.7
TX-4	10,800	14,100	0.460 ± 0.088	137	79-237	44	45	214.1	218.4
						41.5 ± 5.0	**44 ± 2.4**		
W-1	7,050	8,900	0.513 ± 0.047	100	74-132	40*	41*	133.2	135.0
W-2	8,350	10,200	0.684 ± 0.047	26	12-42	35^	30^	133.8	149.4
W-3	11,000	12,900	0.425 ± 0.076	169	107-278	42	41	190.2	182.3
W-4	12,660	14,500	0.554 ± 0.068	77	47-119	40	40*	201.8	201.8
						40 ± 1.2	**41 ± 0.6**		

Rape, J. M. #1

Situated at the southeastern portion of the basin, the Rape, J. M. #1 is characterized by deep burial of the formations of interest, with samples found at depths from 13,000 to 18,000 ft measured depth (MD). The BFGGs for each sample depth are somewhat consistent across both models. This is because of the significant burial depth, as both models predict that reordering equilibrium is reached early within the burial history, and therefore the rates at which equilibrium is reached is the only main difference between the models. The LAM predicts an average geothermal gradient of 28 °C/km based on the three sample depths, whereas the PDM predicts a slightly warmer geothermal gradient of 32 °C/km. This easternmost well location yields the lowest average geothermal gradients.

Lineberry Evelyn #1

Situated at the northeastern portion of the basin, the Lineberry Evelyn #1 also experienced very deep burial in excess of six kilometers. There is more variability in the BFGGs of each sample depth location, and this may reflect the lower temperature sensitivity of clumped isotopic compositions at the high temperatures that these samples record. LB-2 (18,530' MD) records a T(Δ_{47}) of over 300°C. This temperature is higher than any other T(Δ_{47}) recorded within the wellbore despite only being the third deepest sample. While the Δ_{47} of this sample does not have a standard error significantly higher than that of the other samples, the temperature range represented by that standard error is much larger due to lower temperature dependence between Δ_{47} and temperature at high temperature. Thus, at higher temperatures interpretations become less precise. The BFGG predicted by the PDM (39 °C/km) is less variable than that predicted by the LAM (36 °C/km). These BFGG fall within the intermediate range relative to the other four wells.

Lago Unit #1

Located in the north-central portion of the basin, the Lago Unit #1 shows moderate burial depths (7,000-16,000 ft) compared with the other wells. The average geothermal gradients of the models are 35 °C/km for the LAM and 40 °C/km for the PDM, however the BFGGs are far more consistent for the PDM. LG-3 (7,320′ MD) records a clumped isotope value that reflects surface/initial precipitation temperatures (29 °C). It is interpreted that this sample did not see high enough burial temperatures to induce significant reordering. As such, instead of being able to find a BFGG, I can only calculate a maximum geothermal gradient experienced by this sample (47 °C/ km for the LAM and 38 °C/km for the PDM). Above this gradient I would expect

reordering of Δ_{47} to occur and thereby no longer reflect the measured value. The assigned maximum burial temperature for this sample is then calculated using the average geothermal gradient of the well, based on the other samples in the well.

Texaco #1-29

The Texaco #1-29 is the westernmost well in this study and has the shallowest buried samples. Despite the shallow burial depths, all samples yield Δ_{47} values indicative of reordering. The LAM average gradient for the four sample depths is 42 °C/km, whereas the PDM averages a marginally warmer 44 °C/km. These averages are slightly warmer than the northern wells, but interestingly almost 40% warmer than the Rape, J. M. #1, which sits directly to the east on the other side of Reeves County (**Fig. 9**). The BFGGs between the sampled depths from the PDM are again more consistent than those from the LAM.

Weinacht #1

The Weinacht #1 well is situated in the southern Delaware Basin and contains samples with moderately shallow burial depths (7,000-13,000 ft). The LAM and PDM predict similar average geothermal gradients of 40 °C/km and 41 °C/km respectively. Again the PDM is more consistent between sample depths. Interestingly, sample W-1 (7,050′ MD) records an elevated T(Δ_{47}) of 100 °C, but the next deepest sample, W-2 (8,350′ MD) records a T(Δ_{47}) reflective of unaltered surface/initial precipitation conditions. I believe that neither the W-1 nor W-2 sample depths experienced high enough temperatures to induce reordering, and sample W-1 is recording a diagenetic/recrystallization temperature. Similar to LG-3, only a maximum geothermal gradient can be calculated for sample W-2, above which I would expect significant reordering that would no longer be reflective of the measured value.

Summary

For all five wells, the Linear Approximation Model (LAM) yields lower paleo-geothermal gradients (≈2.5 °C/km) than the Paired Diffusion Model (PDM) (**Table 4, Fig. 9**). The higher threshold temperature for the reordering reaction of pairs to singletons with the PDM means that higher temperatures are needed before significant reordering begins, and thereby higher paleo-geothermal gradients are calculated based on the same ending clumped isotope value. At significantly high temperatures (greater than approximately 180°C) the models agree very closely in the calculated paleo-geothermal gradients for calcite. This is because at these high temperatures, reordering of calcite takes place so quickly that both models predict clumped isotope values that are in equilibrium with the ambient burial temperatures. The largest divergence between the two models takes place in the intermediate temperatures (80°C-150°C) where the LAM predicts delayed but relatively rapid reordering, and the PDM predicts earlier but slower reordering (see **Fig. 2**).

The spatial trends of the average BFGGs support the conclusion that higher GORs in the western portions of the basin could be tied to higher geothermal gradients caused by thermal sources, such as Cenozoic intrusions and the Davis Mountains volcanics. Greater sampling density and spatial coverage will further clarify this conclusion.

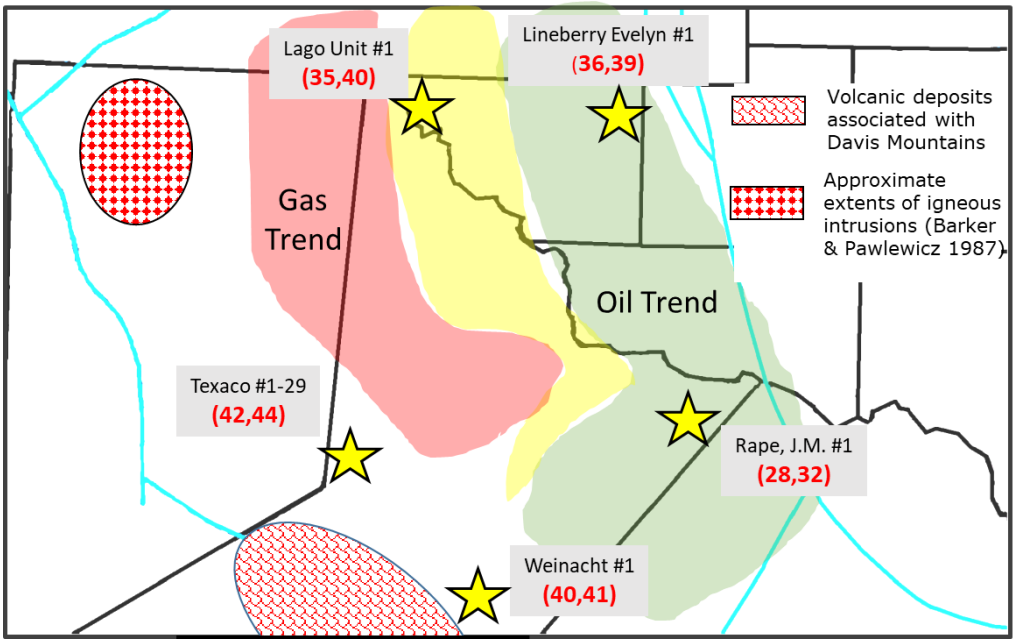

Figure 9- Spatial locations of wells, and calculated average geothermal gradients (LAM, PDM)

Comparison of Maximum Burial Temperatures: Vitrinite Reflectance vs. THRMs

Pawlewicz et al. (2005) compiled vitrinite reflectance (Ro) data for 74 boreholes across the Delaware Basin. The Lineberry Evelyn #1 and the Lago Unit #1 have Ro data from the 2005 study as well as clumped isotope data across similar depths. Barker & Pawlewicz (1986) determined the following time independent relationship between Ro (%) and maximum burial temperature (Tmax):

$$\ln(Ro) = 0.0078*(Tmax) - 1.2 \quad (8)$$

Using this relationship, the vitrinite reflectance Tmax can be plotted vs depth along with the modeled Tmax from the BFGG THRMs to compare the two independent methodologies.

Maximum burial temperatures of the vitrinite reflectance data and the modeled Tmax based on the best-fit THRMs are plotted in **Fig. 10 A-D**.

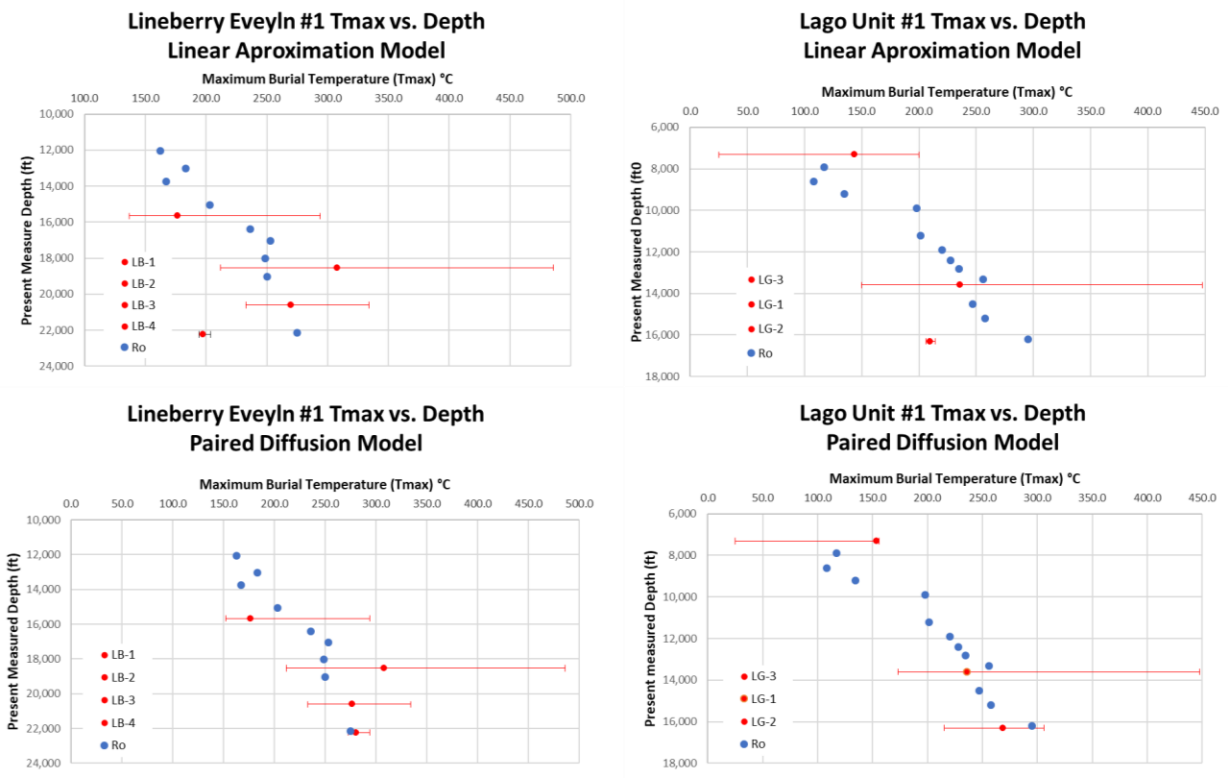

Figure 10- Maximum burial temperature vs depth based on vitrinite reflectance (blue) and modeled maximum burial temperatures based on the BFGG or the THRMs (red). A: Lineberry Evelyn #1 Linear Approximation Model. B: Lago Unit #1 Linear Approximation Model. C: Lineberry Evelyn #1 Paired Diffusion Model. D: Lago Unit #1 Paired Diffusion Model.

Lineberry Evelyn #1

The modeled maximum burial temperatures based on the THRMs fit the trend of the vitrinite reflectance data well within the propagated error of the measurements for samples LB-1, LB-2, and LB-3 for both models (**Fig. 10 A&C; s**ee **Appendix A** for error propagation method). However, only the PDM predicts maximum burial temperatures consistent with the vitrinite reflectance data for sample LB-4, which is a dolomite from the Ordovician Ellenberger

Formation. The maximum burial temperature for LB-2 is higher than the Ro trend in both of the models. This may be a reflection of the precision of the measured Δ_{47}. As previously mentioned, Δ_{47} is not linearly related to temperature and at higher temperature a small change in Δ_{47} can represent a larger change in temperature (see **Fig. 2**). Though the standard error of the measurement is not anomalously high compared with those of other samples, because this sample's Δ_{47} (0.335) is the lowest ("hottest"), its standard error represents a much greater temperature range. Overall there is good agreement between the vitrinite reflectance data and the modeled maximum burial temperatures based on the THRMs for the Lineberry Evelyn #1 well.

Lago Unit #1

Maximum burial temperatures based on vitrinite reflectance and best-fit THRM are plotted in **Fig. 10B&D**. Similar to Lineberry Evelyn #1, the modeled maximum burial temperatures based on the best-fit THRMs fit well with the Ro Tmax. The Linear Approximation Model predicts the maximum burial temeratures of the calcite samples well, but again underpredicts the temperatures for the deepest buried dolomite of the Ellenburger formation (sample LG-2). The Paired Diffusion Model again better predicts the deeper buried dolomite, within the trend of the vitrinite reflectance data. This suggests that the PDM does a better job at predicting intermediate temperature reordering, within the context of uncertain dolomite reordering kinetics. Future empirical determination of the reordering kinetics of dolomite will serve as a means to test and confirm this observation.

Burial History Sensitivity Tests

The time-temperature history of the samples is by far the most important control on their reordering pathways and by extension the measured final apparent clumped isotope temperatures. To test the sensitivity of the results based on the burial curves provided by the Chevron CoRE, I adjusted the burial curves for the Lineberry Evelyn #1 and the Lago Unit #1 by adding and subtracting one kilometer of burial (e.g. **Fig. 11**).

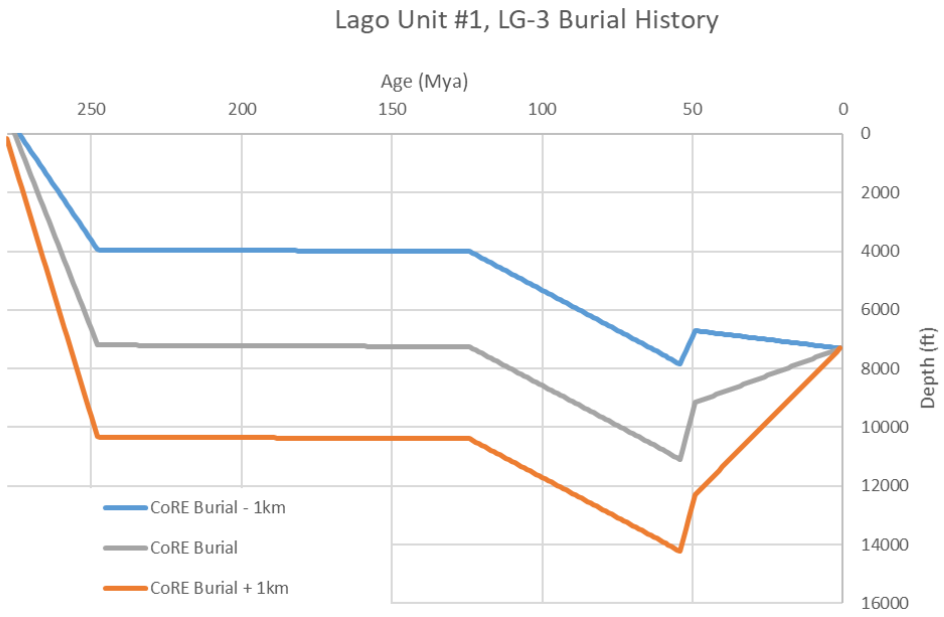

Figure 11- Adjusted shallow and deep burial curves for sample LG-3 alongside provided curve from Chevrom CoRE.

I then used the new burial curves to find the best-fit geothermal gradients for each depth using both models. The resultant BFGGs were used to calculate the corresponding modeled maximum burial temperatures with the new burial curves (**Table 5).**

*Table 5- Results of best-fit geothermal gradients based on the adjusted shallow and deep burial curves. S indicates 1km less burial, D indicates 1 km greater burial. *Indicates a recrystallization temperature of 75°C. **Indicates ± the 95% confidence interval of the measurement. S indicates 1km less burial, D indicates 1 km greater burial.*

ID	depth (ft)	max burial depth (modeled) ft	Δ47 CDES **	Clumped T (°C)	Modeled Max Burial Temp LAM (°C)	Modeled Max Burial Temp PDM (°C)	BFGG LAM (°C/km)	BFGG PDM (°C/km)
LB-1	15,660	16,057	0.421 ± 0.079	173	177	176	31	31
LB-2	18,530	18,930	0.335 ± 0.055	379	302	302	49	49
LB-3	20,300	20,600	0.351 ± 0.025	272	270	276	39	40*
LB-4	22,230	22,650	0.446 ± 0.043	149	198	281	25	37*
LB-1 S	15,660	18,320	0.421 ± 0.079	173	173	177	31	32
LB-2 S	18,530	21,200	0.335 ± 0.055	305	305	305	49	49
LB-3 S	20,300	23,000	0.351 ± 0.025	272	272	310	39	46*
LB-4 S	22,230	22,230	0.446 ± 0.043	149	204	282	27	38*
LB-1 D	15,660	15,660	0.421 ± 0.079	173	198	198	31	31
LB-2 D	18,530	18,530	0.335 ± 0.055	305	341	341	49	49
LB-3 D	20,300	20,300	0.351 ± 0.025	272	298	305	39	40*
LB-4 D	22,230	24,900	0.446 ± 0.043	149	204	306	23	37*
LG-3	7,320	11,100	0.674 ± 0.049	29	140	153	47	38*
LG-1	13,600	17,300	0.400 ± 0.088	197	236	236	40	40
LG-2	16,300	20,000	0.477 ± 0.057	124	208	269	30	40*
LG-3 S	7,320	7,800	0.674 ± 0.049	29	185	180	67	70*
LG-1 S	13,600	14,100	0.400 ± 0.088	197	201	201	41	41
LG-2 S	16,300	16,800	0.477 ± 0.057	124	207	230	36	40*
LG-3 D	7,320	14,300	0.674 ± 0.049	29	185	189	37	38*
LG-1 D	13,600	20,500	0.400 ± 0.088	197	281	275	41	40
LG-2 D	16,300	23,200	0.477 ± 0.057	124	208	280	26	36*

The modeled maximum burial temperatures were then plotted alongside the maximum burial temperatures of the vitrinite reflectance for the Lago Unit #1 and the Lineberry Evelyn #1 wells (**Fig.12)**. In all cases, the CoRE burial histories show less variability in the BFGGs within a well, and better fits to the Tmax values calculated from the vitrinite reflectance data. It is especially apparent in **Figure 12C** that the deep burial curve overestimates the vitrinite data, and the shallow burial curve underestimates it. Again the PDM results show the better fit with the vitrinite reflectance data and less variabilty in the calculated paleo-geothermal gradients than do the LAM results. The results using the Chevron CoRE's burial curves are more predictive of consistent paleo-geothermal gradients within a well bore, and more consistently match the calculated maximum burial temperatures of vitrinite reflectance data than the modified shallow and deep burial curves.

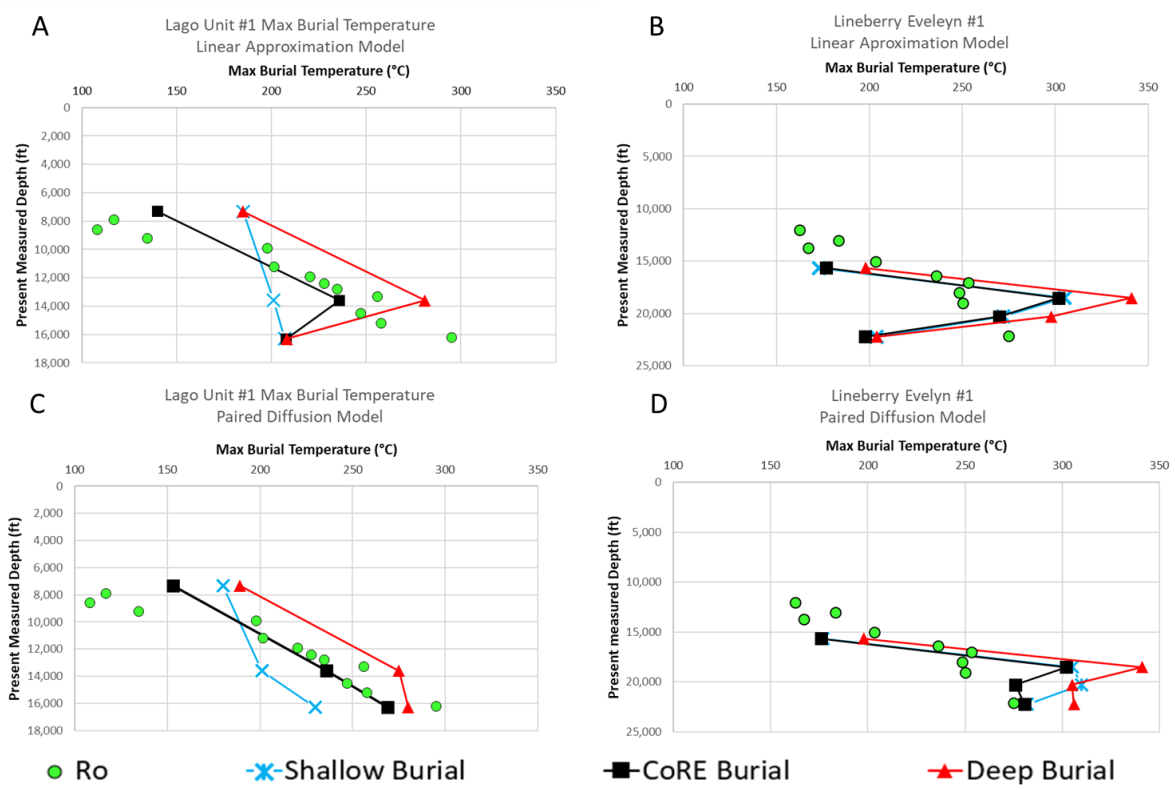

Figure 12- Maximum burial temperature based on vitrinite reflectance and THRMs. Shallow burial curve represents approximately one km less burial than CoRE curve. Deep burial represents approximately one km greater burial than CoRE curve.

CONCLUSIONS

Apparent clumped isotope termperatures of carbonate cuttings taken from five wells spread across the Delaware Basin vary from 26 °C to 305 °C and reflect a combination of initial precipitation temperatures and solid-state reordering during burial heating. The apparent clumped isotope temperatures were used in conjunction with burial history curves to calculate the best fit geothermal gradient (BFGG) for each well, using two different Thermal History Reordering Models (THRMs). The spatial results of the BFGGs support the conclusion that the wells in the shallower, southwestern portions of the basin experienced approximately 40% higher temperature gradients throughout their history than did the wells in the southeastern portions (~44 °C/km vs 32 °C/km). This trend supports the hypothesis that higher GORs in the western portion of the Delaware Basin are tied to higher paleo-geothermal gradients, which could be associated with identified thermal sources such as Cenozoic igneous intrusions as wells as the Davis Mountains volcanics.

The BFGGs calculated from the THRMs curves provided by the Chevron Center of Research Excellence (CoRE) fit well with the maximum burial temperatures from vitrinite reflectance data of Barker & Pawlewicz (2005). Furthermore, the burial curves provided by the Chevron CoRE better match the maximum burial temperature of the vitrinite reflectance data than do the modified shallow and deep burial curves (±1 km) created for the Lineberry Eveleyn #1 and the Lago Unit #1 wells. The Paired Diffusion Model (PDM) matches the vitrinite reflectance data better than the Linear Approximation Model (LAM). The PDM predicts more consistent BFGGs between the sample depths within a wellbore, and it also models dolomite reordering more effectively. Based on this study's data set, the PDM proves to be the better model for this application.

Carbonate clumped isotope values are controlled by the same processes that control the industry standard method of assessing thermal maturity, vitrinite reflectance. Both techniques have their strengths and limitations. However, this study demonstrates that carbonate clumped isotopes not only respond to the same thermal variables as vitrinite reflectance, but that the two separate methodologies can yield similar results. Carbonate clumped isotopes can be a complementary technique to vitrinite reflectance. Future quantification of the reordering kinetics of dolomite, and future improvements in instrumentation will further strengthen the use of clumped isotopes as a tool for assessing thermal maturity.

REFERENCES

Barker, C. E., & Pawlewicz, M. J. (1987) The effects of igneous intrusions and higher heat flow on the thermal maturity of Leonardian and younger rocks, western Delaware Basin, Texas. In: *Glass Mountain: SEPM Guidebook*, 67-83.

Barker, C. E., & Pawlewicz, M. J. (1986) The correlation of vitrinite reflectance with maximum temperature in humic organic matter. In: *Paleogeothermics* (pp. 79-93). Springer, Berlin, Heidelberg.

Bernasconi, S. M., Hu, B., Wacker, U., Fiebig, J., Breitenbach, S. F. M., & Rutz, T. (2013) Background effects on Faraday collectors in gas-source mass spectrometry and implications for clumped isotope measurements. *Rapid Communications in Mass Spectrometry*, 27(5), 603–612.

Bonifacie, M., Calmels, D., Eiler, J. M., Horita, J., Chaduteau, C., Vasconcelos, C., ... & Bourrand, J. J. (2017) Calibration of the dolomite clumped isotope thermometer from 25 to 350 C, and implications for a universal calibration for all (Ca, Mg, Fe) CO 3 carbonates. *Geochimica et Cosmochimica Acta*, *200*, 255-279.

Came, R. E., Eiler, J. M., Veizer, J., Azmy, K., Brand, U., & Weidman, C. R. (2007) Coupling of surface temperatures and atmospheric CO_2 concentrations during the Palaeozoic era. *Nature*, *449*(7159), 198.

Defliese, W. F., Hren, M. T., & Lohmann, K. C. (2015) Compositional and temperature effects of phosphoric acid fractionation on Δ47 analysis and implications for discrepant calibrations. *Chemical Geology, 396*, 51-60.

Dennis, K. J., & Schrag, D. P. (2010) Clumped isotope thermometry of carbonatites as an indicator of diagenetic alteration. *Geochimica et Cosmochimica Acta*, 74(14), 4110-4122.

Eiler, J.M., (2007) “Clumped-isotope” geochemistry-the study of naturally-occurring, multiply-substitute isotopologues. *Earth and Planetary Science Letters*, 262, 309-327.

Eiler, J. M., & Schauble, E. (2004) ^{18}O ^{13}C ^{16}O in Earth’s atmosphere. *Geochimica et Cosmochimica Acta*, 68(23), 4767-4777.

Finnegan, S., Bergmann, K., Eiler, J. M., Jones, D. S., Fike, D. A., Eisenman, I., ... & Fischer, W. W. (2011) The magnitude and duration of Late Ordovician–Early Silurian glaciation. *Science*, 331(6019), 903-906.

Enos, P., Aracen, R. R., Minero, C. J., & Yurewicz, D. (1997) *Sedimentation and Diagenesis of Middle Cretaceous Platform Margins, East-Central Mexico*.

Epstein, S., Buchsbaum, R., Lowenstam, H.A., Urey, H.C., (1953) Revised carbonate-water isotopic temperature scale. *Geological Society of America Bulletin*, 64, 11, 1315-1326.

Gawloski, T. F. (1987) Nature, distribution, and petroleum potential of Bone Spring detrital sediments along the Northwest Shelf of the Delaware Basin. In: *Cromwell and Mazzullo, eds*, 87-27.

Ghosh, P., Adkins, J., Affek, H., Balta, B., Guo, W.F., Schauble, E.A., Schrag, D., Eiler, J.M., (2006) ^{13}C- ^{18}O bonds in carbonate minerals: a new kind of paleothermometer. *Geochimica et Cosmochimica Acta* 70 (6), 1439-1456.

He, B., Olack, G. A., & Colman, A. S. (2012) Pressure baseline correction and high-precision CO_2 clumped-isotope (Δ_{47}) measurements in bellows and micro-volume modes. *Rapid Communications in Mass Spectrometry*, 26(24), 2837–2853

Henkes, G.A., Passey, B.H., Grossman, E.L., Yancey, T.E., Shenton, B., (2013) Empirical and experimental evidence of 13C- 18O bond reordering in Paleozoic brachiopod shells. *3 rd International Workshop on Clumped Isotopes*. Harvard University, Cambridge MA.

Henkes, G. A., Passey, B. H., Grossman, E. L., Shenton, B. J., Pérez-Huerta, A., & Yancey, T. E. (2014). Temperature limits for preservation of primary calcite clumped isotope paleotemperatures. *Geochimica et cosmochimica acta*, *139*, 362-382.

Hills, J. M. (1984) Sedimentation, tectonism, and hydrocarbon generation in Delaware basin, west Texas and southeastern New Mexico. *AAPG Bulletin*, *68*(3), 250-267.

Huntington, K. W., Wernicke, B. P., & Eiler, J. M. (2010) Influence of climate change and uplift on Colorado Plateau paleotemperatures from carbonate clumped isotope thermometry. *Tectonics*, *29*(3).

Huntington, K. W., Budd, D. A., Wernicke, B. P., & Eiler, J. M. (2011) Use of clumped-isotope thermometry to constrain the crystallization temperature of diagenetic calcite. *Journal of Sedimentary Research*, *81*(9), 656-669.

John, C. M. (2015) Burial estimates constrained by clumped isotope thermometry: example of the Lower Cretaceous Qishn Formation (Haushi-Huqf High, Oman). *Geological Society, London, Special Publications*, *435*, SP435-5.

Kim, S. T., & O'Neil, J. R. (1997) Equilibrium and nonequilibrium oxygen isotope effects in synthetic carbonates. *Geochimica et Cosmochimica Acta*, *61*(16), 3461-3475.

Kluth, C. F., & Coney, P. J. (1981) Plate tectonics of the ancestral Rocky Mountains. *Geology*, *9*(1), 10-15.

Kupecz, J. A., Kerans, C., & Land, L. S. (1988) Deep-burial dolomitization in the Ordovician Ellenburger Group Carbonates, West Texas and Southeastern New Mexico: DISCUSSION. *Journal of Sedimentary Research*, *58*(5).

Kupecz, J. A., & Land, L. S. (1991) Late-stage dolomitization of the lower Ordovician Ellenburger Group, west Texas. *Journal of Sedimentary Research*, *61*(4).

Lawson, M., Shenton, B. J., Stolper, D. A., Eiler, J. M., Rasbury, E. T., Becker, T. P., ... & Gray, G. G. (2017) Deciphering the diagenetic history of the El Abra Formation of eastern Mexico using reordered clumped isotope temperatures and U-Pb dating. *GSA Bulletin*.

Lee, Y. I., & Friedman, G. M. (1987) Deep-burial dolomitization in the Ordovician Ellenburger Group carbonates, west Texas and southeastern New Mexico. *Journal of Sedimentary Research*, *57*(3).

Lloyd, Max Kaufmann (2018) *Clumped and Intramolecular Isotopic Perspectives on the Behavior of Organic and Inorganic Carbon in the Shallow Crust and Deep Biosphere. Dissertation (Ph.D.),* California Institute of Technology.

Lloyd, M. K., & Eiler, J. M. (2014) Laboratory and natural constraints on the temperature limit for preservation of the dolomite clumped isotope thermometer. In: *AGU Fall Meeting Abstracts*.

MacDonald, J. M., John, C. M., & Girard, J. P. (2017) Testing clumped isotopes as a reservoir characterization tool: a comparison with fluid inclusions in a dolomitized sedimentary carbonate reservoir buried to 2–4 km. *Geological Society, London, Special Publications*, *468*, SP468-7.

Meckler, A. N., Ziegler, M., Millán, M. I., Breitenbach, S. F., & Bernasconi, S. M. (2014) Long-term performance of the Kiel carbonate device with a new correction scheme for clumped isotope measurements. *Rapid Communications in Mass Spectrometry*, *28*(15), 1705-1715.

Passey, B.H., Henkes, G.A., (2012) Carbonate clumped isotope bond reordering and geospeedometry. *Earth and Planetary Science Letters*, 352-352, 223-236.

Pawlewicz, M. J., Barker, C. E., & McDonald, S. (2005) Vitrinite reflectance data for the Permian Basin, west Texas and southeast New Mexico. *US Department of the Interior, US Geological Survey*.

R Core Team (2018). R: A language and environment for statistical computing. R Foundation for Statistical Computing, Vienna, Austria. URL https://www.R-project.org/.

Reed, T. A., & Strickler, D. L. (1990, May) Structural geology and petroleum exploration of the Marathon thrust belt, west Texas. In: *Marathon thrust belt: structure, stratigraphy, and hydrocarbon potential: West Texas Geological Society and PBS-SEPM field seminar* (pp. 39-64).

Ross, S. M. (2003) Peirce's criterion for the elimination of suspect experimental data. *Journal of engineering technology*, *20*(2), 38.

Ruppel, S., Jones, R., Breton, C., & Kane, J., (2005) Preparation of maps depicting geothermal gradient and Precambrian structure in the Permian Basin. *Contract report to the USGS*, May, 2005.

Schauble, E.A., Ghosh, P., Eiler, J.M., (2006) Preferential formation of 13C-18O bonds in carbonate minerals, estimated using first-principles lattice dynamics. *Geochimica et Cosmochimica Acta* 70, 2510-2529.

Shenton, B. J., Grossman, E. L., Passey, B. H., Henkes, G. A., Becker, T. P., Laya, J. C., ... &Lawson, M. (2015) Clumped isotope thermometry in deeply buried sedimentary carbonates: The effects of bond reordering and recrystallization. *Geological Society of America Bulletin*, 127(7-8), 1036-1051.

Sinclair, T. D. (2007) The generation and continued existence of overpressure in the Delaware Basin, Texas. *Dissertation (Ph.D.)*, Durham University.

Smith, G. W. (1979). Ellenburger Group, Delaware Basin, West Texas. *AAPG Bulletin*, *63*(3), 530-530.

Soetaert, K. E. R., Petzoldt, T., & Setzer, R. W. (2010) Solving differential equations in R: package deSolve. *Journal of Statistical Software*, *33*.

Stolper, D. A., & Eiler, J. M. (2015) The kinetics of solid-state isotope-exchange reactions for clumped isotopes: A study of inorganic calcites and apatites from natural and experimental samples. *American Journal of Science*, *315*(5), 363-411.

Tucker, M. E., & Wright, V. P. (1990) Dolomites and dolomitization models. *Carbonate sedimentology*, 365-400.

Urey, H. C. (1947) The thermodynamic properties of isotopic substances. *Journal of the Chemical Society (Resumed)*, 562-581.

APPENDIX A

Workflow of THRM modeling and data fitting:

Steps:

1) Determine mean Δ_{47} value for sample
2) Calculate 95% confidence interval of Δ_{47} based on 1.96*SE of measurement.
3) Input burial curve (depth vs time) into Excel; multiply by linear geothermal gradient to create time-temperature history.
4) Model time-temperature history using the Linear Approximation Method and the Paired Diffusion Method, varying the geothermal gradient in 0.5 °C/km increments until the modeled Δ_{47} best matches the measured mean value (lowest absolute value of modeled T – measured T). This geothermal gradient is the best-fit geothermal gradient (BFGG). For this and every following step, there will be two sets of data, one for each model.
5) Using the time-temperature history of the BFGG, record the maximum burial temperature.
6) Repeat Step 4, but instead of varying the model to match the mean value, match the upper (cooler) bound of the 95% confidence interval of Δ_{47}. This is the coolest geothermal gradient that fits the Δ_{47} measurment. Likewise repeat Step 4, matching for the lower (warmer) bound of the 95% confidence interval of Δ_{47}. This is the warmest geothermal gradient that fits the Δ_{47} measurment.
7) Using the bounding geothermal gradients from Step 6, record the maximum burial temperature of their respective time-temperature histories. These represent the error bars on the modeled maximum burial temperature value.

8) To compare modeled maximum burial tempearture vs vitrinite maximum burial temperature, plot both vs present measured depth.
9) To constrain the burial curve, create a shallow and deep case that represent ± one km of burial. Now repeat Steps 4 & 5 using the new burial curves. To find the new BFGGs and the maximum burial temperatures.
10) Plot the modeled maximum burial tempertaures for the original, shallow, and deep cases next to the vitrinite reflectance data, and observe which case fits the data best.

APPENDIX B

Screening of samples Using Scanning Electron Micoroscopy (SEM):

A scanning electron microscope, used courtesy of Dr. Juan Carlos Laya at Texas A&M University, was the primary means of determining the lithology of samples and screening for potential contaminants. The settings used were: 15 kV Accelerating voltage, low vacuum, map mode. Shown below are a small but representative selection of the images taken as part of the screening process, captioned with their significance to the project:

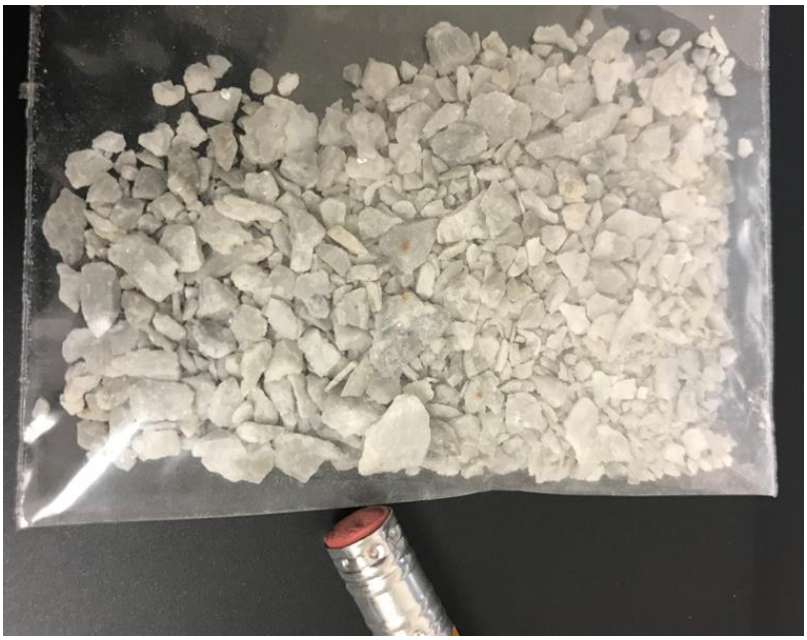

Figure A- 1 Cuttings collected from BEG before being embedded in epoxy. Pencil eraser for size reference.

Figure A- 2 Lineberry Evelyn #1 well, 20,300' MD, Ellenberger Formation. The selected cutting was one of many seated in epoxy, a piece of which shows as the large black body in the center of the image. The crosshairs in the top left quadrant indicate a spot elemental analysis, the results of which are shown in The highly fractured nature of the surface is due to sanding of the sample billet to abrade the epoxy in which the grains are embedded.

Table A-1 - Elemental analysis of crosshair point in Figure 13. Equal proportions of Ca and Mg along with visual nature of the cleavage and crystal habit in Figure 13 confirm that this sample is dolomite. Identifying the mineralogy of the samples is key, as the reordering parameters between calcite and dolomite are different.

Element Number	Element Symbol	Element Name	Atomic Concentration %	Error
20	Ca	Calcium	8.7	0.1
8	O	Oxygen	54.8	0.2
12	Mg	Magnesium	8.4	0.0
6	C	Carbon	28.0	0.5

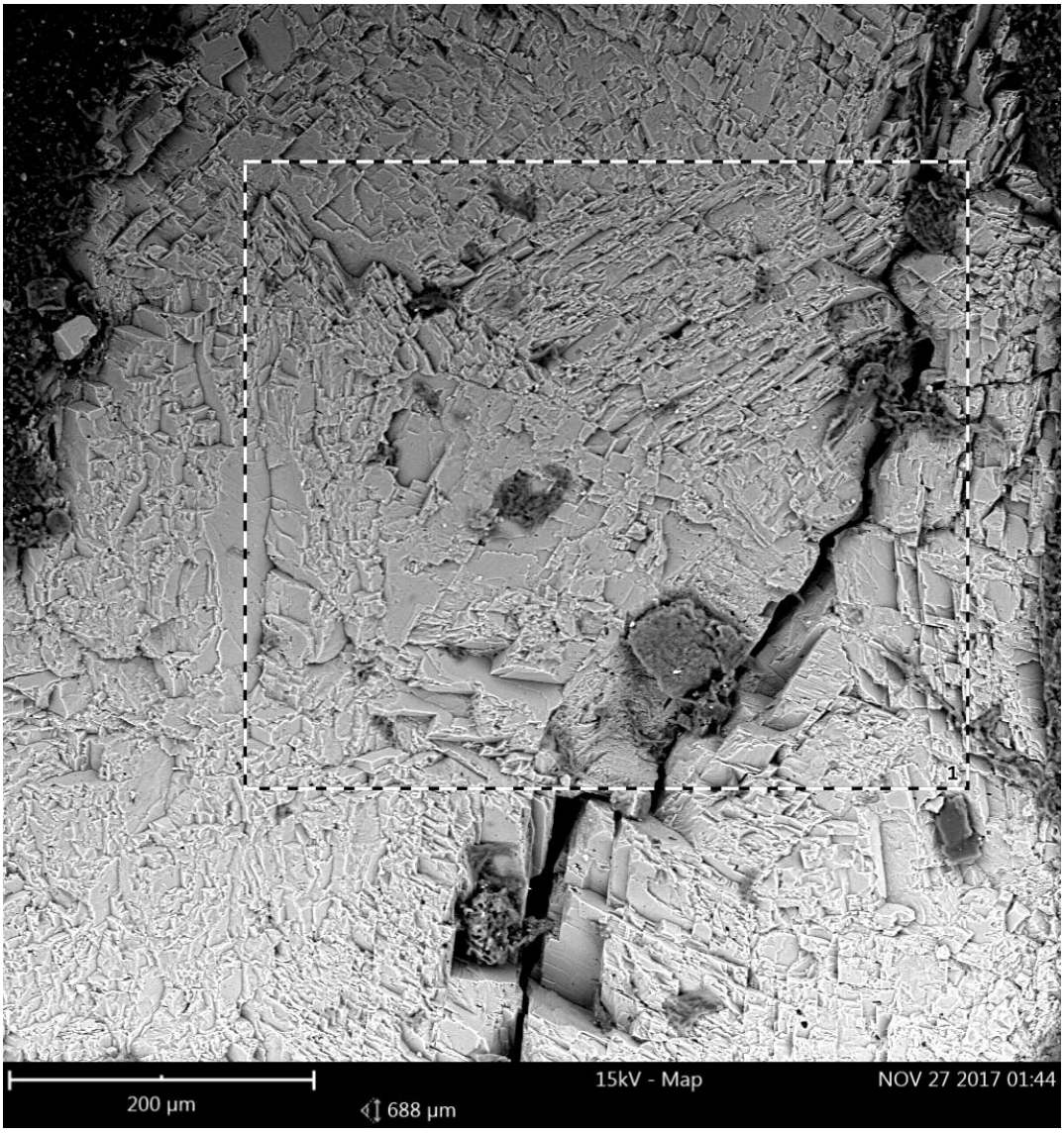

Figure A- 3 SEM Image of Lineberry Evelyn #1, 22,230' (LB-4). Large dolomite crystals are present, with the cleavage patterns showing different crystal growth directions.

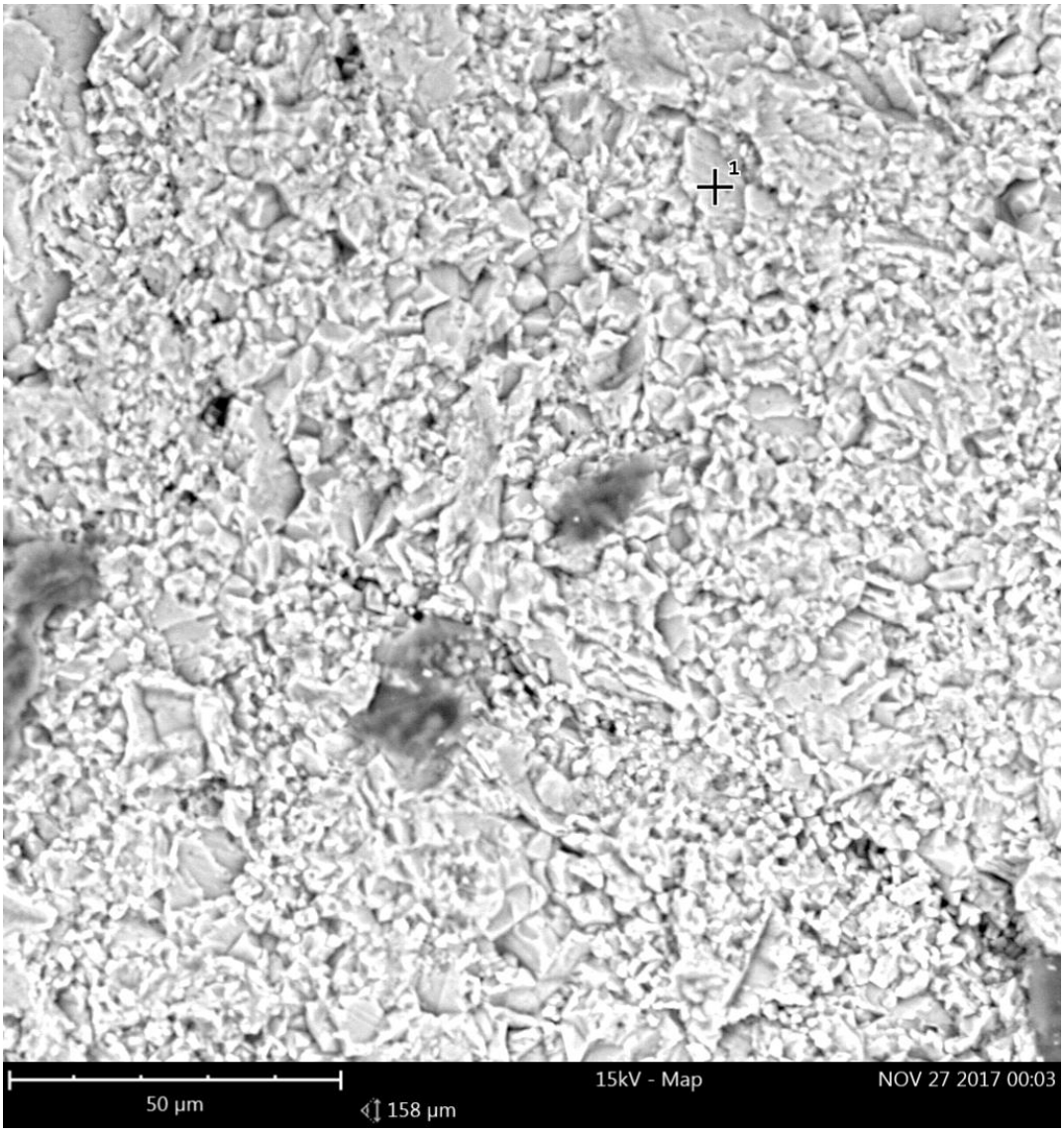

Figure A- 4 SEM Image of a finely grained carbonate cutting from the Lago Unit #1 13,600' MD (LG-1)

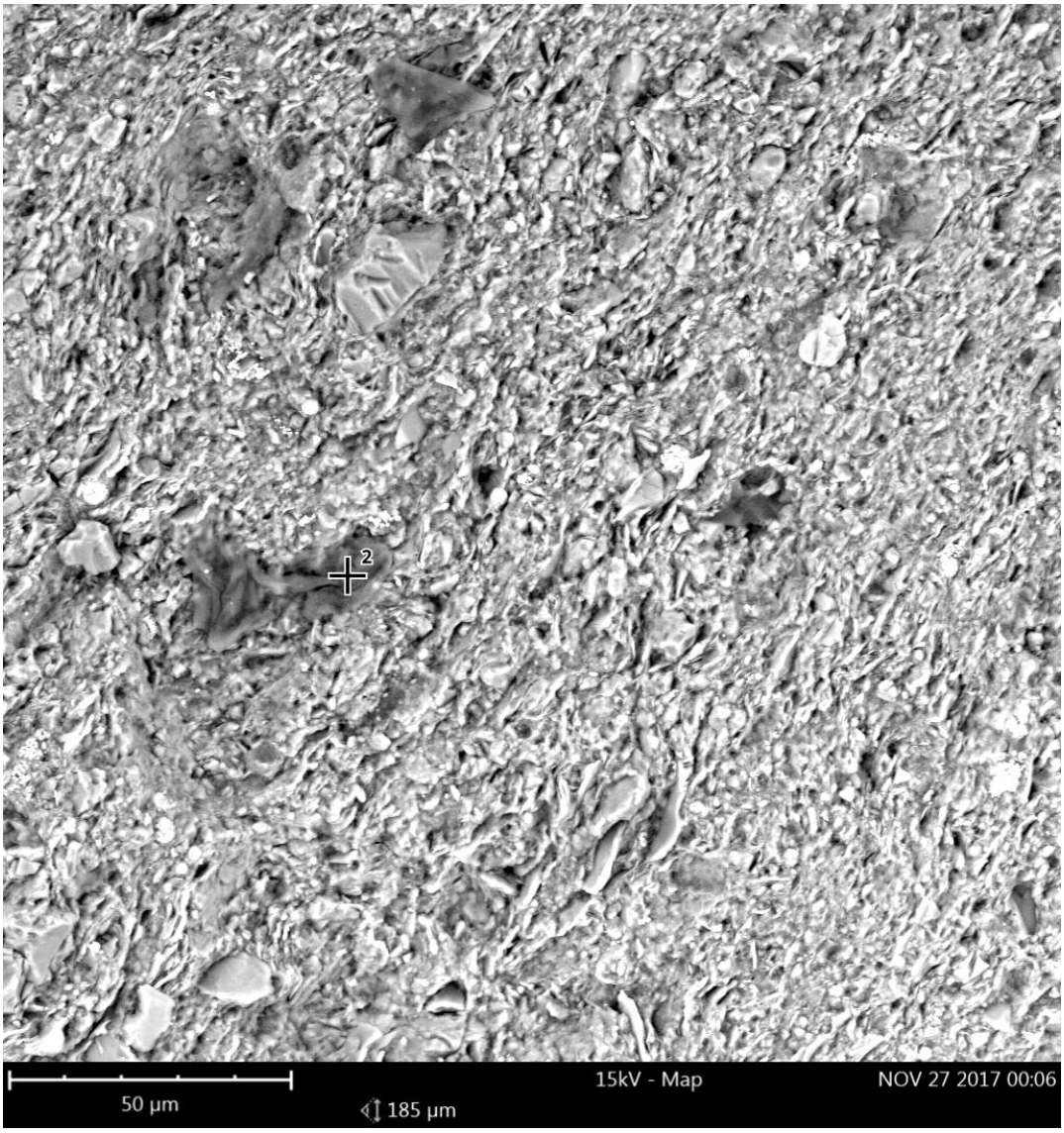

Figure A- 5 SEM Image of a cutting from the Lago Unit #1, 13,600' MD (LG-1). This cutting is from the same depth as the cutting in Figure 16. However, it is clear that this cutting's mineralogy is not carbonate. This cutting is from a shale bed and shows the variability of lithologies within a sample depth, and the need for manual separation of carbonate cuttings.

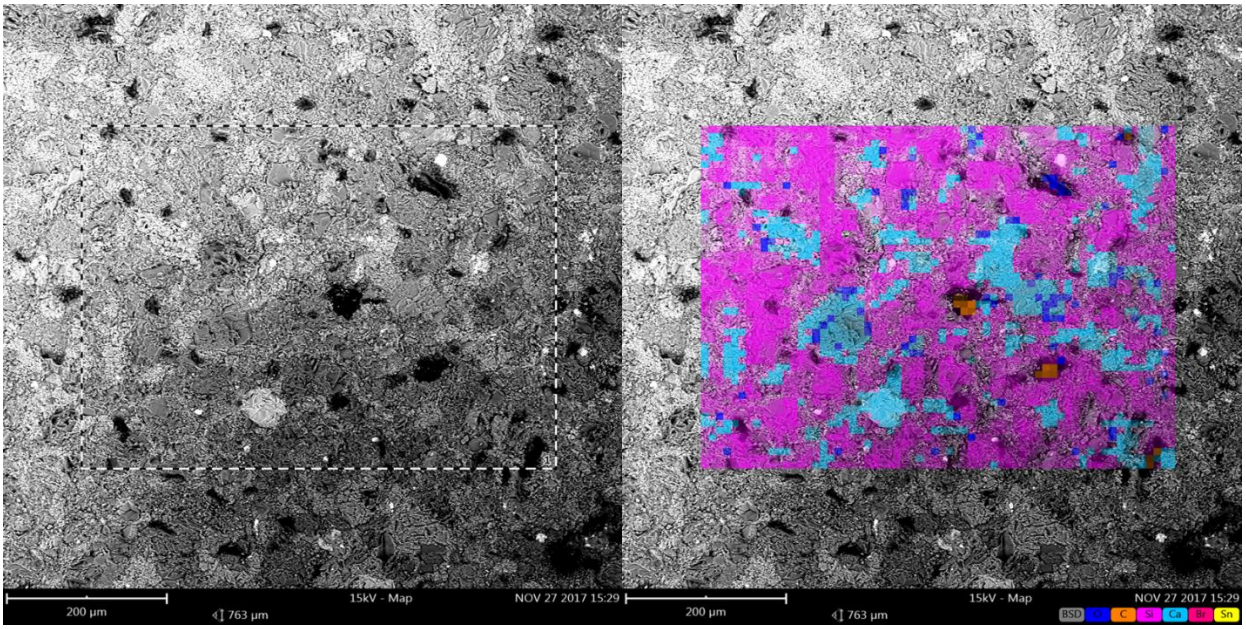

Figure A- 6 Lineberry Evelyn #1 8900' MD. SEM image and corresponding elemental mapping of a cutout. The color of the map corresponds to the dominant element present (key in bottom right hand corner). The purple color reflects silicon and is interpreted to be a silicate mineral such as a clay. The light blue corresponds to calcium and is interpreted to be a calcite. As seen from the pattern, there are small calcite veins, possible secondary precipitation between larger zones of clay minerals. This sample was deemed to have too low of a carbonate content for analysis.

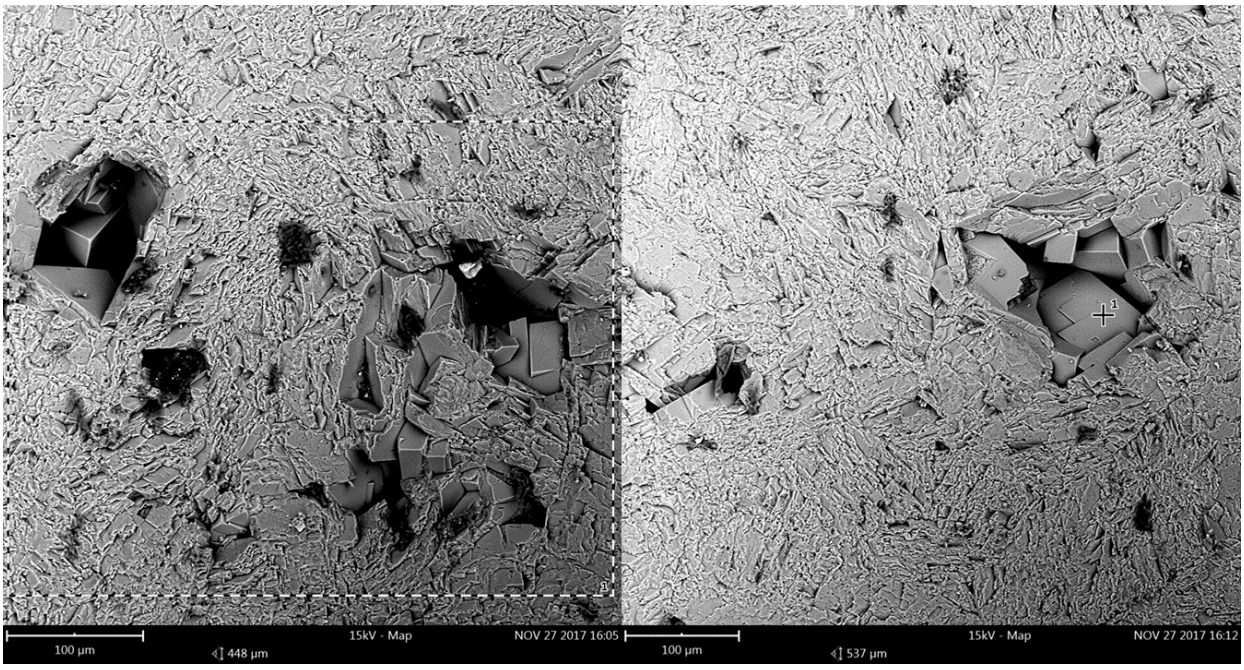

Figure A- 7 SEM images of cuttings from the Rape, J. M. #1 well, 18,350' MD (JMR-3). Porosity voids within the cuttings reveal large dolomite crystals.

APPENDIX C

Reordering Pathways for all Samples: LAM= Linear Approximation Model, PDM= Paired Diffusion Model.

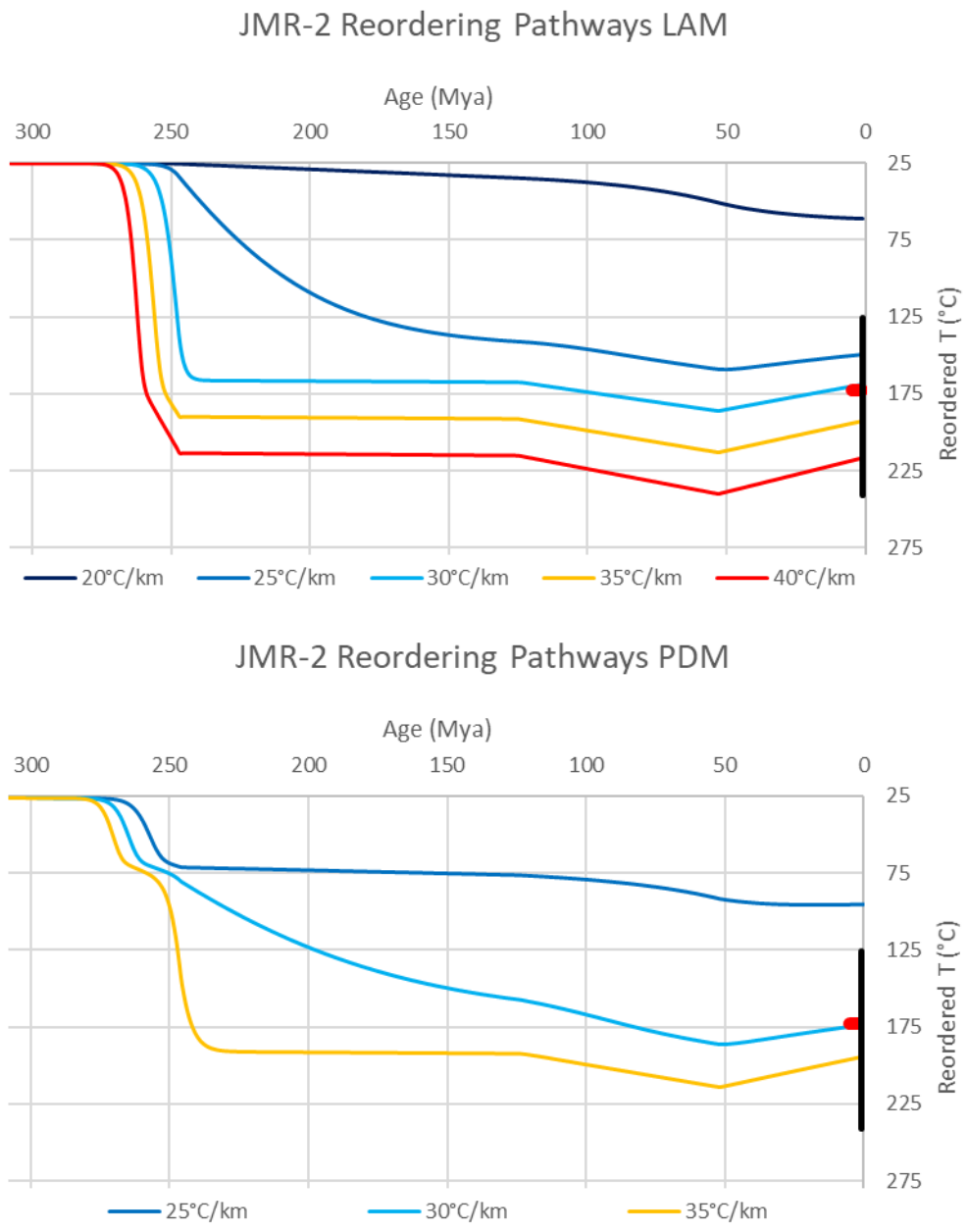

Figure A- 8

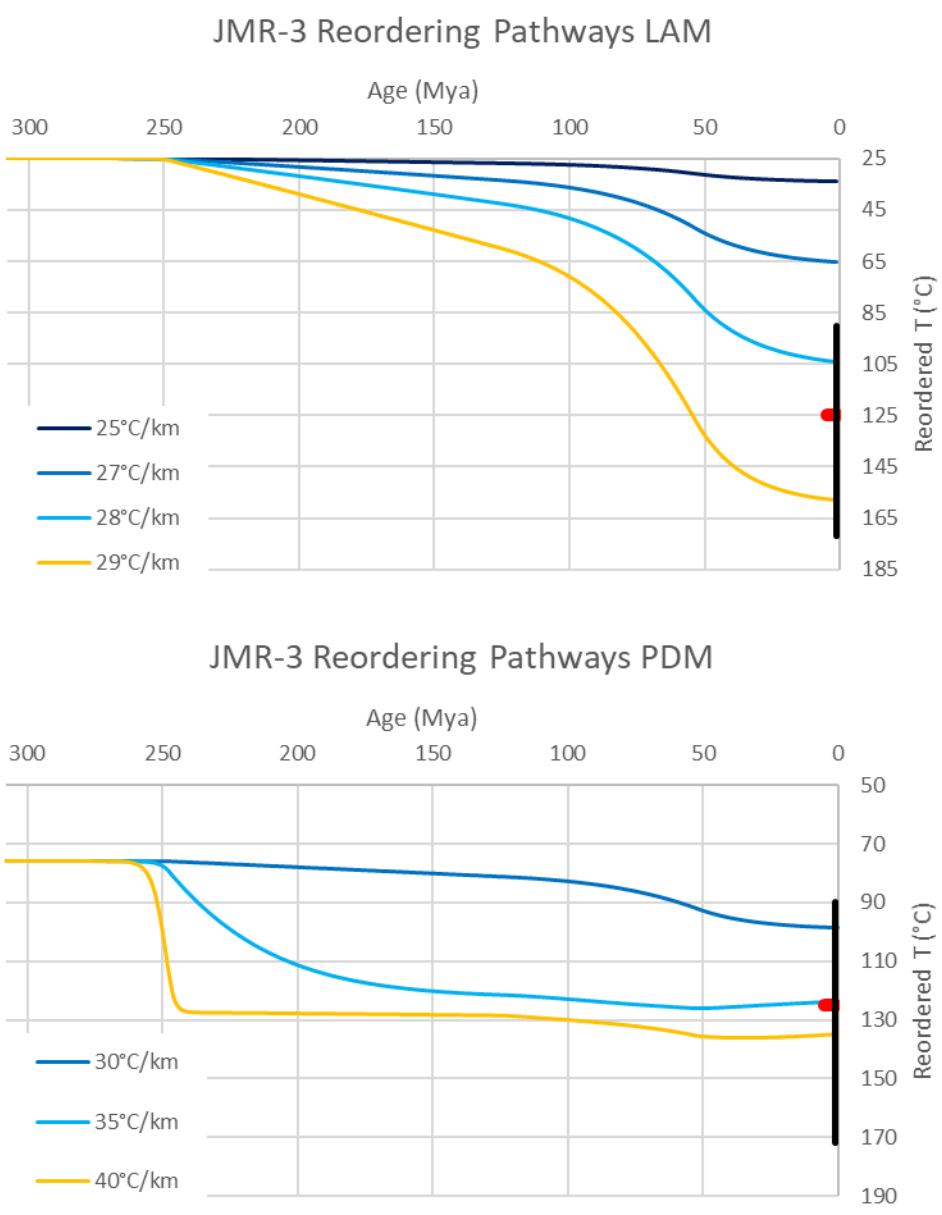
JMR-3 Reordering Pathways LAM
Age (Mya)
300
250
200
150
100
50
0
25
45
65
85
105
125
145
165
185
Reordered T (°C)
25°C/km
27°C/km
28°C/km
29°C/km
JMR-3 Reordering Pathways PDM
Age (Mya)
300
250
200
150
100
50
0
50
70
90
110
130
150
170
190
Reordered T (°C)
30°C/km
35°C/km
40°C/km

Figure A- 9

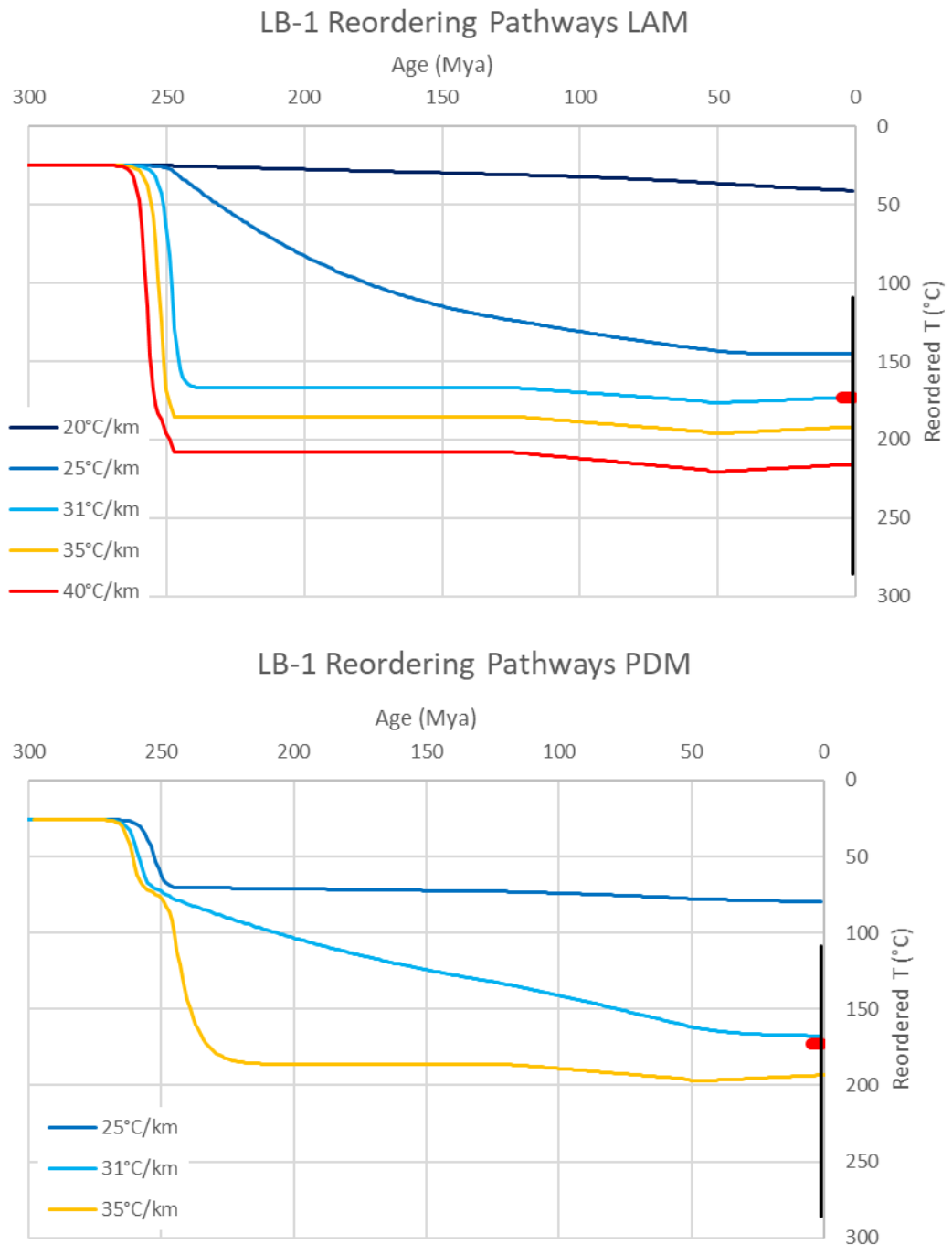
LB-1 Reordering Pathways LAM
Age (Mya)
300
250
200
150
100
50
0
0
50
100
150
200
250
300
Reordered T (°C)
20°C/km
25°C/km
31°C/km
35°C/km
40°C/km
LB-1 Reordering Pathways PDM
Age (Mya)
300
250
200
150
100
50
0
0
50
100
150
200
250
300
Reordered T (°C)
25°C/km
31°C/km
35°C/km

Figure A- 10

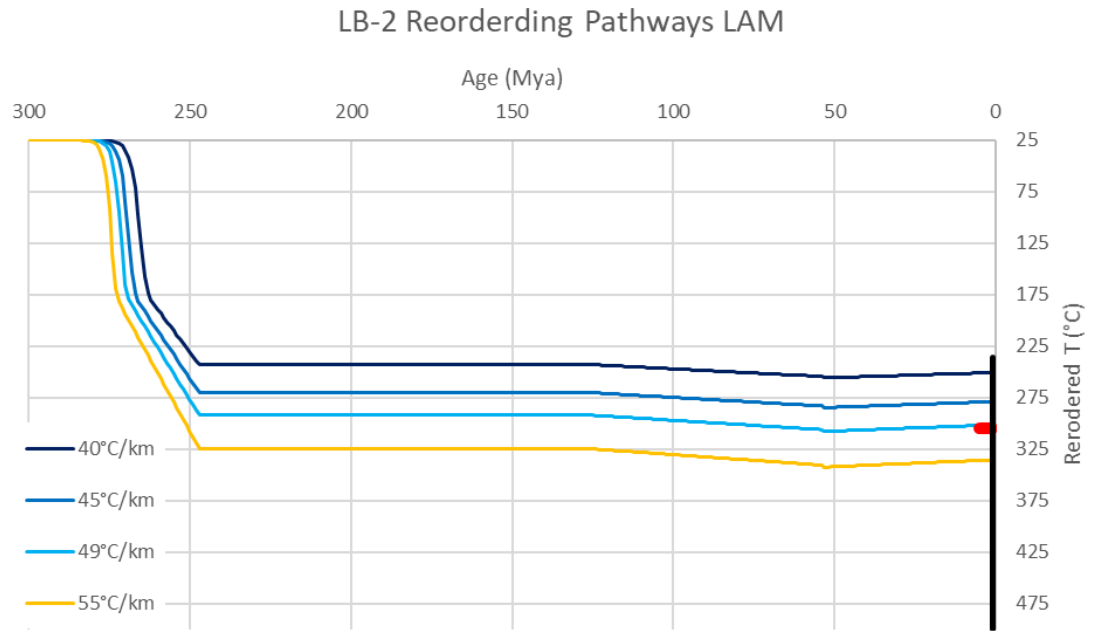
LB-2 Reorderding Pathways LAM
Age (Mya)
300
250
200
150
100
50
0
25
75
125
175
225
275
325
375
425
475
Rerodered T (°C)
40°C/km
45°C/km
49°C/km
55°C/km

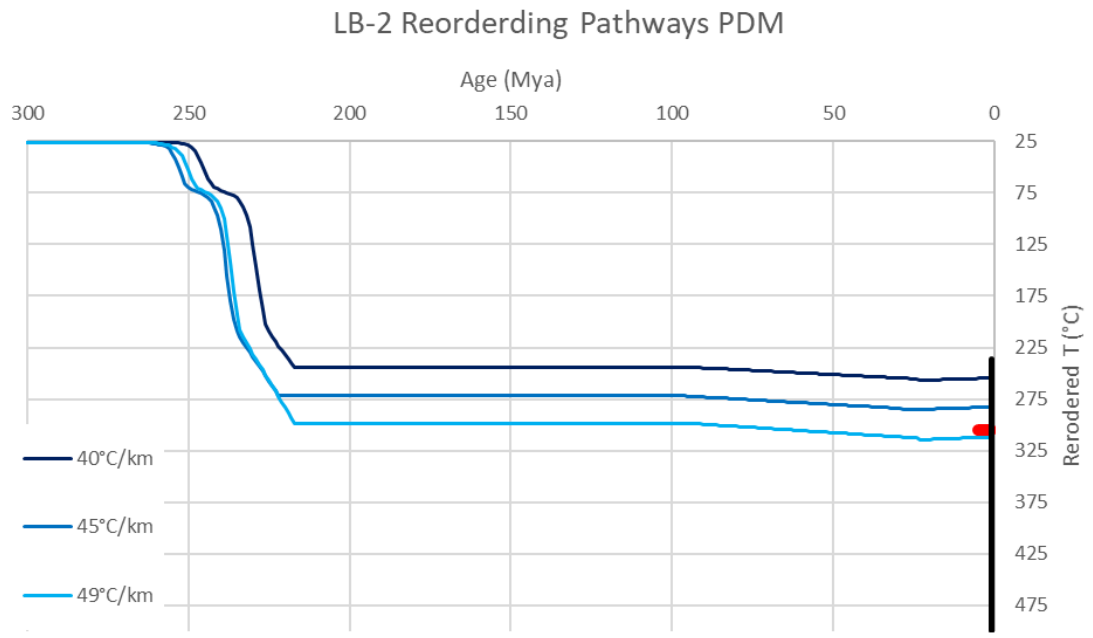
LB-2 Reorderding Pathways PDM
Age (Mya)
300
250
200
150
100
50
0
25
75
125
175
225
275
325
375
425
475
Rerodered T (°C)
40°C/km
45°C/km
49°C/km

Figure A- 11

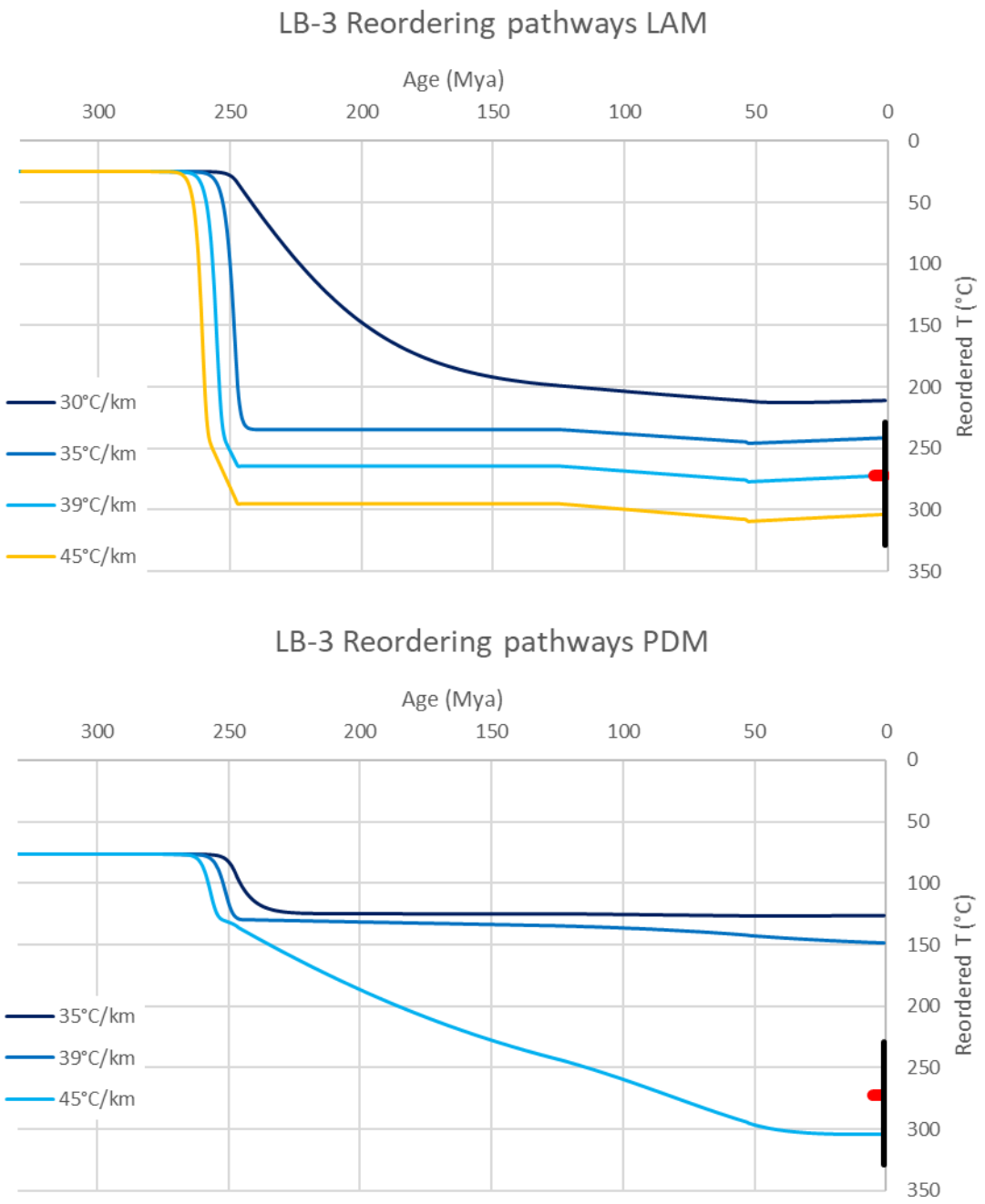
LB-3 Reordering pathways LAM
Age (Mya)
300
250
200
150
100
50
0
0
50
100
150
200
250
300
350
Reordered T (°C)
30°C/km
35°C/km
39°C/km
45°C/km
LB-3 Reordering pathways PDM
Age (Mya)
300
250
200
150
100
50
0
0
50
100
150
200
250
300
350
Reordered T (°C)
35°C/km
39°C/km
45°C/km

Figure A- 12

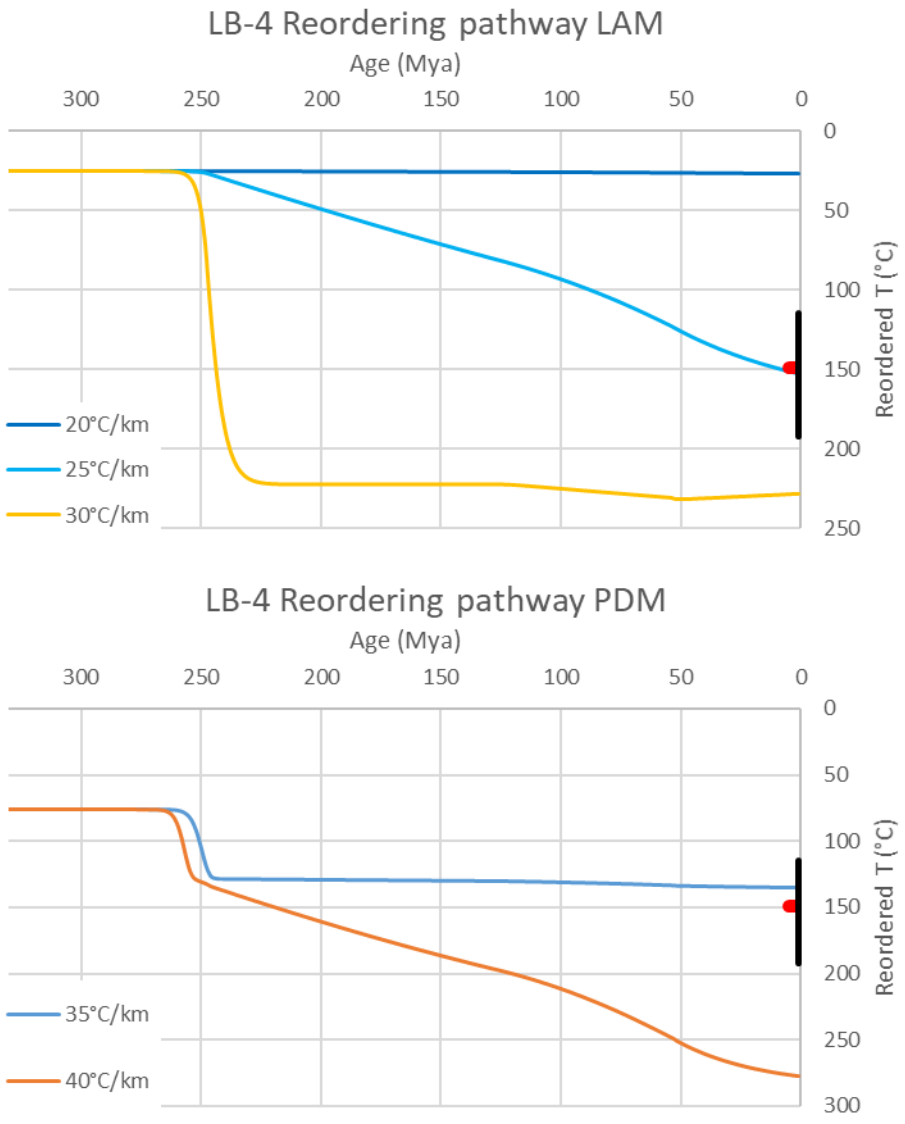
LB-4 Reordering pathway LAM
Age (Mya)
300
250
200
150
100
50
0
0
50
100
150
200
250
Reordered T (°C)
20°C/km
25°C/km
30°C/km
LB-4 Reordering pathway PDM
Age (Mya)
300
250
200
150
100
50
0
0
50
100
150
200
250
300
Reordered T (°C)
35°C/km
40°C/km

Figure A- 13

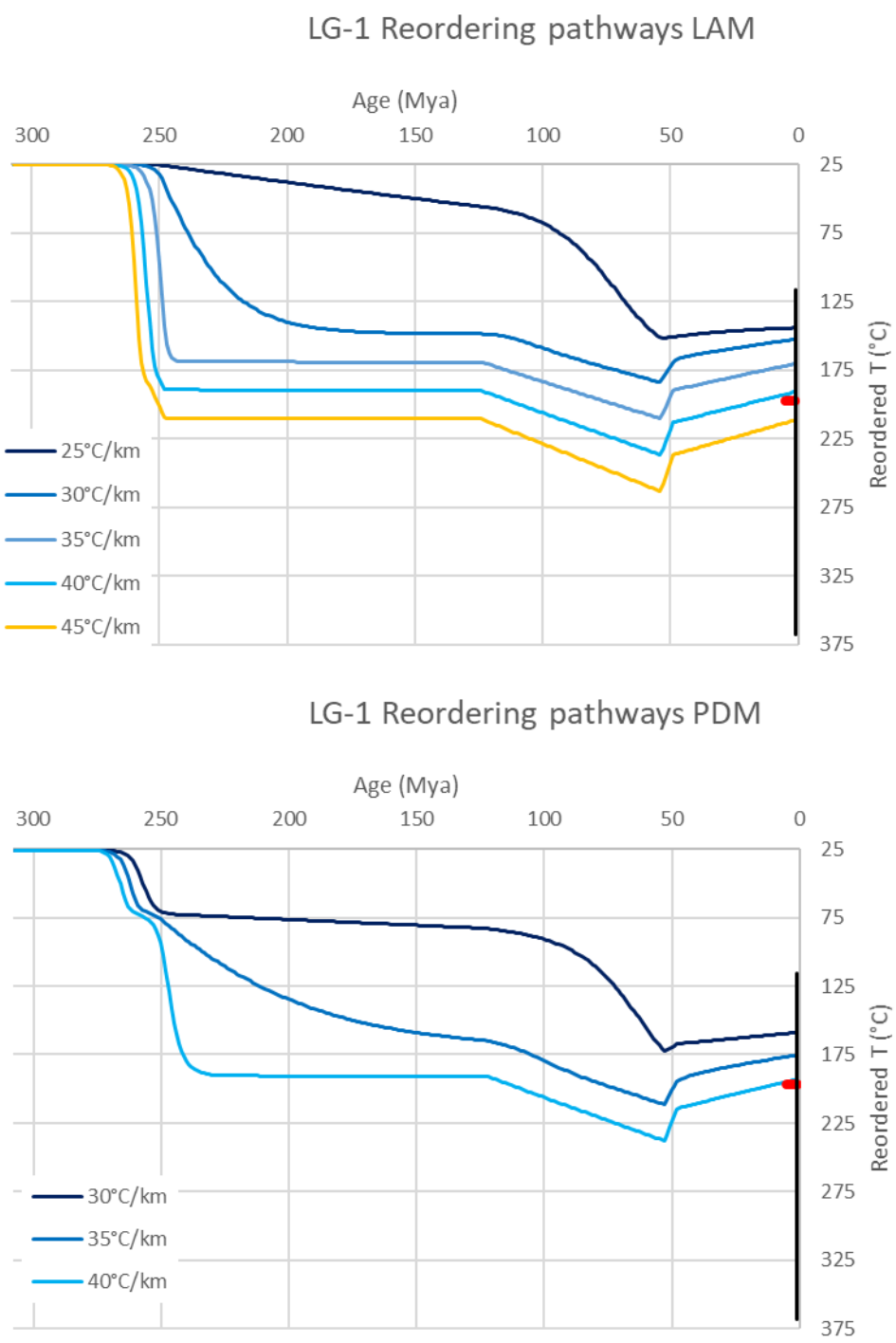
LG-1 Reordering pathways LAM
Age (Mya)
300
250
200
150
100
50
0
25
75
125
175
225
275
325
375
Reordered T (°C)
25°C/km
30°C/km
35°C/km
40°C/km
45°C/km
LG-1 Reordering pathways PDM
Age (Mya)
300
250
200
150
100
50
0
25
75
125
175
225
275
325
375
Reordered T (°C)
30°C/km
35°C/km
40°C/km

Figure A- 14

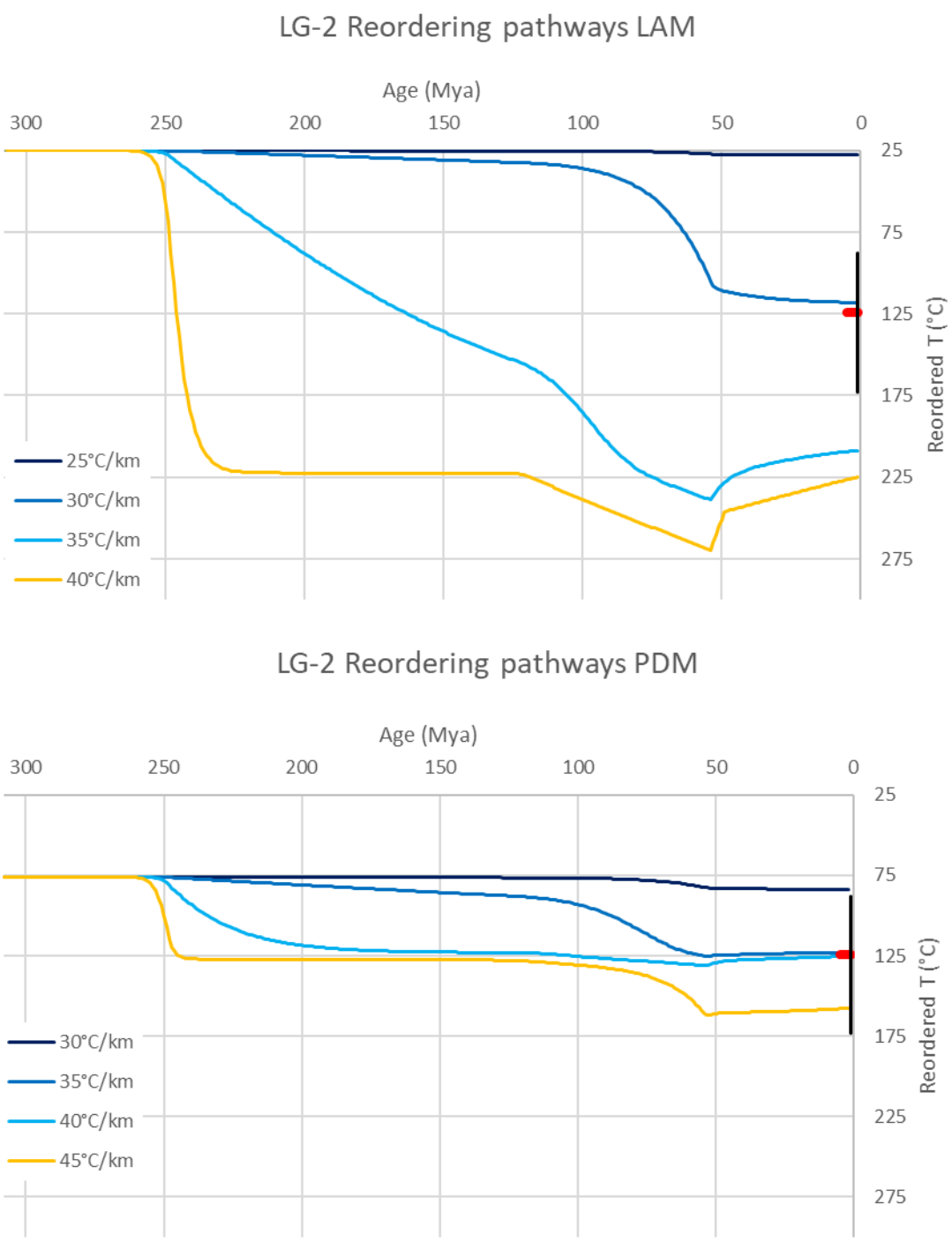
LG-2 Reordering pathways LAM
Age (Mya)
300
250
200
150
100
50
0
25
75
125
175
225
275
Reordered T (°C)
25°C/km
30°C/km
35°C/km
40°C/km
LG-2 Reordering pathways PDM
Age (Mya)
300
250
200
150
100
50
0
25
75
125
175
225
275
Reordered T (°C)
30°C/km
35°C/km
40°C/km
45°C/km

Figure A- 15


LG-3 Reordering pathways (LAM)
Age (Mya)
250
200
150
100
50
0
0
10
20
30
40
50
60
70
80
90
100
Reordered T (°C)
45°C/km
50°C/km
55°C/km
LG-3 Reordering pathways (PDM)
Age (Mya)
250
200
150
100
50
0
25
27
29
31
33
35
37
39
Reordered T (°C)
30°C/km
35°C/km
40°C/km

Figure A- 16

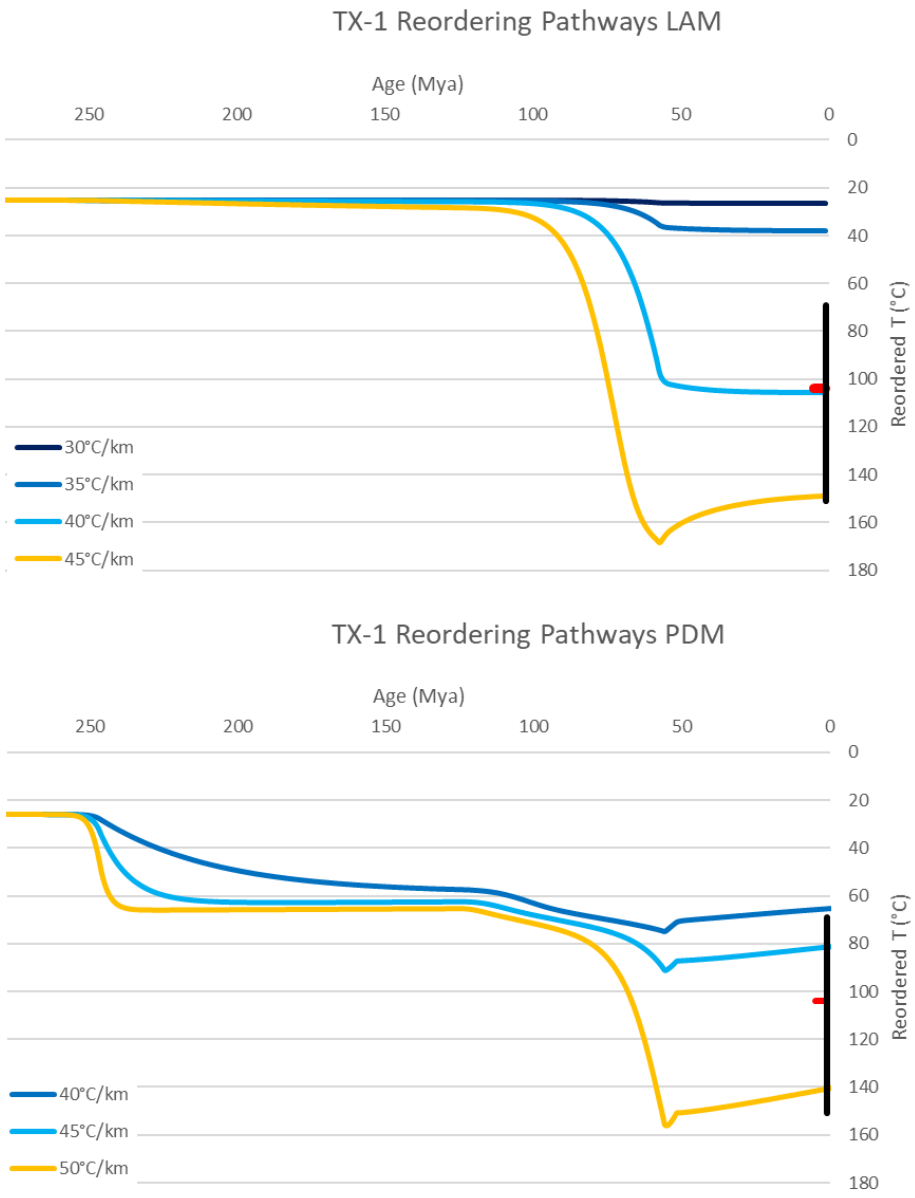
TX-1 Reordering Pathways LAM
Age (Mya)
250
200
150
100
50
0
0
20
40
60
80
100
120
140
160
180
Reordered T (°C)
30°C/km
35°C/km
40°C/km
45°C/km
TX-1 Reordering Pathways PDM
Age (Mya)
250
200
150
100
50
0
0
20
40
60
80
100
120
140
160
180
Reordered T (°C)
40°C/km
45°C/km
50°C/km

Figure A- 17

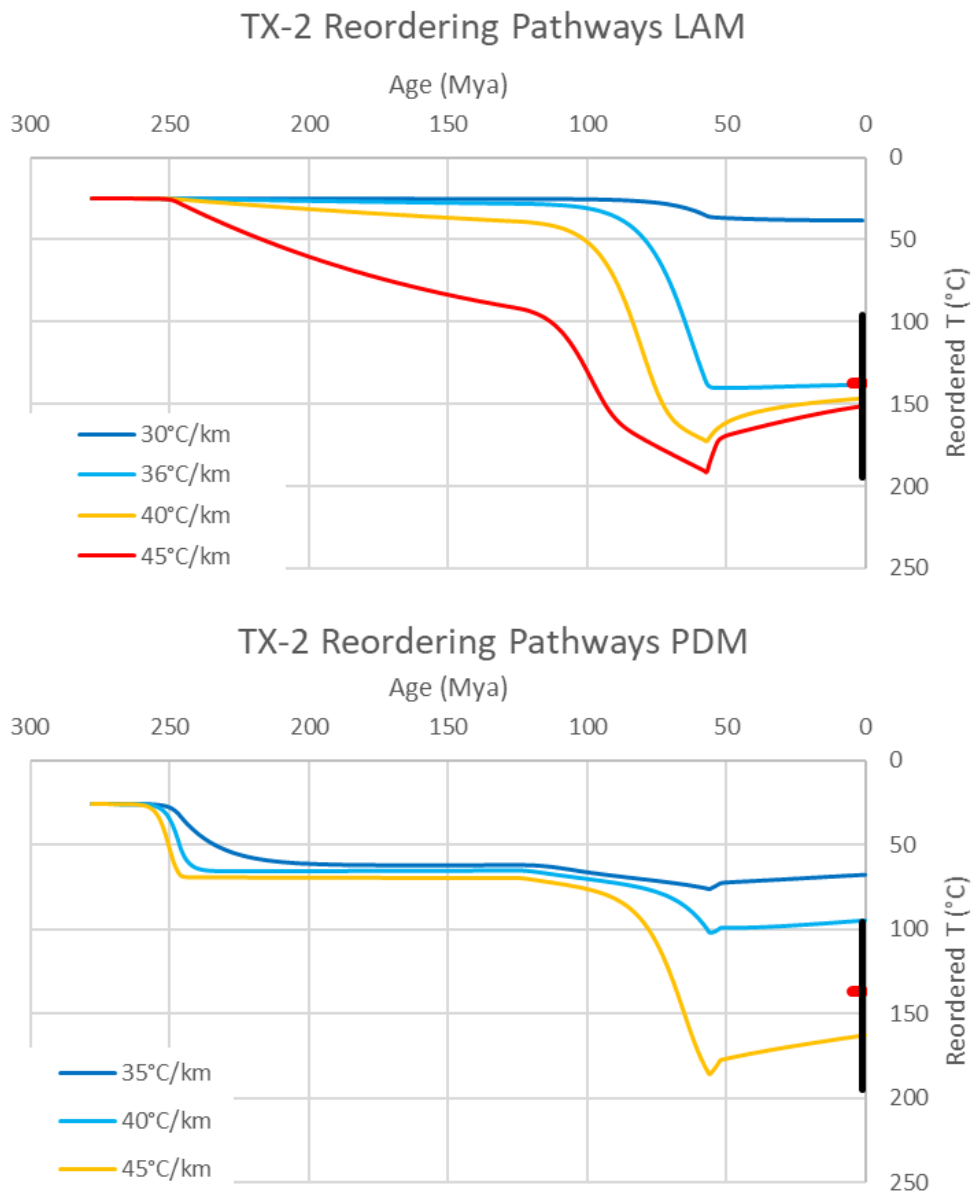
TX-2 Reordering Pathways LAM
Age (Mya)
300
250
200
150
100
50
0
0
50
100
150
200
250
Reordered T (°C)
30°C/km
36°C/km
40°C/km
45°C/km
TX-2 Reordering Pathways PDM
Age (Mya)
300
250
200
150
100
50
0
0
50
100
150
200
250
Reordered T (°C)
35°C/km
40°C/km
45°C/km

Figure A- 18

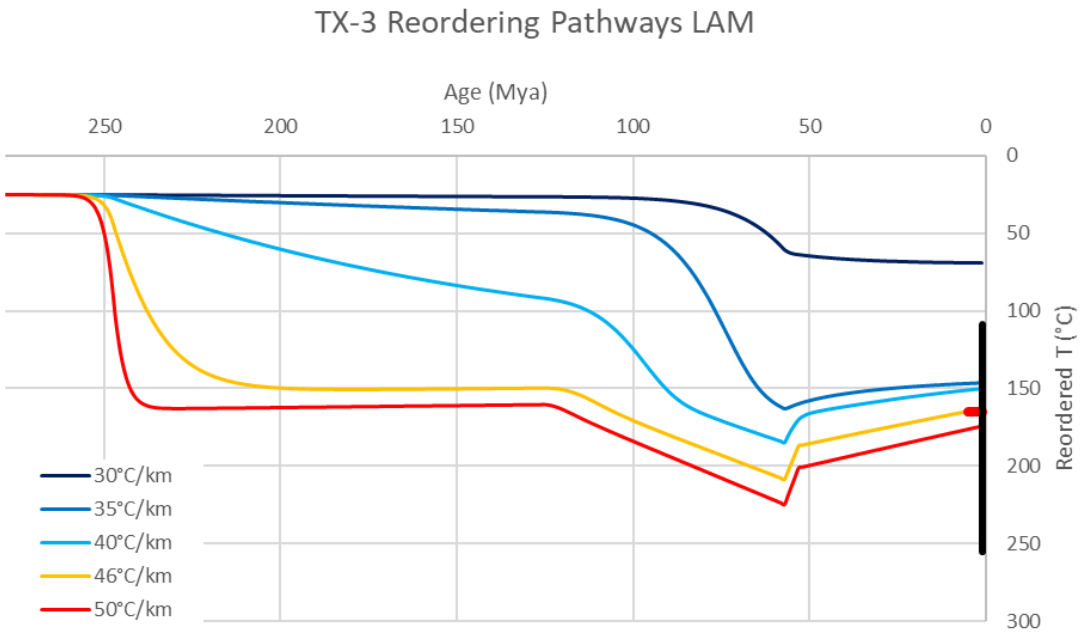
TX-3 Reordering Pathways LAM
Age (Mya)
250
200
150
100
50
0
0
50
100
150
200
250
300
Reordered T (°C)
30°C/km
35°C/km
40°C/km
46°C/km
50°C/km

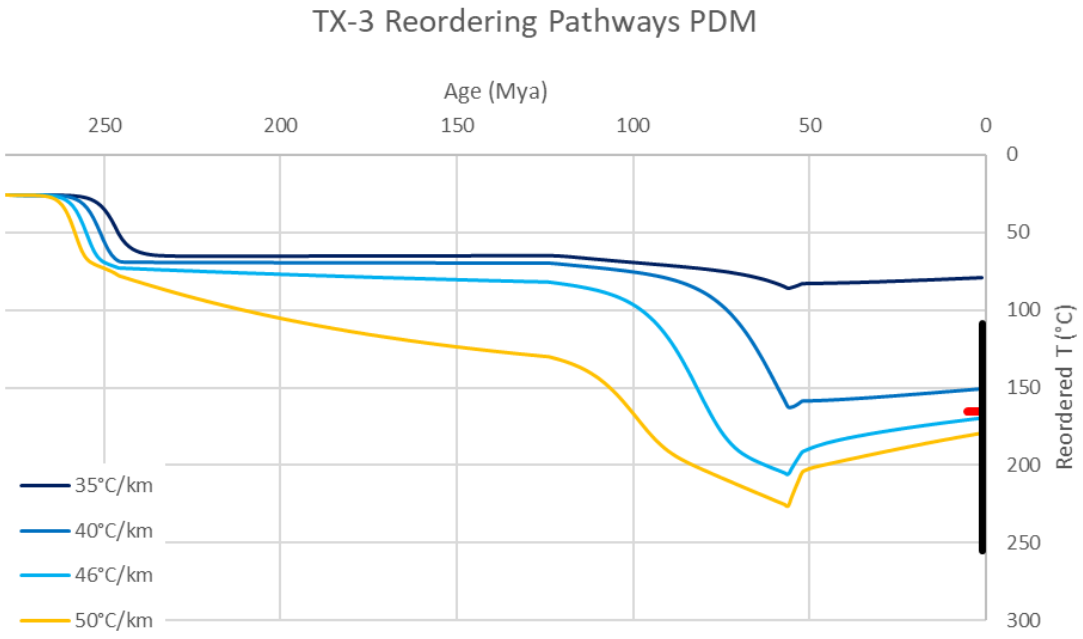
TX-3 Reordering Pathways PDM
Age (Mya)
250
200
150
100
50
0
0
50
100
150
200
250
300
Reordered T (°C)
35°C/km
40°C/km
46°C/km
50°C/km

Figure A- 19

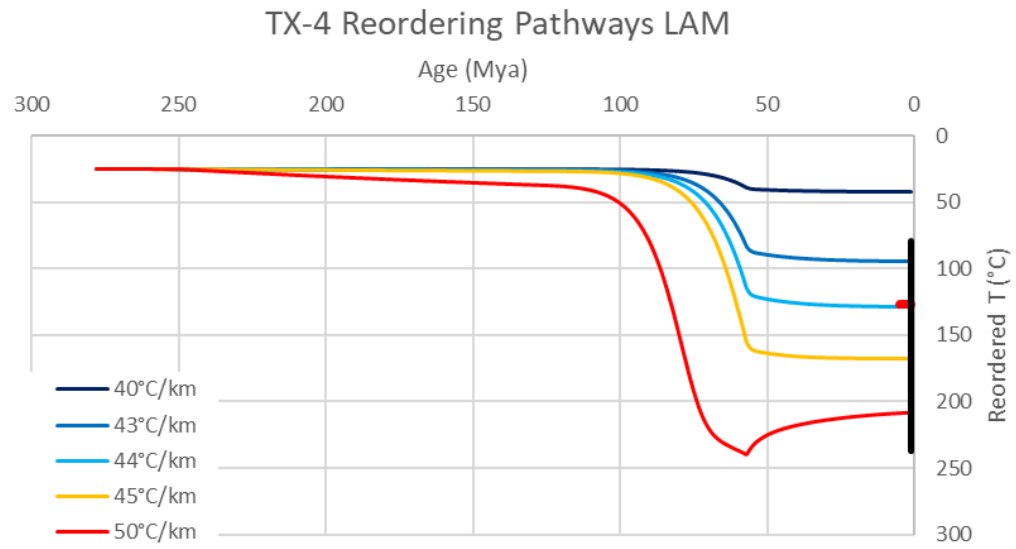
TX-4 Reordering Pathways LAM
Age (Mya)
300
250
200
150
100
50
0
0
50
100
150
200
250
300
Reordered T (°C)
40°C/km
43°C/km
44°C/km
45°C/km
50°C/km

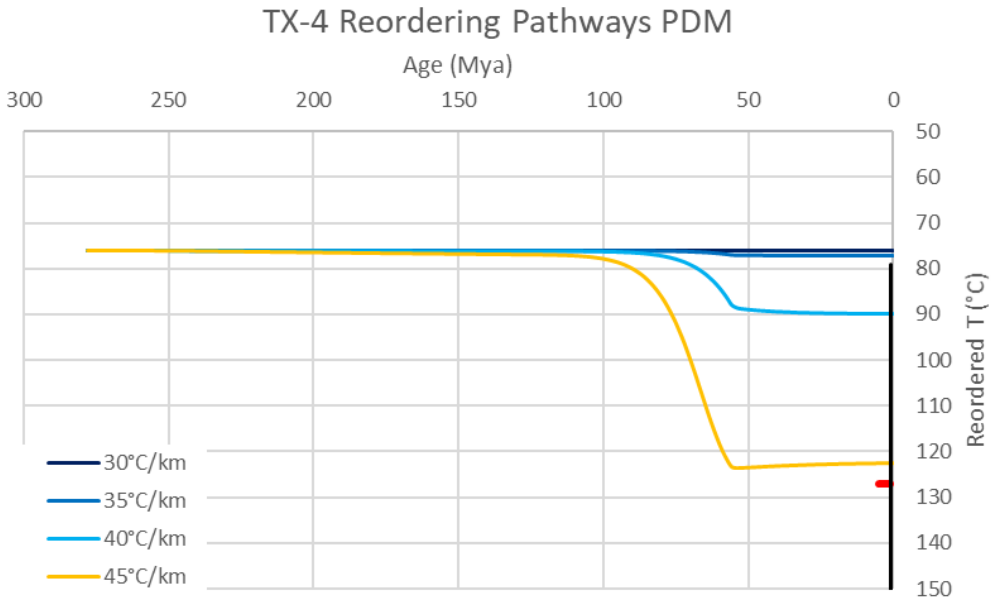
TX-4 Reordering Pathways PDM
Age (Mya)
300
250
200
150
100
50
0
50
60
70
80
90
100
110
120
130
140
150
Reordered T (°C)
30°C/km
35°C/km
40°C/km
45°C/km

Figure A- 20

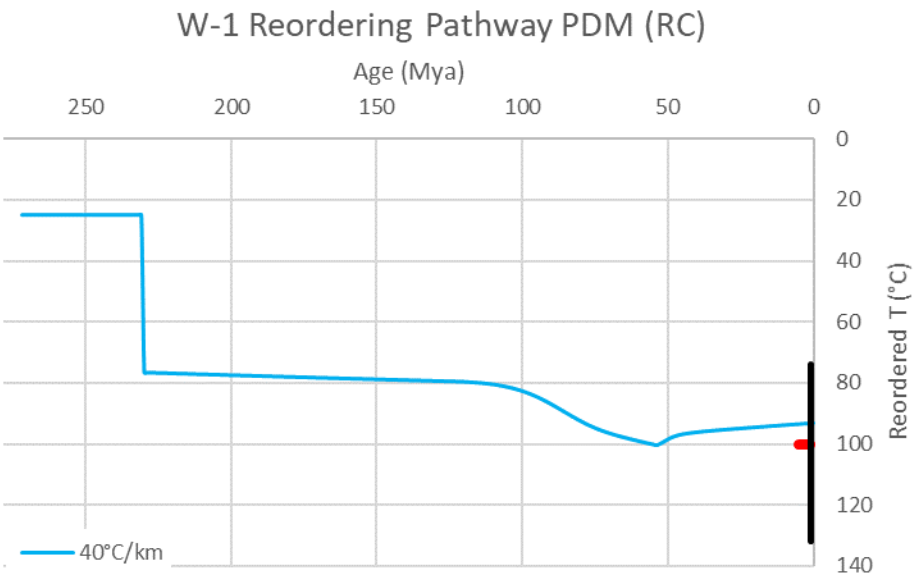
W-1 Reordering Pathway PDM (RC)
Age (Mya)
250
200
150
100
50
0
0
20
40
60
80
100
120
140
Reordered T (°C)
40°C/km

Figure A- 21

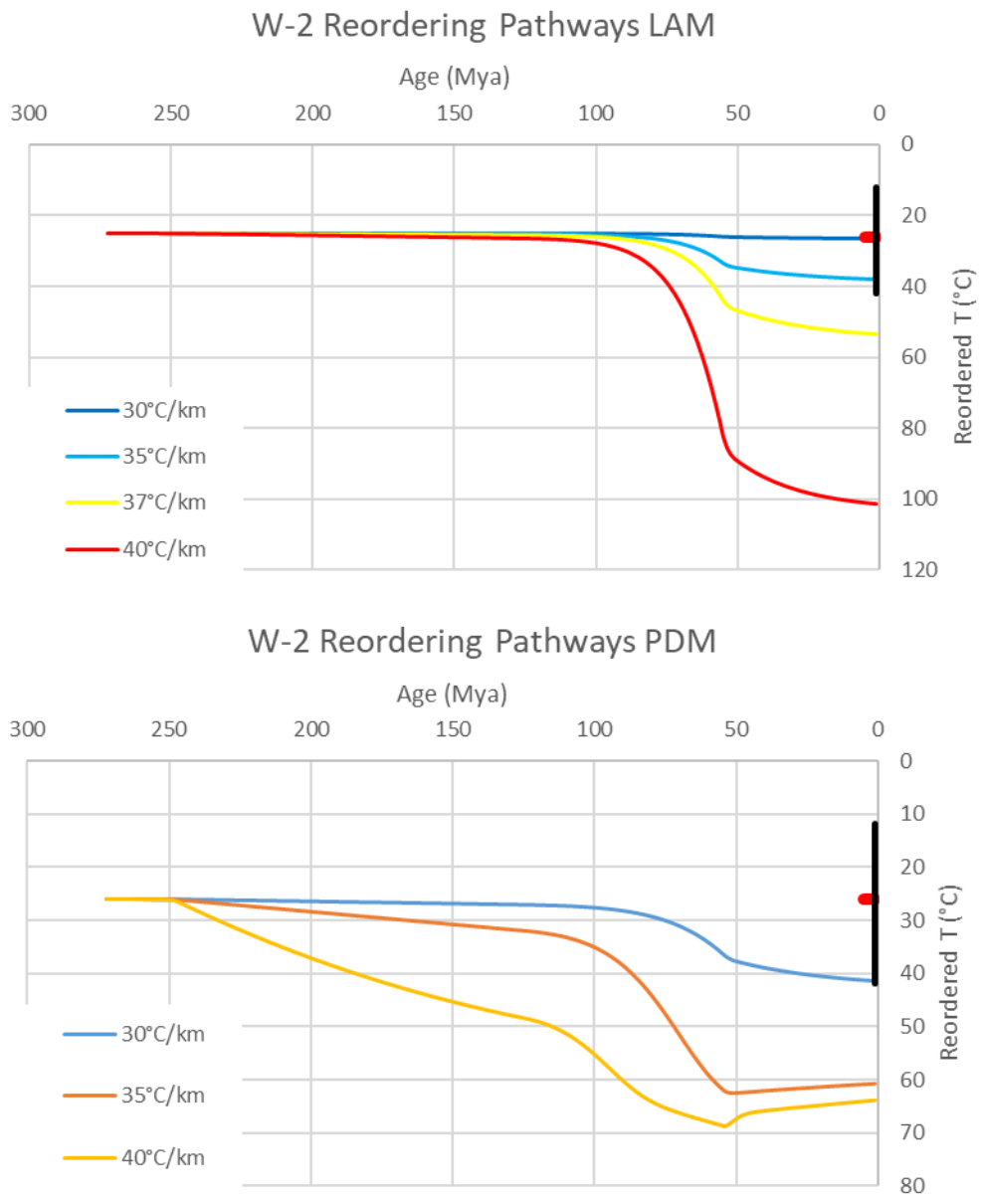
W-2 Reordering Pathways LAM
Age (Mya)
300
250
200
150
100
50
0
0
20
40
60
80
100
120
Reordered T (°C)
30°C/km
35°C/km
37°C/km
40°C/km
W-2 Reordering Pathways PDM
Age (Mya)
300
250
200
150
100
50
0
0
10
20
30
40
50
60
70
80
Reordered T (°C)
30°C/km
35°C/km
40°C/km

Figure A- 22

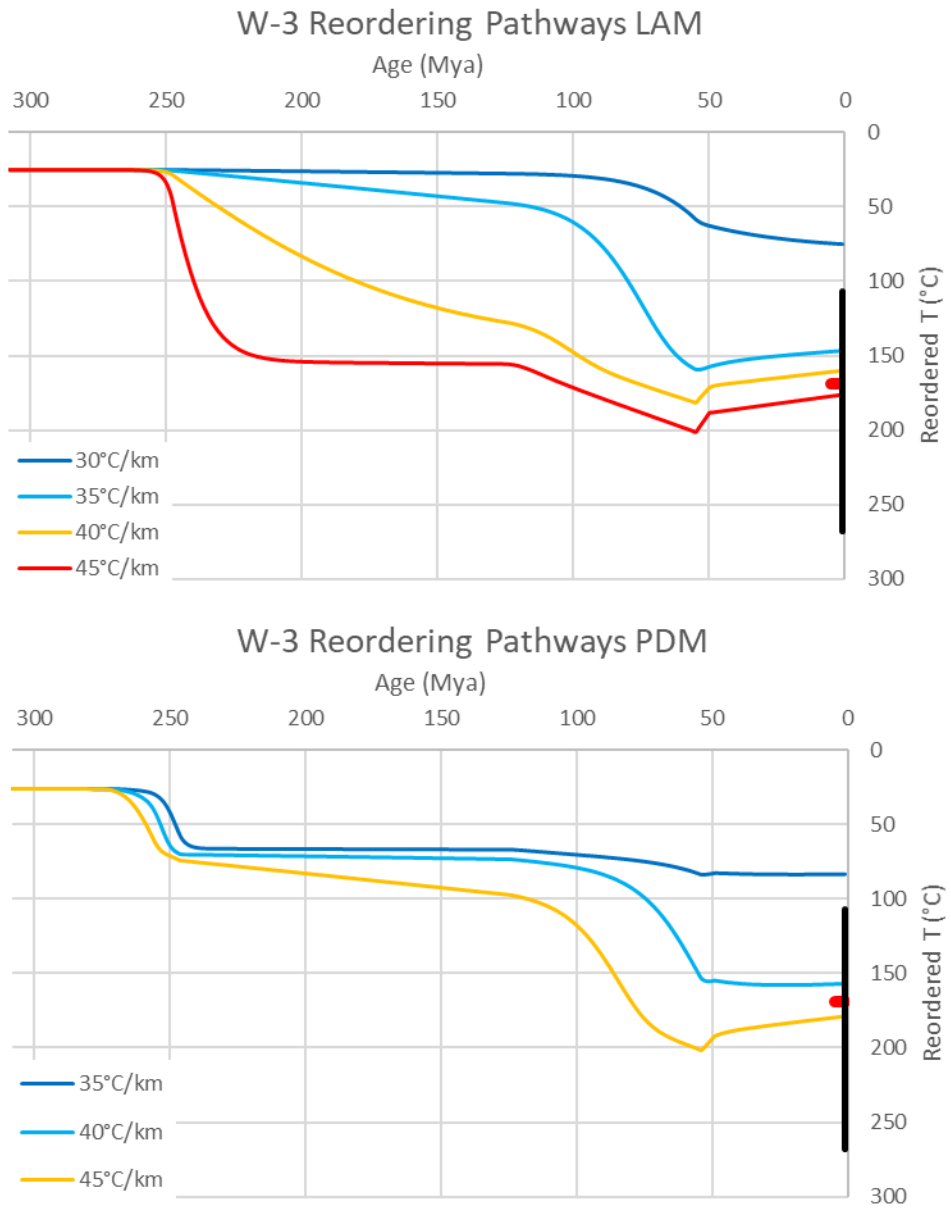
W-3 Reordering Pathways LAM
Age (Mya)
300
250
200
150
100
50
0
0
50
100
150
200
250
300
Reordered T (°C)
30°C/km
35°C/km
40°C/km
45°C/km
W-3 Reordering Pathways PDM
Age (Mya)
300
250
200
150
100
50
0
0
50
100
150
200
250
300
Reordered T (°C)
35°C/km
40°C/km
45°C/km

Figure A- 23

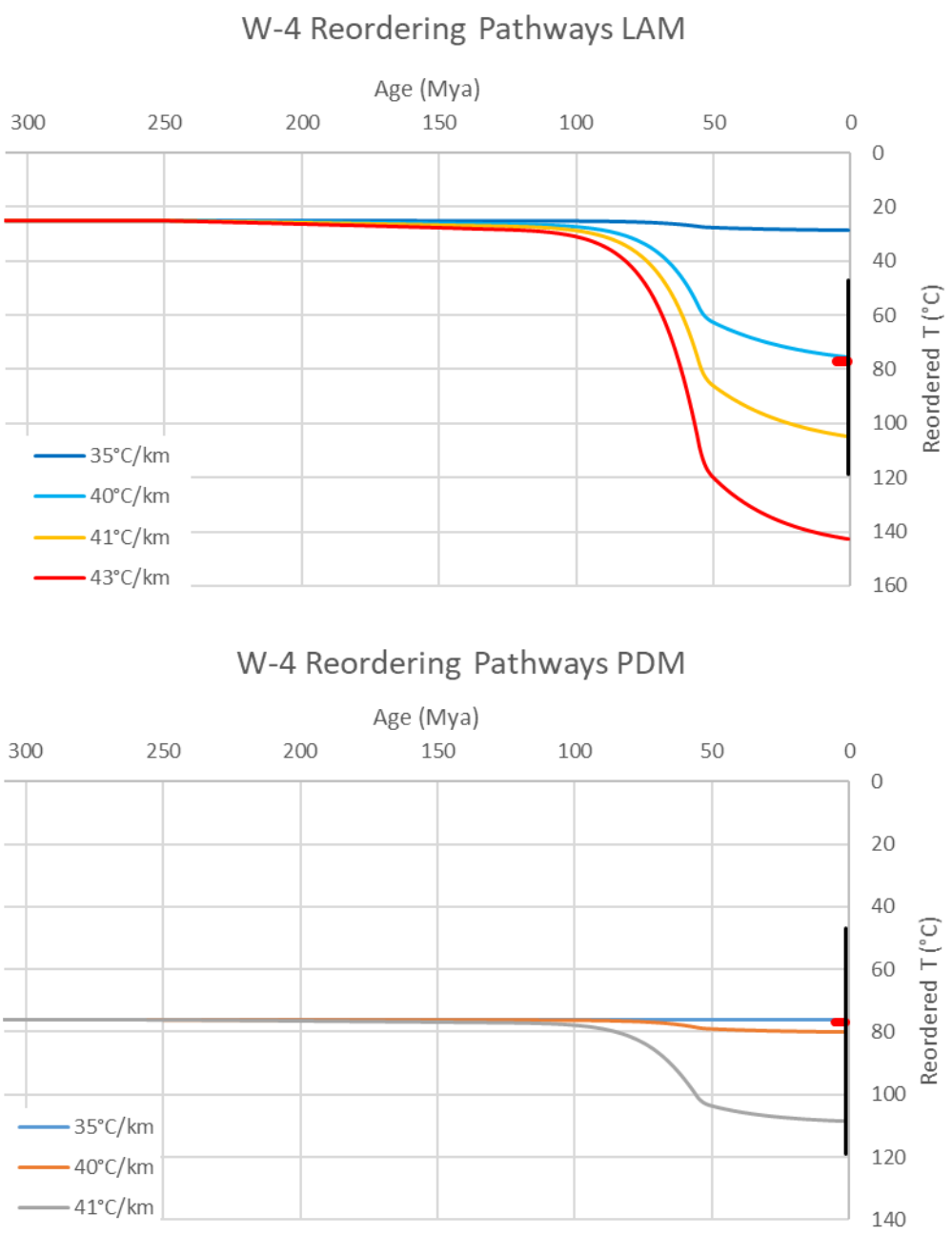
W-4 Reordering Pathways LAM
Age (Mya)
300
250
200
150
100
50
0
0
20
40
60
80
100
120
140
160
Reordered T (°C)
35°C/km
40°C/km
41°C/km
43°C/km
W-4 Reordering Pathways PDM
Age (Mya)
300
250
200
150
100
50
0
0
20
40
60
80
100
120
140
Reordered T (°C)
35°C/km
40°C/km
41°C/km

Figure A- 24

APPENDIX D

Table A-2- Project standards (ETH 1-4)

Time Stamp	Identifier	$\delta^{13}C$ VPDB	$\delta^{18}O$ VPDB	ETF Slope	ETF Intercept	(Δ_{47}) CDES
2018-03-30 00:06	ETH-3	1.58	-1.84	1.219114212	0.770143685	0.607
2018-03-30 11:58	ETH-1	1.99	-2.23	1.511269304	0.841012451	-0.019
2018-03-30 12:47	ETH-1	2.03	-2.20	1.225223029	0.785012405	0.307
2018-03-30 13:35	ETH-2	-10.28	-18.74	1.32782131	0.793867859	0.217
2018-03-30 14:26	ETH-2	-10.29	-18.89	1.366141037	0.824384008	0.361
2018-03-30 15:13	ETH-3	1.64	-1.74	1.378502588	0.828373719	0.644
2018-03-30 16:03	ETH-3	1.70	-1.68	1.59308896	0.900861677	0.845
2018-03-30 16:50	ETH-4	-10.29	-18.86	1.419786979	0.825006429	0.383
2018-03-30 17:41	ETH-4	-10.17	-18.41	1.475652946	0.859759621	0.673
2018-03-30 18:28	ETH-1	1.98	-2.27	1.419001798	0.832411291	0.236
2018-03-30 19:19	ETH-2	-10.05	-18.23	1.316419375	0.810967693	0.443
2018-03-30 20:07	ETH-3	1.65	-1.84	1.192659126	0.76049893	0.525
2018-03-30 20:57	ETH-4	-10.22	-18.68	1.177975153	0.782082928	0.553
2018-03-31 15:55	ETH-3	1.70	-1.67	1.178729958	0.778659662	0.611
2018-03-31 16:44	ETH-4	-10.25	-18.70	1.198354811	0.795413659	0.518
2018-03-31 17:33	ETH-1	2.03	-2.13	1.075590909	0.765825443	0.392
2018-03-31 18:23	ETH-2	-10.23	-18.64	1.241966218	0.822888085	0.360
2018-03-31 19:12	ETH-3	1.66	-1.72	1.449492743	0.883839324	0.837
2018-03-31 20:01	ETH-4	-10.23	-18.71	1.383312948	0.851534918	0.530
2018-04-02 14:04	ETH-1	2.06	-2.04	1.370575588	0.833159478	0.086
2018-04-02 22:22	ETH-1	2.06	-2.10	1.273455845	0.805593102	-0.040
2018-04-02 23:14	ETH-2	-10.13	-18.51	1.256293835	0.785437698	0.083
2018-04-03 00:06	ETH-3	1.51	-2.13	1.137750389	0.773185262	0.605
2018-04-03 00:56	ETH-4	-10.19	-18.61	1.106452827	0.761621949	0.458
2018-04-03 04:55	ETH-3	1.68	-1.77	1.119134238	0.756335392	0.575
2018-04-03 05:47	ETH-4	-10.25	-18.70	1.151236929	0.773835387	0.544
2018-04-04 16:20	ETH-1	2.02	-2.16	0.96439645	0.734527123	0.476
2018-04-04 17:10	ETH-2	-10.20	-18.58	0.916794656	0.697091599	0.575
2018-04-04 18:01	ETH-3	1.65	-1.71	0.92951077	0.70231835	0.731
2018-04-04 18:50	ETH-4	-10.27	-18.72	0.885499202	0.682839449	0.539
2018-04-05 06:10	ETH-4	-10.24	-18.69	0.920750086	0.689240392	0.530
2018-04-05 06:59	ETH-3	1.72	-1.66	0.926306383	0.697303794	0.564
2018-04-05 07:49	ETH-2	-10.18	-18.57	0.823806614	0.663232076	0.278
2018-04-05 08:37	ETH-1	1.99	-2.25	1.166824191	0.745513222	0.363
2018-04-05 17:11	ETH-1	2.04	-2.15	1.035335328	0.682706777	0.304
2018-04-05 17:58	ETH-2	-10.23	-18.66	1.101977436	0.684855324	0.040

2018-04-05 18:47	ETH-3	1.66	-1.73	1.078297521	0.72489718	1.007
2018-04-05 19:35	ETH-4	-10.26	-18.77	0.924279489	0.655797322	0.465
2018-04-06 06:52	ETH-4	-10.12	-18.43	1.072365888	0.710283604	0.050
2018-04-06 07:42	ETH-3	1.66	-1.67	0.914049064	0.660276413	0.322
2018-04-06 09:20	ETH-1	1.94	-2.26	1.085605832	0.730723997	0.212
2018-04-06 13:24	ETH-1	2.02	-2.16	0.973156269	0.703981618	0.492
2018-04-06 14:10	ETH-2	-10.20	-18.63	0.827992144	0.663156972	0.515
2018-04-06 14:58	ETH-3	1.64	-1.73	1.053621463	0.738570948	0.921
2018-04-06 15:47	ETH-4	-10.25	-18.69	0.960662568	0.721783698	0.719
2018-04-07 11:23	ETH-1	2.06	-2.12	0.982204226	0.703922656	0.112
2018-04-07 12:12	ETH-2	-10.12	-18.41	1.086419268	0.766558906	0.173
2018-04-07 13:00	ETH-3	1.57	-1.86	1.049183946	0.75341475	0.572
2018-04-07 13:48	ETH-4	-10.25	-18.75	0.942606026	0.693368134	0.339
2018-04-09 14:43	ETH-1	2.06	-2.19	1.008567768	0.739374827	0.416
2018-04-09 15:30	ETH-2	-10.21	-18.61	1.064653704	0.750842687	0.112
2018-04-09 16:20	ETH-3	1.60	-1.92	0.974111754	0.742377914	0.733
2018-04-09 17:07	ETH-4	-10.24	-18.70	0.910333287	0.739350993	0.585
2018-04-09 20:54	ETH-1	2.04	-2.13	0.972983931	0.772656723	0.156
2018-04-10 19:18	ETH-1	2.01	-2.13	1.049735671	0.825768535	0.314
2018-04-10 20:08	ETH-2	-10.24	-18.66	1.089284654	0.838128213	0.258
2018-04-10 20:58	ETH-3	1.73	-1.55	1.087526676	0.835345044	0.660
2018-04-13 16:17	ETH-3	1.62	-1.98	1.022529178	0.800808559	0.553
2018-04-14 12:22	ETH-1	2.01	-2.18	1.032148334	0.80321346	0.195
2018-04-14 13:10	ETH-2	-10.15	-18.49	0.978599118	0.795646814	0.250
2018-04-14 14:00	ETH-3	1.66	-1.70	0.991724035	0.799513837	0.688
2018-04-14 14:48	ETH-4	-10.24	-18.67	0.978473895	0.797000017	0.517
2018-04-14 22:44	ETH-1	2.02	-2.21	1.026409346	0.830381261	0.223
2018-04-14 23:33	ETH-2	-10.26	-18.72	1.014668184	0.829301085	0.360
2018-04-15 00:22	ETH-3	1.65	-1.75	1.039970297	0.845224224	0.678
2018-04-15 01:11	ETH-4	-10.19	-18.59	1.037728105	0.843483748	0.555
2018-04-15 15:11	ETH-1	2.04	-2.12	1.052381677	0.847798441	0.270
2018-04-15 15:58	ETH-2	-10.27	-18.72	1.036681956	0.826702643	0.203
2018-04-15 16:45	ETH-3	1.63	-1.79	0.973389211	0.792520665	0.599
2018-04-15 17:32	ETH-4	-10.18	-18.58	0.981155505	0.80204741	0.581
2018-04-16 01:30	ETH-1	2.05	-2.13	1.001144542	0.809652705	0.190
2018-04-16 02:18	ETH-2	-10.30	-18.71	1.012967098	0.813454628	0.201
2018-04-16 03:06	ETH-3	1.58	-1.86	1.06704903	0.827087895	0.615
2018-04-16 03:55	ETH-4	-10.11	-18.46	1.104476237	0.83208757	0.469
2018-04-16 15:09	ETH-1	2.06	-2.11	1.050444202	0.80055516	0.211
2018-04-16 15:58	ETH-2	-10.10	-18.52	1.014866126	0.790177533	0.333
2018-04-16 16:46	ETH-3	1.61	-1.83	1.044822513	0.803508524	0.700
2018-04-16 17:33	ETH-4	-10.29	-18.75	1.078947574	0.816139494	0.659
2018-04-17 00:41	ETH-1	2.06	-2.10	1.108778125	0.80338077	0.083
2018-04-17 01:28	ETH-2	-10.16	-18.56	1.104702965	0.807814551	0.229
2018-04-17 03:04	ETH-4	-10.12	-18.58	1.149183149	0.825624106	0.447
2018-04-17 13:06	ETH-1	2.10	-2.03	1.062903886	0.787525451	0.406
2018-04-17 13:57	ETH-2	-10.25	-18.65	1.085016116	0.800773497	0.484
2018-04-17 14:46	ETH-3	1.48	-2.00	1.111736323	0.814154409	0.836
2018-04-17 22:50	ETH-1	2.10	-2.07	1.170153571	0.828863073	0.129

2018-04-18 00:26	ETH-3	1.49	-1.99	1.229877482	0.880834515	0.686
2018-04-18 01:15	ETH-4	-10.21	-18.59	1.197695404	0.879458815	0.567
2018-04-18 13:32	ETH-1	2.07	-2.11	1.121998424	0.873647875	0.389
2018-04-18 15:06	ETH-3	1.65	-1.80	1.253584682	0.925762785	0.712
2018-04-19 00:24	ETH-3	1.68	-1.75	1.195860106	0.896136378	0.602
2018-04-19 01:11	ETH-4	-10.18	-18.61	1.282681554	0.952721183	0.780
2018-04-19 17:51	ETH-1	2.04	-2.10	1.145236227	0.885747269	0.268
2018-04-19 18:38	ETH-2	-10.27	-18.75	1.010515216	0.84605586	0.176
2018-04-19 19:28	ETH-3	1.63	-1.77	1.016964892	0.85803787	0.518
2018-04-19 20:18	ETH-4	-10.12	-18.49	0.949011236	0.81750397	0.339
2018-04-20 03:25	ETH-1	2.06	-2.12	1.208996888	0.939799398	0.124
2018-04-20 04:12	ETH-2	-10.23	-18.64	1.22699003	0.946722698	0.108
2018-04-20 04:58	ETH-3	1.61	-1.81	1.10686082	0.902068529	0.610
2018-04-20 05:47	ETH-4	-10.23	-18.64	1.174729815	0.937635345	0.590
2018-04-20 14:05	ETH-1	2.04	-2.15	1.13165176	0.921507762	0.366
2018-04-20 14:52	ETH-2	-10.26	-18.71	1.174105344	0.946461763	0.253
2018-04-20 15:38	ETH-3	1.68	-1.74	1.152405167	0.93347718	0.625
2018-04-20 16:26	ETH-4	-10.21	-18.66	1.229532367	0.971787816	0.558
2018-04-20 23:30	ETH-1	2.07	-2.11	1.214148982	0.957130842	0.229
2018-04-21 00:17	ETH-2	-10.22	-18.60	1.118825539	0.916041098	0.385
2018-04-21 01:03	ETH-3	1.63	-1.80	1.252407237	0.979562	0.826
2018-04-21 01:50	ETH-4	-10.19	-18.60	1.231123384	0.956140751	0.581
2018-04-21 14:12	ETH-1	2.10	-2.11	1.145323356	0.909688653	0.342
2018-04-21 15:00	ETH-2	-10.17	-18.58	1.248580524	0.946611134	0.159
2018-04-21 15:48	ETH-3	1.53	-1.87	1.217465542	0.947261105	0.765
2018-04-21 23:39	ETH-1	2.04	-2.15	1.188813848	0.927934917	0.243
2018-04-22 00:26	ETH-2	-10.23	-18.65	1.128449706	0.898039815	0.246
2018-04-22 01:13	ETH-3	1.61	-1.87	1.037727046	0.854652434	0.539
2018-04-22 02:00	ETH-4	-10.20	-18.64	1.147591191	0.909537071	0.396
2018-04-23 02:50	ETH-1	2.06	-2.09	1.140333079	0.913704571	0.171
2018-04-23 04:27	ETH-3	1.63	-1.84	1.10215322	0.897274841	0.709
2018-04-23 05:15	ETH-4	-10.18	-18.58	1.071312173	0.901461251	0.593
2018-04-24 18:03	ETH-1	2.02	-2.09	1.114850443	0.907998123	0.366
2018-04-25 00:21	ETH-1	2.07	-2.09	1.100452848	0.887971761	0.244
2018-04-25 15:24	ETH-1	2.04	-2.12	1.11298837	0.881573553	0.228
2018-04-25 16:12	ETH-2	-10.25	-18.68	1.070812401	0.869148128	0.220
2018-04-25 17:51	ETH-4	-10.23	-18.65	1.091939497	0.878388322	0.358
2018-04-26 02:29	ETH-1	2.03	-2.21	1.0559393	0.864827691	0.296
2018-04-26 03:20	ETH-2	-10.24	-18.65	1.032181511	0.8479576	0.284
2018-04-26 04:11	ETH-3	1.53	-1.98	1.226315232	0.926059293	0.824
2018-04-26 12:25	ETH-1	2.08	-2.03	1.103712053	0.861948129	0.340
2018-04-26 13:13	ETH-2	-10.22	-18.57	1.077415069	0.843870891	0.302
2018-04-26 14:03	ETH-3	1.63	-1.71	1.103770975	0.866383412	0.772
2018-04-26 14:53	ETH-4	-10.21	-18.59	1.054000289	0.850552125	0.627
2018-04-27 00:12	ETH-2	-10.09	-18.54	1.104461986	0.857494068	0.079
2018-04-27 01:01	ETH-3	1.57	-1.90	0.989234179	0.799986608	0.500
2018-04-27 01:54	ETH-4	-10.22	-18.73	0.96078603	0.780225013	0.449
2018-04-27 15:33	ETH-1	2.00	-2.28	0.974556258	0.799742405	0.343
2018-04-27 16:25	ETH-2	-10.27	-18.69	0.908042178	0.770226839	0.412

2018-04-27 17:16	ETH-3	1.63	-1.88	0.972910268	0.797829613	0.686
2018-04-27 18:08	ETH-4	-10.24	-18.65	0.939100647	0.796309365	0.629
2018-04-28 02:24	ETH-1	2.12	-2.05	0.933038855	0.78806057	0.173
2018-04-28 03:15	ETH-2	-10.22	-18.61	0.954694698	0.80444561	0.161
2018-04-28 04:06	ETH-3	1.61	-1.71	0.954045267	0.807914286	0.639
2018-04-28 04:55	ETH-4	-10.19	-18.57	0.997392514	0.822182188	0.551
2018-04-28 12:10	ETH-1	2.06	-2.12	0.956859366	0.797630525	0.257
2018-04-28 12:57	ETH-2	-10.15	-18.55	0.93157587	0.782358388	0.268
2018-04-28 13:44	ETH-3	1.60	-1.81	0.924168391	0.79337981	0.774
2018-04-28 23:36	ETH-1	2.06	-2.10	0.87409257	0.772106144	0.225
2018-04-29 00:23	ETH-2	-10.20	-18.61	0.877884321	0.77630624	0.198
2018-04-29 01:10	ETH-3	1.68	-1.74	0.889512694	0.789610377	0.619
2018-04-29 01:58	ETH-4	-10.23	-18.66	0.943996336	0.820930104	0.558
2018-04-29 09:06	ETH-1	2.03	-2.21	0.976881371	0.82759728	0.318
2018-04-29 09:53	ETH-2	-10.24	-18.67	1.057789106	0.848157991	0.247
2018-04-29 10:41	ETH-3	1.62	-1.78	1.048549976	0.844666479	0.661
2018-04-29 11:28	ETH-4	-10.24	-18.71	1.062566989	0.857133528	0.568
2018-04-29 21:59	ETH-2	-10.13	-18.46	1.093178915	0.859929503	0.144
2018-04-29 23:36	ETH-4	-10.22	-18.65	1.131304804	0.892968507	0.532
2018-04-30 00:26	ETH-1	2.01	-2.17	1.218273796	0.925121406	0.158
2018-04-30 02:03	ETH-3	1.63	-1.74	1.190195626	0.909060795	0.641
2018-04-30 02:53	ETH-4	-10.21	-18.61	1.22267849	0.914513536	0.417
2018-04-30 14:32	ETH-1	2.02	-2.17	1.157781692	0.897196154	0.366
2018-04-30 15:21	ETH-2	-10.29	-18.74	1.13273152	0.894638898	0.485
2018-04-30 16:59	ETH-4	-10.23	-18.66	1.184417992	0.905337748	0.528
2018-05-01 00:19	ETH-1	2.03	-2.14	1.145141623	0.878464068	0.189
2018-05-01 01:06	ETH-2	-10.30	-18.72	1.13750963	0.877454544	0.270
2018-05-01 01:55	ETH-3	1.65	-1.76	1.207434131	0.893027801	0.698
2018-05-01 02:43	ETH-4	-10.08	-18.45	1.20509507	0.889895211	0.394
2018-05-01 13:18	ETH-1	2.01	-2.18	1.272986877	0.917091903	0.177
2018-05-01 14:05	ETH-2	-10.11	-18.52	1.200615084	0.882582591	0.377
2018-05-01 14:54	ETH-3	1.59	-1.84	1.16042965	0.861962781	0.676
2018-05-01 22:58	ETH-1	2.01	-2.18	1.147017743	0.868463921	0.144
2018-05-01 23:47	ETH-2	-10.14	-18.52	1.107904352	0.864560336	0.319
2018-05-02 00:34	ETH-3	1.64	-1.77	1.145292721	0.885805834	0.765
2018-05-02 01:24	ETH-4	-10.25	-18.68	1.185946953	0.891268991	0.485
2018-05-02 13:39	ETH-1	2.04	-2.19	1.151161853	0.876170424	0.367
2018-05-02 14:29	ETH-2	-10.27	-18.65	1.198546379	0.893739403	0.360
2018-05-02 15:17	ETH-3	1.73	-1.77	1.183913824	0.870782136	0.667
2018-05-02 16:06	ETH-4	-10.25	-18.68	1.218714538	0.884420459	0.507
2018-05-02 23:57	ETH-1	2.05	-2.12	1.305383284	0.922903786	0.111
2018-05-03 00:44	ETH-2	-10.19	-18.64	1.320007158	0.925273303	0.050
2018-05-03 01:34	ETH-3	1.64	-1.75	1.22677197	0.904769217	0.687
2018-05-03 02:23	ETH-4	-10.25	-18.72	1.184677017	0.891290446	0.479
2018-05-03 13:41	ETH-1	2.04	-2.13	1.117430635	0.874489233	0.399
2018-05-03 14:33	ETH-2	-10.17	-18.57	1.149622583	0.889944793	0.389
2018-05-03 15:20	ETH-3	1.61	-1.81	1.087955345	0.870181153	0.695
2018-05-03 16:11	ETH-4	-10.18	-18.61	1.060477914	0.869971306	0.612
2018-05-04 17:15	ETH-4	-10.20	-18.61	1.082942209	0.881462331	0.545

2018-05-04 22:28	ETH-3	1.58	-1.83	1.06280734	0.871775091	0.603
2018-05-04 23:19	ETH-4	-10.19	-18.61	1.056374513	0.87814081	0.512
2018-05-05 00:12	ETH-1	2.05	-2.08	1.087632966	0.890096433	0.153
2018-05-05 01:03	ETH-2	-10.33	-18.93	1.040651844	0.875863004	0.273
2018-05-05 01:50	ETH-3	1.64	-1.78	1.066242628	0.901807804	0.779
2018-05-05 02:42	ETH-4	-10.15	-18.31	0.92112114	0.832441819	0.478
2018-05-05 03:29	ETH-1	2.08	-2.14	0.907740593	0.839165184	0.237
2018-05-05 04:21	ETH-2	-10.28	-18.80	0.926104095	0.851339961	0.325
2018-05-05 05:12	ETH-3	1.70	-1.67	0.888471818	0.83709023	0.628
2018-05-05 06:04	ETH-4	-10.31	-18.91	0.883427545	0.846483681	0.493
2018-05-05 06:51	ETH-1	2.04	-2.21	0.963217391	0.905122266	0.242
2018-05-05 07:43	ETH-2	-10.28	-18.73	0.998286167	0.923632612	0.249
2018-05-05 14:34	ETH-1	2.06	-2.13	0.992961799	0.921039186	0.252
2018-05-05 15:21	ETH-2	-10.00	-17.94	0.97337181	0.91160089	0.269
2018-05-05 16:09	ETH-3	1.23	-2.61	1.070074512	0.981592115	0.757
2018-05-05 16:57	ETH-4	-10.08	-18.45	1.053964132	0.970796284	0.579
2018-05-05 17:44	ETH-1	1.97	-2.26	0.987322685	0.933502813	0.325
2018-05-09 22:05	ETH-1	2.07	-2.09	1.050995563	0.959565282	0.043
2018-05-09 22:56	ETH-2	-10.29	-18.84	1.061676662	0.969989039	0.110
2018-05-09 23:48	ETH-3	1.92	-0.73	0.879595534	0.853225033	0.461
2018-05-10 05:28	ETH-1	2.06	-2.24	0.946125865	0.914587691	0.324
2018-05-10 06:15	ETH-2	-10.20	-18.65	0.915883577	0.902510309	0.353
2018-05-10 07:05	ETH-3	1.59	-1.95	1.00257518	0.953157514	0.726

**Indicates exclusion based upon Pierce's Criterion (Ross, 2003)*

*Indicates exclusion based upon $\delta^{13}C$ or $\delta^{18}O$ value outside of 2σ window.

Table A-3- Project sample replicates

ID	Identifier	Sample Type	$\delta^{13}C$ VPDB (Final)	$\delta^{18}O$ VPDB (Final)	ETF Slope	ETF Intercept	Δ_{47} CDES (Final)
2018-04-04 22:51	JMR-1	Calcite	3.35	-1.09	0.8613749	0.65531285	0.526
2018-04-04 23:40	JMR-1	Calcite	3.30	-1.27	0.8613749	0.65531285	0.518
2018-04-21 17:24	JMR-1	Calcite	2.93	-1.86	1.1934584	0.92942075	0.415
2018-04-21 19:44	JMR-1	Calcite	3.34	-1.34	1.1934584	0.92942075	0.466
2018-04-21 22:05	JMR-1	Calcite	3.36	-1.34	1.1934584	0.92942075	0.471
2018-04-22 03:34	JMR-1	Calcite	3.24	-1.20	1.0993169	0.90173638	0.604
2018-04-22 05:55	JMR-1	Calcite	3.36	-1.35	1.0993169	0.90173638	0.453
2018-04-24 15:34	JMR-1	Calcite	3.27	-1.52	1.1022906	0.90335037	0.514
2018-04-26 05:49	JMR-1	Calcite	3.25	-1.30	1.1401192	0.87786021	0.555
2018-04-26 08:19	JMR-1	Calcite	3.32	-1.39	1.1401192	0.87786021	0.414
2018-04-26 10:49	JMR-1	Calcite	3.39	-1.06	1.1401192	0.87786021	0.473
2018-04-27 20:41	JMR-1	Calcite	3.35	-1.41	0.8946385	0.77447778	0.393
2018-05-03 21:51	JMR-1	Calcite	3.34	-1.32	1.0507282	0.86158461	0.358

2018-04-13 22:53	JMR-2	Calcite	-0.35	-5.23	1.037321	0.80524673	0.334
2018-04-21 18:11	JMR-2	Calcite	-0.28	-4.99	1.1934584	0.92942075	0.470
2018-04-21 20:32	JMR-2	Calcite	-0.35	-5.17	1.1934584	0.92942075	0.424
2018-04-21 22:53	JMR-2	Calcite	-0.32	-5.13	1.1934584	0.92942075	0.420
2018-04-22 04:22	JMR-2	Calcite	-0.26	-4.98	1.0993169	0.90173638	0.554
2018-04-24 16:25	JMR-2	Calcite	-0.25	-5.10	1.1022906	0.90335037	0.554
2018-04-26 06:36	JMR-2	Calcite	0.10	-4.14	1.1401192	0.87786021	0.297
2018-04-26 09:11	JMR-2	Calcite	-0.25	-5.00	1.1401192	0.87786021	0.416
2018-04-26 11:36	JMR-2	Calcite	-0.22	-4.95	1.1401192	0.87786021	0.394
2018-04-27 21:31	JMR-2	Calcite	-0.25	-4.96	0.8946385	0.77447778	0.353
2018-04-14 00:21	JMR-3	Dolomite	-1.84	-6.13	1.037321	0.80524673	0.404
2018-04-14 01:14	JMR-3	Dolomite	-1.88	-5.93	1.037321	0.80524673	0.503
2018-04-21 18:57	JMR-3	Dolomite	-1.78	-6.32	1.1934584	0.92942075	0.422
2018-04-21 21:19	JMR-3	Dolomite	-1.88	-6.19	1.1934584	0.92942075	0.432
2018-04-22 02:47	JMR-3	Dolomite	-1.85	-6.18	1.0993169	0.90173638	0.547
2018-04-22 05:08	JMR-3	Dolomite	-1.86	-6.17	1.0993169	0.90173638	0.364
2018-04-24 13:52	JMR-3	Dolomite	-1.83	-6.12	1.1022906	0.90335037	0.678
2018-04-26 07:26	JMR-3	Dolomite	-1.79	-6.10	1.1401192	0.87786021	0.417
2018-04-26 09:59	JMR-3	Dolomite	-1.84	-6.05	1.1401192	0.87786021	0.422
2018-04-26 15:43	JMR-3	Dolomite	-1.86	-6.03	1.0444788	0.83556976	0.481
2018-04-27 22:21	JMR-3	Dolomite	-1.63	-6.00	0.8946385	0.77447778	0.552
2018-04-05 20:25	LB-1	Calcite	3.26	-3.14	0.962474	0.67566782	0.572
2018-04-05 23:38	LB-1	Calcite	3.27	-3.14	0.962474	0.67566782	0.667
2018-04-17 06:15	LB-1	Calcite	3.33	-3.02	1.2183277	0.84545342	0.334
2018-04-17 07:03	LB-1	Calcite	3.32	-3.07	1.2183277	0.84545342	0.320
2018-04-26 16:37	LB-1	Calcite	3.27	-3.05	1.0444788	0.83556976	0.432
2018-04-26 18:22	LB-1	Calcite	3.27	-3.02	1.0444788	0.83556976	0.433
2018-04-27 13:48	LB-1	Calcite	3.29	-3.30	1.004115	0.80721562	0.436
2018-04-30 17:48	LB-1	Calcite	3.21	-3.22	1.1814817	0.90198213	0.285
2018-04-30 21:04	LB-1	Calcite	3.24	-3.15	1.1814817	0.90198213	0.398
2018-05-01 03:32	LB-1	Calcite	3.31	-3.09	1.2419225	0.90578623	0.317
2018-05-03 20:14	*LB-1*	*Calcite*	*3.10*	*-3.19*	*1.0507282*	*0.86158461*	*0.098*
2018-04-04 22:03	LB-2	Calcite	2.49	-4.84	0.8613749	0.65531285	0.291
2018-04-05 21:12	LB-2	Calcite	2.50	-4.86	0.962474	0.67566782	0.262
2018-04-06 00:25	LB-2	Calcite	2.48	-4.92	0.962474	0.67566782	0.437
2018-04-15 19:04	LB-2	Calcite	2.42	-4.84	0.9865535	0.80538384	0.405
2018-04-15 19:53	LB-2	Calcite	2.50	-4.76	0.9865535	0.80538384	0.255
2018-04-15 20:40	LB-2	Calcite	2.53	-4.81	0.9865535	0.80538384	0.205
2018-04-16 19:57	LB-2	Calcite	2.52	-4.82	1.0181307	0.77874283	0.215
2018-04-16 20:44	LB-2	Calcite	2.55	-4.77	1.0181307	0.77874283	0.170
2018-04-27 14:41	LB-2	Calcite	2.49	-4.90	1.004115	0.80721562	0.502
2018-04-30 21:52	LB-2	Calcite	2.54	-4.80	1.1814817	0.90198213	0.342
2018-05-01 04:20	LB-2	Calcite	2.49	-4.85	1.2419225	0.90578623	0.351
2018-05-10 01:25	LB-2	Calcite	2.80	-3.86	0.9801053	0.92865726	0.358
2018-05-10 02:15	LB-2	Calcite	2.48	-4.96	0.9801053	0.92865726	0.336

2018-05-10 03:51	LB-2	Calcite	2.53	-4.86	0.9801053	0.92865726	0.513
2018-05-10 04:38	LB-2	Calcite	2.72	-4.43	0.9801053	0.92865726	0.382
2018-04-07 14:36	LB-3	Dolomite	1.36	-7.77	1.0820561	0.75450267	0.286
2018-04-07 15:33	LB-3	Dolomite	1.31	-7.87	1.0820561	0.75450267	0.399
2018-04-15 21:31	LB-3	Dolomite	1.45	-7.55	0.9865535	0.80538384	0.336
2018-04-15 22:19	LB-3	Dolomite	1.46	-7.57	0.9865535	0.80538384	0.313
2018-04-15 23:07	LB-3	Dolomite	1.44	-7.58	0.9865535	0.80538384	0.378
2018-04-26 17:31	LB-3	Dolomite	1.48	-7.57	1.0444788	0.83556976	0.351
2018-04-26 19:09	*LB-3*	*Dolomite*	*1.44*	*-7.56*	*1.0444788*	*0.83556976*	*0.489*
2018-04-27 18:59	LB-3	Dolomite	1.45	-7.57	0.8946385	0.77447778	0.388
2018-04-30 19:25	LB-3	Dolomite	1.44	-7.70	1.1814817	0.90198213	0.316
2018-04-30 22:42	LB-3	Dolomite	1.42	-7.65	1.1814817	0.90198213	0.348
2018-05-01 05:09	LB-3	Dolomite	1.44	-7.63	1.2419225	0.90578623	0.407
2018-04-08 15:02	LB-4	Dolomite	-1.36	-6.22	1.0820561	0.75450267	0.475
2018-04-15 02:00	LB-4	Dolomite	-1.44	-6.32	1.0435437	0.8470825	0.554
2018-04-15 02:48	LB-4	Dolomite	-1.42	-6.25	1.0435437	0.8470825	0.531
2018-04-15 03:37	LB-4	Dolomite	-1.47	-6.29	1.0435437	0.8470825	0.507
2018-04-15 04:25	LB-4	Dolomite	-1.44	-6.24	1.0435437	0.8470825	0.511
2018-04-15 23:55	LB-4	Dolomite	-1.37	-6.24	0.9865535	0.80538384	0.410
2018-04-16 00:43	LB-4	Dolomite	-1.38	-6.14	0.9865535	0.80538384	0.368
2018-04-16 04:42	LB-4	Dolomite	-1.38	-6.31	1.134785	0.84991634	0.391
2018-04-27 19:51	LB-4	Dolomite	-1.35	-6.28	0.8946385	0.77447778	0.459
2018-04-30 23:30	LB-4	Dolomite	-1.38	-6.18	1.1814817	0.90198213	0.398
2018-05-01 05:58	LB-4	Dolomite	-1.41	-6.21	1.2419225	0.90578623	0.384
2018-05-01 06:48	LB-4	Dolomite	-1.41	-6.16	1.2419225	0.90578623	0.355
2018-04-12 17:35	LG-1	Calcite	1.43	-3.52	1.081487	0.83196593	0.674
2018-04-12 18:25	LG-1	Calcite	1.39	-3.54	1.081487	0.83196593	0.649
2018-04-22 21:06	LG-1	Calcite	1.35	-3.51	1.0993169	0.90173638	0.276
2018-04-23 00:22	LG-1	Calcite	1.41	-3.49	1.0993169	0.90173638	0.351
2018-04-23 06:52	LG-1	Calcite	1.67	-2.29	1.1022906	0.90335037	0.407
2018-04-23 08:30	LG-1	Calcite	1.31	-3.45	1.1022906	0.90335037	0.316
2018-04-27 02:45	LG-1	Calcite	1.22	-3.70	1.004115	0.80721562	0.420
2018-04-27 11:10	LG-1	Calcite	1.42	-3.54	1.004115	0.80721562	0.467
2018-05-01 16:33	LG-1	Calcite	1.20	-3.75	1.1182277	0.85032309	0.287
2018-05-01 18:57	LG-1	Calcite	1.61	-3.21	1.1182277	0.85032309	0.173
2018-05-01 21:23	LG-1	Calcite	1.52	-3.54	1.1182277	0.85032309	0.434
2018-05-02 03:00	LG-1	Calcite	1.59	-3.44	1.193166	0.89162628	0.486
2018-05-02 04:36	LG-1	Calcite	1.35	-3.53	1.193166	0.89162628	0.329
2018-04-08 18:20	LG-2	Dolomite	0.25	-7.66	1.0820561	0.75450267	0.338
2018-04-08 19:10	LG-2	Dolomite	0.29	-7.73	1.0820561	0.75450267	0.531
2018-04-14 18:32	LG-2	Dolomite	0.25	-7.70	1.0380572	0.83285203	0.541
2018-04-14 19:19	LG-2	Dolomite	0.25	-7.66	1.0380572	0.83285203	0.559
2018-04-14 20:06	LG-2	Dolomite	0.23	-7.71	1.0380572	0.83285203	0.344
2018-04-14 20:54	LG-2	Dolomite	0.28	-7.59	1.0380572	0.83285203	0.412
2018-04-22 21:55	LG-2	Dolomite	0.29	-7.60	1.0993169	0.90173638	0.376

2018-04-23 01:13	LG-2	Dolomite	0.29	-7.64	1.0993169	0.90173638	0.501
2018-04-27 03:34	LG-2	Dolomite	0.31	-7.65	1.004115	0.80721562	0.440
2018-04-27 11:58	LG-2	Dolomite	0.34	-7.55	1.004115	0.80721562	0.562
2018-05-01 17:20	LG-2	Dolomite	0.25	-7.59	1.1182277	0.85032309	0.354
2018-05-01 19:46	LG-2	Dolomite	0.23	-7.66	1.1182277	0.85032309	0.643
2018-05-01 22:10	LG-2	Dolomite	0.26	-7.64	1.1182277	0.85032309	0.362
2018-05-02 03:47	LG-2	Dolomite	0.47	-7.32	1.193166	0.89162628	0.496
2018-05-02 05:24	LG-2	Dolomite	0.61	-6.61	1.193166	0.89162628	0.633
2018-04-14 16:56	LG-3	Dolomite	0.78	-5.03	1.0380572	0.83285203	0.749
2018-04-23 02:00	LG-3	Dolomite	0.84	-4.84	1.0993169	0.90173638	0.670
2018-04-23 07:42	LG-3	Dolomite	0.87	-4.81	1.1022906	0.90335037	0.700
2018-04-23 09:19	LG-3	Dolomite	0.84	-4.70	1.1022906	0.90335037	0.572
2018-04-27 12:53	LG-3	Dolomite	0.86	-4.88	1.004115	0.80721562	0.699
2018-05-01 18:09	LG-3	Dolomite	0.76	-5.03	1.1182277	0.85032309	0.361
2018-05-01 20:33	LG-3	Dolomite	0.78	-4.96	1.1182277	0.85032309	0.604
2018-05-02 02:10	LG-3	Dolomite	0.81	-4.83	1.193166	0.89162628	0.659
2018-04-10 13:26	*TX-1*	*Calcite*	*0.87*	*-2.21*	*1.0366523*	*0.82221078*	*0.201*
2018-04-10 14:16	TX-1	Calcite	0.82	-2.23	1.0366523	0.82221078	0.498
2018-04-17 16:22	TX-1	Calcite	0.54	-2.69	1.0723648	0.78614415	0.619
2018-04-17 19:35	TX-1	Calcite	0.75	-2.41	1.0723648	0.78614415	0.294
2018-04-28 05:43	TX-1	Calcite	0.67	-2.58	0.9455949	0.79033494	0.479
2018-04-28 08:59	TX-1	Calcite	0.87	-2.35	0.9455949	0.79033494	0.640
2018-04-29 02:46	TX-1	Calcite	0.96	-2.36	0.9579031	0.82298672	0.513
2018-04-29 05:57	TX-1	Calcite	0.86	-2.34	0.9579031	0.82298672	0.595
2018-04-29 12:16	TX-1	Calcite	0.77	-2.43	1.0534482	0.85007694	0.522
2018-05-02 16:53	TX-1	Calcite	0.81	-2.44	1.1927969	0.87838837	0.583
2018-05-02 20:43	TX-1	Calcite	0.45	-2.45	1.1927969	0.87838837	0.412
2018-05-03 03:13	TX-1	Calcite	0.98	-2.25	1.2373224	0.92169017	0.405
2018-04-10 15:07	TX-2	Calcite	1.06	-5.18	1.0366523	0.82221078	0.511
2018-04-10 15:58	TX-2	Calcite	1.08	-5.19	1.0366523	0.82221078	0.586
2018-04-17 17:11	*TX-2*	*Calcite*	*1.05*	*-5.17*	*1.0723648*	*0.78614415*	*0.765*
2018-04-17 20:24	TX-2	Calcite	1.10	-5.02	1.0723648	0.78614415	0.338
2018-04-28 06:31	TX-2	Calcite	1.10	-5.03	0.9455949	0.79033494	0.435
2018-04-28 09:46	TX-2	Calcite	1.06	-5.20	0.9455949	0.79033494	0.550
2018-04-29 03:34	TX-2	Calcite	1.08	-5.20	0.9579031	0.82298672	0.464
2018-04-29 06:45	TX-2	Calcite	1.05	-5.19	0.9579031	0.82298672	0.571
2018-04-29 13:04	TX-2	Calcite	1.08	-5.31	1.0534482	0.85007694	0.498
2018-05-02 18:18	TX-2	Calcite	1.09	-4.98	1.1927969	0.87838837	0.295
2018-05-02 21:31	TX-2	Calcite	1.11	-5.00	1.1927969	0.87838837	0.342
2018-05-03 04:01	TX-2	Calcite	1.13	-5.11	1.2373224	0.92169017	0.465
2018-04-10 16:48	TX-3	Calcite	-0.52	-4.97	1.0366523	0.82221078	0.581
2018-04-10 17:39	TX-3	Calcite	-0.65	-4.98	1.0366523	0.82221078	0.596
2018-04-17 17:59	TX-3	Calcite	-0.53	-4.98	1.0723648	0.78614415	0.271
2018-04-17 21:12	*TX-3*	*Calcite*	*-0.24*	*-3.87*	*1.0723648*	*0.78614415*	*0.022*
2018-04-18 03:48	TX-3	Calcite	-0.29	-4.56	1.2359959	0.90431481	0.448

2018-04-28 07:21	TX-3	Calcite	-0.60	-4.89	0.9455949	0.79033494	0.416
2018-04-28 10:35	TX-3	Calcite	-0.51	-4.95	0.9455949	0.79033494	0.503
2018-04-29 04:22	TX-3	Calcite	-0.69	-5.06	0.9579031	0.82298672	0.421
2018-04-29 07:32	TX-3	Calcite	-0.53	-4.99	0.9579031	0.82298672	0.485
2018-04-29 13:52	TX-3	Calcite	-0.62	-5.01	1.0534482	0.85007694	0.500
2018-05-02 19:07	TX-3	Calcite	-0.55	-4.99	1.1927969	0.87838837	0.268
2018-05-02 22:20	TX-3	Calcite	-0.54	-4.99	1.1927969	0.87838837	0.217
2018-05-03 04:51	TX-3	Calcite	-0.46	-4.96	1.2373224	0.92169017	0.436
2018-04-18 04:37	TX-4	Calcite	-1.41	-5.22	1.2359959	0.90431481	0.746
2018-04-18 19:03	TX-4	Calcite	-1.38	-4.71	1.2260694	0.91354495	0.274
2018-04-18 22:02	TX-4	Calcite	-1.35	-4.69	1.2260694	0.91354495	0.168
2018-04-24 14:43	TX-4	Calcite	-1.35	-4.43	1.1022906	0.90335037	0.775
2018-04-25 19:30	TX-4	Calcite	-1.40	-4.68	1.058742	0.86566495	0.284
2018-04-25 21:13	TX-4	Calcite	-1.42	-4.67	1.058742	0.86566495	0.623
2018-04-28 08:10	TX-4	Calcite	-1.35	-4.56	0.9455949	0.79033494	0.497
2018-04-28 11:22	TX-4	Calcite	-1.67	-5.20	0.9455949	0.79033494	0.448
2018-04-29 08:19	TX-4	Calcite	-1.38	-4.70	0.9579031	0.82298672	0.501
2018-04-29 14:40	TX-4	Calcite	-1.39	-4.75	1.0534482	0.85007694	0.555
2018-04-29 15:27	TX-4	Calcite	-1.42	-4.75	1.0534482	0.85007694	0.529
2018-05-02 19:54	TX-4	Calcite	-1.38	-4.87	1.1927969	0.87838837	0.347
2018-05-02 23:07	TX-4	Calcite	-1.36	-4.72	1.1927969	0.87838837	0.284
2018-05-03 05:40	TX-4	Calcite	-1.35	-4.78	1.2373224	0.92169017	0.407
2018-05-03 06:30	TX-4	Calcite	-1.34	-4.63	1.2373224	0.92169017	0.480
2018-04-05 00:28	W-1	Calcite	3.45	-0.84	0.8613749	0.65531285	0.488
2018-04-05 02:03	W-1	Calcite	3.53	-0.83	0.8613749	0.65531285	0.485
2018-04-19 21:05	W-1	Calcite	3.44	-0.99	1.0650645	0.89121779	0.543
2018-04-20 00:15	W-1	Calcite	3.54	-0.73	1.0650645	0.89121779	0.396
2018-04-20 06:36	W-1	Calcite	3.40	-0.96	1.1659239	0.93212213	0.540
2018-04-20 17:13	W-1	Calcite	3.19	-1.06	1.1439304	0.91879752	0.610
2018-04-20 20:21	W-1	Calcite	3.49	-0.88	1.1439304	0.91879752	0.429
2018-04-21 02:38	W-1	Calcite	3.51	-0.88	1.1875524	0.92790759	0.444
2018-04-25 03:47	W-1	Calcite	3.37	-1.07	1.1040665	0.89192488	0.573
2018-04-25 07:31	W-1	Calcite	3.47	-0.87	1.1040665	0.89192488	0.594
2018-04-06 03:37	*W-2*	*Calcite*	*-10.19*	*-2.42*	*0.962474*	*0.67566782*	*0.450*
2018-04-06 04:26	W-2	Calcite	-9.56	-2.39	0.962474	0.67566782	0.750
2018-04-19 21:52	W-2	Calcite	-9.52	-2.45	1.0650645	0.89121779	0.652
2018-04-20 01:01	W-2	Calcite	-10.07	-2.28	1.0650645	0.89121779	0.607
2018-04-20 07:24	W-2	Calcite	-10.69	-2.61	1.1659239	0.93212213	0.659
2018-04-20 18:00	W-2	Calcite	-9.84	-2.44	1.1439304	0.91879752	0.701
2018-04-20 21:08	W-2	Calcite	-10.09	-2.63	1.1439304	0.91879752	0.611
2018-04-21 03:24	W-2	Calcite	-10.85	-3.09	1.1875524	0.92790759	0.751
2018-04-25 04:36	W-2	Calcite	-10.00	-2.34	1.1040665	0.89192488	0.661
2018-04-25 08:24	W-2	Calcite	-9.31	-2.58	1.1040665	0.89192488	0.805
2018-05-03 18:36	W-2	Calcite	-10.02	-3.00	1.0507282	0.86158461	0.558
2018-04-19 22:39	W-3	Calcite	0.05	-5.22	1.0650645	0.89121779	0.335

2018-04-20 01:49	W-3	Calcite	-0.02	-5.25	1.0650645	0.89121779	0.582
2018-04-20 08:12	W-3	Calcite	0.17	-5.25	1.1659239	0.93212213	0.537
2018-04-20 21:56	W-3	Calcite	0.09	-5.25	1.1439304	0.91879752	0.487
2018-04-25 05:32	W-3	Calcite	0.05	-5.16	1.1040665	0.89192488	0.360
2018-04-25 22:03	W-3	Calcite	0.07	-5.26	1.058742	0.86566495	0.467
2018-05-03 17:48	W-3	Calcite	0.08	-5.19	1.0507282	0.86158461	0.501
2018-05-03 21:04	W-3	Calcite	0.06	-5.20	1.0507282	0.86158461	0.271
2018-05-03 22:40	W-3	Calcite	0.09	-5.18	1.0507282	0.86158461	0.307
2018-04-06 18:12	*W-4*	*Dolomite*	*-1.69*	*-6.12*	*0.9603792*	*0.70216541*	*0.201*
2018-04-19 23:28	W-4	Dolomite	-1.96	-6.42	1.0650645	0.89121779	0.351
2018-04-20 02:36	W-4	Dolomite	-1.89	-6.25	1.0650645	0.89121779	0.706
2018-04-20 08:59	W-4	Dolomite	-1.92	-6.46	1.1659239	0.93212213	0.443
2018-04-20 19:35	W-4	Dolomite	-1.89	-6.33	1.1439304	0.91879752	0.553
2018-04-20 22:42	W-4	Dolomite	-1.92	-6.24	1.1439304	0.91879752	0.552
2018-04-21 04:58	W-4	Dolomite	-1.96	-6.60	1.1875524	0.92790759	0.600
2018-04-21 05:46	W-4	Dolomite	-1.92	-6.24	1.1875524	0.92790759	0.547
2018-04-25 06:32	W-4	Dolomite	-1.79	-6.07	1.1040665	0.89192488	0.539
2018-04-25 14:34	W-4	Dolomite	-1.89	-6.27	1.1040665	0.89192488	0.635
2018-05-03 16:57	W-4	Dolomite	-2.08	-6.53	1.0507282	0.86158461	0.595